Universita' degli Studi di Napoli Federico II
Department of Chemical Engineering, Materials and Industrial Production

Ph.D in Engineering of Materials and Structures

XXVIII Cycle

A new bioengineered 3D tumor platform *in vitro* to replicate tumor-stroma interaction and investigate anti-cancer drug delivery

Ph.D Thesis

Filomena Gioiella

Tutor
Prof. Dr. Paolo Antonio Netti

Coordinator
Prof. Dr. Giuseppe Mensitieri

Advisors

Francesco Urciuolo PhD

Giorgia Imparato PhD

Virginia Brancato PhD

May 2016

"A mio padre che dall'alto mi guarda
e mi protegge ogni giorno"

Contents

Introduction

Nowadays, cancer is still a second leading cause of death after cardiovascular disease in the world [1]. One of the main factors that lead the failure of cancer therapy is related to the fact that little is known about the interaction of cancer cells with microenvironment. Indeed, as hypothesized in the "seed" and "soil" theory by Paget over a century ago, tumor progression is determined not only by tumor cells but also by the surrounding stromal milieu [2]. For these reasons in the last years, increasing attention is focused on the importance of tumor microenvironment in an effort to develop successful strategies in cancer disease treatment [3], [4]. In traditional two-dimensional *in vitro* models the absence of 3D architecture generates misleading and contradictory results [5]. Hence emerges the need to have an *in vitro* versatile platform that closely recapitulates pathophysiological features of the native tumor tissue and its surrounding microenvironment [5].

In this PhD thesis a microtissue precursors (μTP) assembling strategy, recently published [6], was used and translated to produce 3D tumor engineered models composed by tumor and/or stromal cells. In contrast with the classical spheroid model, the μTP we proposed presents the production of extracellular matrix directly synthesized by stromal cells.

First of all, in the chapter 1 a stat of art overview was presented which highlights the importance of tumor microenvironment in cancer research, the existing models for studying tumor development and the nanotechnology contribution in cancer treatment. Then the chapter 2 is focalized on the realization of stromal microtissues fabricated seeding normal or activated fibroblasts on microporous beads, in order to monitor their dynamic evolution in terms of metabolic activity, mechanical properties and ECM composition. In particular it is demonstrated how the microtissue configuration is able to keep phenotypic differences between normal and activated fibroblasts in all the aspects investigated compared to the classical 3D spheroidal model. In

the chapter 3 the cross talk between epithelial tumor and the surrounding stroma in a microfluidic device is investigated. Thanks to the combination of 3D microtissues with microfluidic technology, it is possible to detect in real time the modification occurring at cellular and ECM level during the activation period.

In the second part of work, the tumor microtissue model is validated as a potential drug-screening platform. In particular, in chapter 4 a commonly drug used in chemotherapy (Doxorubicin) is tested in order to detect the difference in chemoresistance between microtissues and spheroid models, both in monoculture and coculture. Finally, a stimuli-responsive nanoparticles are tested on normal and tumor 3D heterotypic microtissues to demonstrate their significant selectively. At last, the microtissue system may be a useful *in vitro* screening tool for testing innovative approaches of drug delivery, reducing expensive and time-consuming protocol nowadays used in preclinical studies.

Abbreviations

TME : Tumor Microenvironment
DCIS : Ductal Carcinoma *In Situ*
LCIS : Lobular Carcinoma *In Situ*
IDC : Invasive Ductal Carcinoma
ILC : Invasive Lobular Carcinoma
MSCs : Mesenchymal Stem Cells
ECM : ExtraCellular Matrix
MMPs: Matrix MetalloProteinases
CAF : Carcinoma Associated Fibroblasts
TGF-β : Transforming Growth Factor Beta
HGFs : Hepatocyte Growth Factors
IGFs : Insulin-like Growth Factors
uPA : Urokinase-type Plasminogen Activator
α-SMA : Smooth Muscle alpha-Actin
PDGFR-α/β : Platelet-Derived Growth Factors-α/β
HER2 : Human Epidermal growth factor Receptor 2
TAMs : Tumor Associted Macrophages
ECs : Endothelial Cells
LOX : Lysyl OXidase
FN : Fibronectin
HA : Hyaluronic Acid
PGs : ProteoGlycans
IFP : Interstitial Fluid Pressure
BM : Basement Membrane
EMT : Epithelial to Mesenchymal Transition
GAGs : GlycosAminoGlycans
HIF-1α : Hypoxia Inducible Factor-1α
PEG : PolyEthylene Glycol

PLG : Poly(Lactide-Co-Glycolide)

PLGA : Poly(Lactic-Co-Glycolic Acid)

PLA : PolyLactic Acid

3D-μTP = Three Dimensional MicroTissue Precursor / Precursors

PDMS : PolyDiMethylSiloxane

COPs : Cyclic Olefin Copolymers

PMMA : Poly(Methyl MethaAcrylate)

PC : PolyCarbonate

PS: PolyStyrene

PDAC : Pancreatic Ductal AdenoCarcinoma

MP : MultiPhoton microscopy

SHG : Second Harmonic Generation

TACS : Tumor Associated Collagen Signature

F/B ratio : Forward / Backward ratio

H & E : Haematoxylin and Eosin stain

GLCM : Gray Level Co-occurrence Matrix

NPs : NanoParticles

FRAP : Fluorescence Recovery After Photobleaching

FCS : Fluorescence Correlation Spectroscopy

Pgp : P-Glycoprotein

MRP : Multidrug Resistance Protein

MXR : MitoXantrone Resistance protein

BCRP : Breast Cancer Resistance Protein

NF = human Normal mammary Fibroblasts

DMEM : Dulbecco's Modified Eagle Medium

GPMs : Gelatin Porous Microbead / Microbeads

RT : Room Temperature

SEM : Scanning Electron Microscopy

GAL : Glyceraldeydes

PBS : Phosphate Buffered Saline

MPT : Multiple Particle Tracking microrheology

MSD : Mean Square Displacements

CF : Collagen Fraction

ROI : Region Of Interest

CAD : Collagen Assembly Degree

ANOVA : One-way Analysis of Variance

MCF7 = Human breast adenocarcinoma cells

RPMI : Roswell Park Memorial Institute

AC-μTP : ACtivated-NF-μTP

PFA : ParaFormAldehyde

THG : Third Harmonic Generation

DOX : Doxorubicin

MTT : 3-(4,5-dimethylthiazol-2-yl)- 2,5-diphenyltetrazolium bromide

DMSO : DiMethyl SulfOxide

MCF10 : Human non tumorigenic Epithelial cell lines

MEBM : Modified Eosin Methylene Blue agar

PELGA: Poly(D,L-lactic-co-glycolic acid) (PLGA) and Polyethylene glycol (PEG)

TAP : Tumor-Activated Prodrug

Chapter 1

State of Art

1.1 Tumor microenvironment

Nowadays, cancer remains a leading cause of death. Thus, it is not surprising that the majority of drug candidates in development today are aimed at stalling or eliminating cancer. However, cancer drug development is costly, as it suffers from a very low success rate. Despite significant progress in clinical research in recent years resulting in the development of more specific anticancer drugs such as nanoparticles or monoclonal antibodies such as imatinib, trastuzumab, crizotinib and vemurafenib, their activity remains poor with no evidence of tumor withdrawing [7]. The high heterogeneity and plasticity of this ever-changing dynamic desease make it difficult to develop widely applicable drugs with low side effects. There is extensive evidence demonstrating the importance of tumor microenvironment on cancer progression and treatment outcome [8]. Infact, tumor microenvironment (TME) plays an important role in regulating the behavior of cancer cells to invade and metastasize and poses multi-faceted barriers including biological, chemical and physical hindrance to drug transport and actions. These barriers are highly dynamic so their interactions and relative significance with respect to drug delivery and therapeutic efficacy vary drastically depending on the cancer type, stage and organs [9]. Indeed, in many tumor types, such as pan-

creatic and breast tumors, these barriers can become insurmountable, often leading to therapy failure [10]. To this end, the specific cross-talk between a given cancer and its stroma will have to be defined for each cancer type in order to achieve effective therapeutic targeting [8]. Carcinomas comprise the majority of all solid tumors, and their malignancy is driven not only by the genetic transformation of epithelial cells, but also by the remodeling of contiguous stromal tissue to foster growth, metastasis and therapy resistance [11]. Among carcinomas, breast cancer is the most frequent cancer in woman together with colorectal and ovarian cancers. The systemic outgrowth and spread of the cancer cells through a process known metastasis is the main cause of deaths in these patients. The development of breast cancer involves the progression via a series of intermediate hyperplastic lesions with and without atypia (atypical ductal hyperplasia, atypical lobular hyperplasia and usual ductal hyperplasia) followed by subsequent evolution into *in situ* carcinoma, for example ductal carcinoma (DCIS) and lobular carcinoma *in situ* (LCIS), invasive carcinomas and metastatic cancers (Fig. 1.1 [12]). In atypical hyperplasia, the breast cells are abnormal in number size, shape, appearance, and growth pattern that may be seen as an excessive growth of cells of the ducts (atypical ductal hyperplasia) or the cells of the lobules (atypical lobular hyperplasia). DCIS is thought to be a precursor of invasive ductal carcinoma, in which tumor cells are confined to the lumen of the mammary duct [12]. Seventy-five to 80% of invasive breast carcinomas are categorized as invasive ductal carcinoma (IDC), which is the progression of a primary tumor from within the breast duct to an invasion of surrounding tissue by penetrating through the basement membrane of the duct. During cancer progression from DCIS to IDC, the tumor cells invade the reactive stroma. Although the ductal epithelium and the underlying myoepithelial cells are separated from the surrounding connective tissue by a basement membrane in both normal and tumor carcinoma *in situ*, the basement membrane in DCIS, although intact, is altered.

LCIS, instead, is characterized as abnormal proliferation of acinar cells

in terminal ductal lobular units [13]. Invasive lobular carcinoma (ILC) is the invasive growth of cancer cells that originate in the lobules and penetrate the surrounding breast tissue [14]. Furthermore, gene expression changes occur in all cell types during breast tumor progression [15].

In breast cancer, dynamic changes in the microenvironment are characterized by formation of tumor stroma containing abundant fibrous components as well as by active recruitment of inflammatory cells during the progression from mammary gland hyperplasia to adenoma formation and eventually to cancer [16]. It is becoming increasingly clear that the inflammatory changes occurring in the tumor microenvironment are closely linked with initiation, promotion and progression of tumorigenesis, and thereby have become the focus of intense research [16].

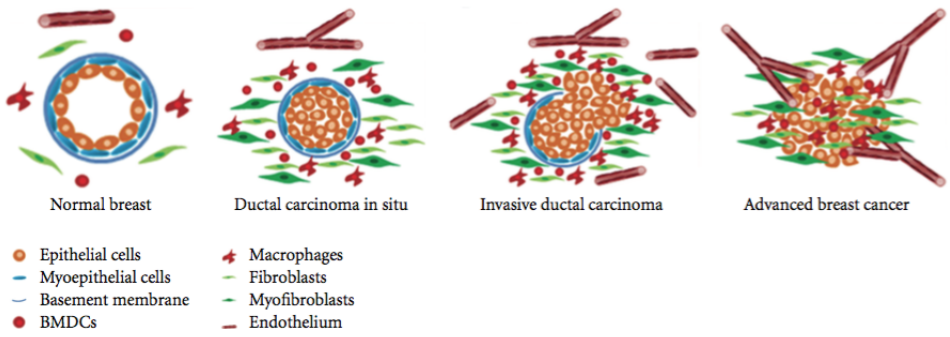

Figure 1.1: Schematic presentation of breast cancer progression accompanied with stromal cells [12].

Cellular components of the tumor microenvironment

Human tumors encompass various cell types whose functions and fate are further differentially influenced by multiple chemical, physical and biological factors present in the microenvironment [7]. In tumors, heterogeneous cancer cell populations coexist with non-mutated progenitor cells (epithelial cells) and stromal cells that support the TME. These include fibroblasts and immune cells, as well as endothelial cells and smooth muscle cells that form

blood vessels and provide nourishment to the tumor. In their dysfunctional state, fibroblast and immune cells produce chemokines and growth factors that stimulate cancer cell growth and invasion and can recruit other cells, including mesenchymal stem cells (MSCs) that replenish cells in the tumor [3]. The immune system plays dual roles in tumor development and progression. In addition to the above studies indicating that immune cells can promote tumor development, other studies have reported that adaptive immune cells, for example B and T lymphocytes, may inhibit later stages of cancer development by affecting growth and/or dissemination of primary tumors [17]. In addition to the cellular component, the extracellular matrix (ECM) and secreted extracellular molecules act in autocrine and/or paracrine manners to support/sustain tumor development (Fig. 1.2).

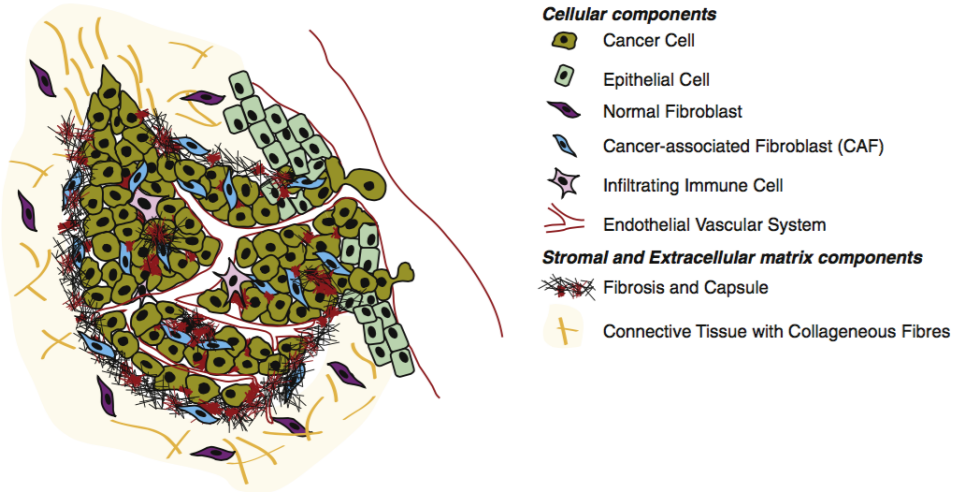

Figure 1.2: The tumor microenvironment: schematic illustrating cellular components (cancer cells and variuos stromal cells) coexisting in the tumor microenvironment and extracellular components secreted by the cellular components of the tumor [7].

Fibroblasts

As the predominant cells in stroma, fibroblasts are responsible for the elaboration of the most connective tissue components in the ECM, including collagens and structural proteoglycans, as well as various classes of proteolytic enzymes, their inhibitors and various growth factors [17]. In normal tissues, fibroblasts produce different collagen subtypes (type I, III and V) and fibronectin, and contribute to the formation of the basement membrane by secreting type IV collagen and laminin. They continuously remodel the ECM through a dynamic process of ECM protein production and degradation by matrix metalloproteinases (MMPs) and other proteases and are responsible for the overall architecture of tissues. The turnover is, however, well regulated and restrained [18]. On the other hand, cancer-associated fibroblasts (CAF) have phenotypes that are significantly different from normal fibroblasts. Like fibroblasts in wounds, CAF exhibit a higher proliferation rate, express α-smooth muscle actin and variants of fibronectin, which are involved in cell contraction and wound closure. However in tumors, unlike fibroblasts in wounds, CAFs do not revert back to their inactivated state, or undergo apoptosis.

The so-called CAF or myofibroblasts, peritumoral fibroblasts or reactive stromal cells, play a determinant role in malignant progression of cancer and represent an important target for cancer therapies [19]. CAF are known to supply many inflammatory mediators including a variety of cytokines, growth factors, tissue remodeling enzymes such as matrix metalloproteinases (MMPs) and ECM components, all of which modulate the TME to aid the active mobilization of the inflammatory cells [16]. CAF also secrete growth factors (transforming growth factor beta TGF-β, hepatocyte growth factors HGFs, insulin-like growth factors IGFs) and chemokines (monocyte chemotactic protein 1 and interleukin 1) that facilitate proliferation and invasion of cancer cells. In addition, CAF produce MMPs, mostly MMP-9 and MMP-2, and other matrix-modifying enzymes, including urokinase-type plasminogen activator (uPA) that degrades the ECM and support tumor invasion and

metastasis [3].

Smooth muscle α-actin (α-SMA) is the most common marker used to identify myofibroblasts together with PDGF receptor (PDGFR) α/β [20]. PDGF plays an important role in the regulation of fibroblasts and pericytes modulating tumor progression. Moreover it has a limited autocrine role in tumor cell replication, but it is a potential player, in a paracrine fashion, in tumor stroma development. PDGf induces CAF proliferation and possibly recruiting CAF indirectly by stimulation of TGF-β release from macrophages [21]. In breast cancer, high stromal PDGF β -receptor expression was significantly associated with high histopathological grade, estrogen receptor negativity and high HER-2 expression. Based on animal model studies, PDGF receptor activation in stromal cells have also been shown to control tumor drug uptake and tumor oxygenation [22].

Immune cells

In addition to fibroblasts, immune cells are abundant cells in tumor tissue. Among immune cells, tumor-associated macrophages (TAMs) have a central role in tumor growth [23]. TAMs derived from differentiated monocytes that have been recruited to the reactive stroma in response to tumoral chemotactic factors or from resident macrophages. There are two major lines connecting TAMs and cancer: 1) accumulation of TAMs in tissues of chronic inflammation apparently promotes cancer initiation and progression and 2) a high density of TAMs in tumor tissues often correlates with poor prognosis for cancer patients. It is well accepted that TAMs are required for tumor cell migration, invasion and metastasis formation [24]. However the best characterized pro-tumoral function of TAMs relates to their pro-angiogenic capacities by secretion of specific pro-angiogenic factors (VEGF, IL-1 β, TNF- α) or indirectly through the release of MMP-9 [24].

Endothelial cells

Besides interactions with TAMs and CAF, the interplay of tumor cells with endothelial cells (ECs) is also of pivotal importance for tumor progression and the development of metastasis. It is generally assumed that cancer cell migration through connective tissue is too slow and undirected to account for the quick spreading and metastasis formation seen in many tumors, and that cancer cells spread much more quickly and efficiently via lymph or blood vessels to distant sites. The endothelium and the basement membrane constitute a strong physical barrier, hence the process of intravasation is potentially time-consuming and rate-limiting in metastasis development [24]. Signaling cross-talk between cancer cells and ECs may involve up-regulation of adhesion molecule expression by the endothelium as well as by tumor cells, reorganization of the acto-myosin cytoskeleton and Src-mediated disruption of endothelial VE-cadherin-β-catenin cell-cell adhesions [24].

Abnormalities of tumor ECM

Extracellular matrix (ECM) is a fundamental component of the tumor microenvironment that acts bidirectionally, both affecting and being affected by tumor cells. The ECM not only plays an important role in providing support to tissues, but also directs a diverse set of functions in individual cells [25]. In particular, ECM can act as a scaffold for cell migration, a reservoir for cytokines and growth factors and a signal through receptor binding [16]. Although the ECM prevents tumor cells from invading the surrounding tissues its remodeling ECM is crucial in order to promote this phenomenon. Numerous factors are involved in this process, including integrins, lysyl oxidase (LOX) and MMPs. Integrins are a family of heterodimeric, transmembrane glycoproteins, consisting of one α and β unit. Each family member binds multiple ECM ligands which activates intracellular signaling pathways [26]. Members of the LOX family are secreted by cancer and stromal cells in response to hypoxia and modify the ECM [26]. In particular, LOX cross-links newly synthesized collagen and its expression and activity are elevated in

response to increased collagen deposition [27]. MMPs are a family of proteolytic enzymes which are synthesized both by tumor and peritumoral stromal cells (CAF) and their primary function is degradation of protein in the ECM and release growth factors and cytokines that reside in the ECM [26]. They can be considered the most important proteolytic enzyme for connective tissue dissolution [28]. Through their proteolytic activity, MMPs are implicated in cancer invasion and metastasis with different classes of MMPs being associated more frequently with cancer of varying origin [28]. Their expression is often highly up-regulated in many solid tumors, and the sustained presence of these proteases coupled with increased ECM synthesis and secretion, leads to the progressive destruction of normal ECM and its replacement by tumor-derived ECM. MMP degradation of the ECM not only facilitates cell movement but also generates numerous bioactive cleaved peptides and releases growth factors and chemokines that are contained within the ECM [27]. MMP-1 (collagenase-I), the first MMP discovered in 1962, is one of the proteases responsible for degrading fibrillar collagens. High-expression of MMP-1 has been linked to cell invasion *in vivo*; therefore targeting MMP-1 is often used as a strategy for attenuating cell invasion. Other members of MMP family, such as gelatinases MMP-2 and MMP-9, degrade collagen IV, which is the major component of basement membranes and is also found in stromal ECM [29]. These types of MMPs have focused great attention because they are overexpressed in a variety of malignant tumor and their expression and activity are often associated with tumor aggressiveness and a poor prognosis [30]. Elevated levels of gelatinases are found in breast, brain, ovarian, pancreas, colorectal, prostate and melanoma [30]. Furthermore, a differential regulation of MMP-expression can be found in tumors of different grades of malignancy in a mouse transplantation model *in vivo* as demonstrated by *Mueller et al.* (2002).

The abnormal structure and function of tumor stroma is largely attributed to the up-regulation of matrix remodeling molecules such as the transforming growth factor β (TGFβ) and some matrix components such as

fibronectin (FN) and hyaluronic acid (HA). These abnormalities, collectively known as desmoplasia, refer to the formation of a dense ECM characterized by increased levels of total fibrillar collagen, fibronectin, proteoglycans (PGs) and tenascin C and it is associated with activation of angiogenic programs. In fact, desmoplastic response has been demonstrated to be associated with more aggressive and invasive cancer and worse prognosis in several types of cancer such as papillary microcarcinomas, breast cancers and rectal cancers. FN plays an important role in the formation of the pre-metastatic niche. In particular, FN binds collagen and regulates collagen fibril organization. The dynamic and reciprocal relationship between collagen and FN plays a role in tumor progression [31]. *Fishbach et al.* (2005), reported that increased concentration of FN in tumors have been linked to enhanced malignant capacity of tumors [32]. Furthermore HA is another main component of the tumor microenvironment and has thus become an increasingly important target for cancer therapy [16]. It is a large glycosaminoglycan known to be up-regulated in the extracellular space of tumor and thought to impede drug delivery by functioning as an immobile, gel-like phase due to negative charge repulsion and water sequestration. For instance, increased secretion of HA by CAF is commonly observed in pancreatic cancer and it is known to promote tumor growth. This could be caused by increased interstitial pressure (IFP) due to water molecule retention [33]. Similar to other ECM molecules, HA degradation products have the ability to induce specific gene expression programs for proteases and cytokines that are necessary for inflammation and matrix remodeling [16]. ECM deposition and desmoplastic response differ significantly among various cancer types, indicating different mechanisms of cancer development and progression. Desmoplasia may contribute to an increase in tumor density that, as a tumor grows in the confined space of the host tissue, results in the generation and accumulation of mechanical forces among the components of the tumor microenvironment. Finally, desmoplasia limits the available space for transport in the tumor interstitial space, which prevents homogeneous penetration of therapeutic agents. High collagen and

cellular densities reduce the size of the pores of the tumor interstitial space and as a result the resistance to interstitial fluid flow increases. This, in turn, further enhances the uniform elevation of the IFP and renders diffusion the dominant transport mechanism in the tumor interior [10].

1.1.1 Cancer cell invasion in tumor microenvironment

Tumor cell migration is a crucial prerequisite for metastasis and has been regarded largely as a mechanical process dependent on the expression of adhesion molecules and matrix degrading enzymes [24]. This phenomenon involves dynamic and drastic changes in the adhesion structures, also called the focal complexes, which are assembled by membrane, associated receptor and other signal-relaying molecules. The drastic changes in cell adhesion state during migration and invasion are fulfilled by actin polymerization that facilitates its disassembly and reorganization that confers the motility of the cells [23]. As outlined by *Branek et al.* (2010) [34], the architecture and composition of the TME in terms of structural and biochemical properties of the ECM (fiber network, morphology collagen content, fiber thickness, extent of intrafibrillar crosslinks and the ratio mesh size-diameter of the migrating cell) determines the degree of resistance the moving of cells [24]. Epithelial-stromal interaction plays a crucial role in tumor formation and progression. Therefore, due to the increased stroma associated with breast tissue density, increasing collagen density in the mammary gland promotes tumorigenesis or stromagenesis [35]. Stromagenesis is induced by neoplasia, accompanies tumor development and can be sorted into three distinctive phases: normal, primed, and activated [36]. Recent studies indicate that the TME can profoundly affect tumorigenesis even at the earliest stages of neoplasia prior to breaching the epithelial basement membrane barrier [37]. The first step in metastasis is the migration of cancer cells away from the primary tumor, a process called *tumor invasion* (Fig. 1.3). *In vivo* cancer cells can invade tissue individually as single cells in elongated, mesenchymal or rounded, amoeboid modes after cell-cell junctions were abandoned. Al-

ternatively, cancer cells retain cell-cell junctions and migrate collectively as cohesive multicellular units into the peritumoural stroma [38].

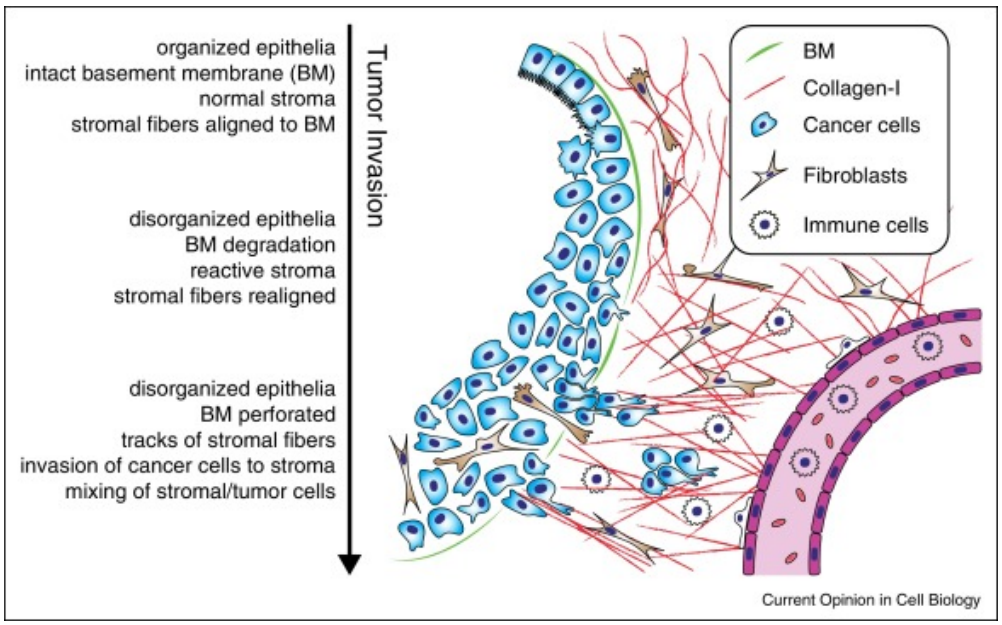

Figure 1.3: Summary of tumor progression and invasion [39].

Tumor cells often localize near dense collagen and promote a desmoplastic response, followed by tumor growth and expansion of the collagen matrix leading to matrix reorganization to help facilitate local invasion [40]. In solid epithelial tumors or *carcinomas*, invading cells cross the basement membrane (BM), a natural barrier between the epithelium and the stroma and come into direct contact with the interstitial/stromal ECM. These migrating activated epithelial cells can trigger the activation of stromal cells, either directly or by means of paracrine signals, resulted in a "primed" or "activated" stroma [29]. Finally metastasizing cells migrate through the stroma to reach blood or lymph vessels, where they can be carried to other organs [39]. *In vitro* studies have identified different intrinsic factors regulating migration of cancer cells. Tumor cells are able to migrate individually or collectively depending on typology of cell. In addition to intrinsic factors, the TME plays a significant role in determining cancer cell migration mode and morphology. In

human epithelial cancers such as breast and colorectal cancers, invasive cells are typically observed to migrate collectively. Invading cells often display characteristic Epithelial to Mesenchymal Transition (EMT) markers, such as down-regulation of E-cadherin and up-regulation of Vimentin, and lose some epithelial characteristics, such as apical-basal polarity. During tumor progression, the stroma also undergoes profound changes.

The content and distribution of collagen in cancer tissue are different from the corresponding normal tissue due to remodeling of the ECM during malignant process. In particular, CAF deposit abundant amounts of fibrillar ECM molecules including collagen I and FN. These ECM compositional changes entail structural and mechanical alterations of the ECM. For example, CAF mediate the partial unfolding of FN, which increases both the stiffness of individual FN fibers and their ability to bind other ECM molecules such as glycosaminoglycans (GAGs) and collagen. Along with elevated collagen crosslinking and GAG concentration, these pronounced changes in ECM density and intermolecular interactions globally enhance tumor stiffness with direct consequences for tumor progression [41]. Under normal physiologic conditions, fibroblasts are in an inactive quiescent state, have a low proliferative index and only secrete factors needed to maintain normal tissue homeostasis. Tumor cells are unable to overcome the constraints imposed by the normal microenvironment unless stroma itself undergoes a series of alterations. Changes in normal stromal fibroblasts produce a "primed" stroma that promotes tumor growth and invasion during the earliest stages of stromagenesis [37]. Activation of stromal cells into CAF has many consequences for tumor development, progression and cancer metastasis. CAF have been reported to produce a variety of growth factors and cytokines that promote tumor progression. Secreted stroma-derived factors include TGFβ1, HGF, EGF, VEGF, stroma-derived factor-1, basic FGF and pro-inflammatory cytokines CXCL14, IL-1, IL-6 and IL-8.

1.2 Existing models for studying tumor development and drug testing

Tissue engineering is a multidisciplinary field aimed at creation of human tissues or organs by hybridizing therapeutic cells with biomaterials and other conditions that facilitate cell growth and differentiation followed by tissue morphogenesis. Apart form the current mainstream applications of tissue engineering in therapeutics for repairing or replacing diseased tissues or organs, namely for the purpose regenerative medicine, the engineered tissues can also be potentially used for cancer drug evaluation. Drug evaluation is generally assessed in terms of three key areas: drug delivery methods, drug efficacy and drug toxicity. These parameters are important because it is imperative to develop an efficient drug delivery method that can maximize drug efficacy while minimizing toxic side effects [42]. One of the most immediate uses for tissue-engineered systems is as a tool for biologists and physicians to create a more clinically accurate *ex vivo* physiology of human tissues.

Below it is described current state of *in vivo* and *in vitro* models.

1.2.1 *In vivo* models

One way to better replicate the biological complexity of human tumor growth is to study human cancer within an animal model. This provides tumor cells with many of the 3D microenvironmental cues that are missing during monolayer growth. The most common mouse model employed in drug testing for solid tumors is the subcutaneous human tumor xenograft. In this model, human tumor cells are implanted just beneath the skin of immunodeficient mice, and a few days or weeks are allowed for initial tumor growth before drug candidates are administered. A great advantage of this method is the capability to transplant both cancer tissue and surrounding stroma to mimic the complexity of the human tumor microenvironment. Unfortunately, many drugs appear promising when tested in xenografts, but several studies involving a variety of tumor types have found a general lack of correlation between

the human tumor xenograft response data and the results of phase II clinical trials [43] (Fig. 1.4). The reasons can be most likely due to murine origin rather than human of TME, which implies subtle but important changes that impact tumor cell behavior. Obvious limitations of animal models that preclude their use in large-scale drug discovery programs include their unsuitability for high-throughput drug screening owing to considerations of space, time and cost. Another major challenge is how to observe tumor growth or regression over the course of a treatment, for example at weekly intervals. The assessment of treatment efficacy can be reliably performed only at the end of the trial, when animal is sacrificed [44].

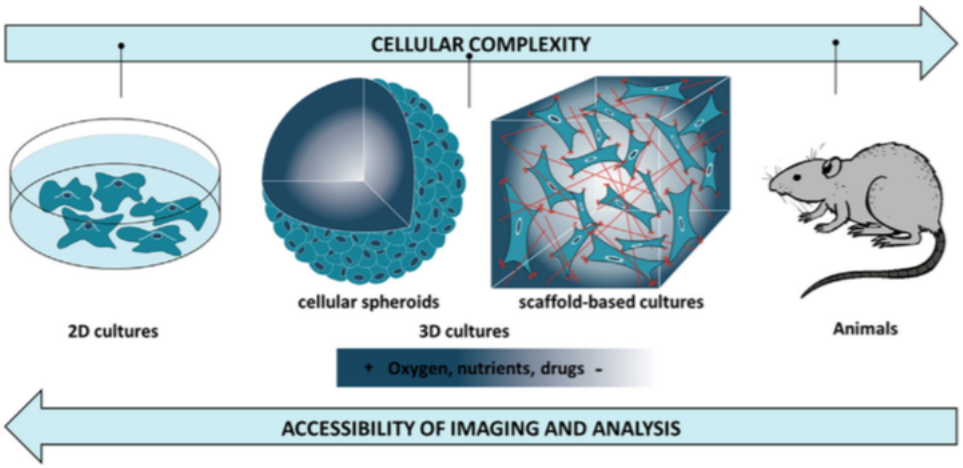

Figure 1.4: *In vitro* and *in vivo* models [45].

1.2.2 *In vitro* models

The complexity of TME *in vivo* makes difficult to study manifold phenomena like tumor invasion because it is necessary to isolate and control individual stimuli. The requirement for such control has led to the development of *in vitro* assays that mimic aspects of the *in vivo* tissue. *In vitro* testing of anticancer drugs typically involves growing cancer cell lines as monolayers on Petri dishes and using high-throughput screening procedures to evaluate

drug efficacy. In 2D cells are not able to organize into tissue-like structures since they lack the tridimensionality of the surrounding microenvironment [46]. For this reason, the monolayer culture has remained a poor predictor of whether a given drug will ultimately yield clinical benefit. These cells, therefore, may not be representative of the tumor as a whole and are especially susceptible to therapies that target rapidly dividing cells. Perhaps the most dramatic alterations occur, however, because of the removal of the cells from their native microenvironment, including the ECM, soluble signals, 3D architecture, stromal cells, and irregular microvasculature that surround the tumor cells *in vivo*. These stromal elements affect many different aspects of cancer cell behavior, including the cell's proliferation rate and resistance to drug-induced apoptosis [43]. To avoid these experimental inconsistencies, it is essential to develop models with a higher degree of complexity with retaining the reproducibility and the capacity of cellular level imaging [45]. Recent advances in this field include the incorporation of multiple cell types and ECM proteins into 3D models to recapitulate the structure, organization and functionality of live tissue *in situ* [47].

In recent years there are increasingly more attempts to create three-dimensional biomimetic engineered tissue models that are expected to better fulfill the role in drug evaluation. These attempts are aimed at recapitulating some of the important human native tissue structures and functions so that the response to therapeutic administrations may be predicted more accurately in an *in vitro* setting. This paradigm shift from two dimensional cell-based model to 3D tissue model is essential because cell cultured on cell culture plates or microwells are incapable of providing a realistic model of the intercellular environment [42]. Tumor cell spheroid and scaffold-based models are the most popular 3D culture systems that have been concomitantly developing since the 1970s [23]. In 3D tumor models, cells are cultured as aggregates (spheroids), are grown on 3D scaffold materials or are embedded in gels. In every case, cells in a 3D environment behave fundamentally different from cells in monolayer culture, as cell-matrix interactions trigger signaling

pathways and cellular responses in 3D, which may not be observed in 2D [47]. Moreover, biochemical nature of cell-cell and cell-extracellular matrix contacts and the structural organization of cells differ significantly between two dimensional and three dimensional cultures, which could also be responsible of augmented drug resistance of cancer cells in three dimensional culture [48].

Human spheroid

By far, the most widely used 3D model is the human tumor spheroid, a small, tightly bound cellular aggregate that forms in the absence of cell substrate adhesion. These cellular aggregates can range in size from 20 μm all the way up to 1 mm in diameter, depending on the cell type and growth conditions. Spheroids have been widely used in cancer research because the 3D architecture and extensive cell-cell contacts provided by spheroid growth appear to better mimic the *in vivo* cellular environment than two-dimensional monolayer cultures. Spheroids also exhibit many of the biological properties of solid tumors, including cell morphology, growth kinetics, gene expression and drug response. Spheroid formation can be induced by a variety of different techniques including hanging drop method, liquid-overlay cultures and dynamic bioreactors. In the hanging drop method, cells form spheroids within small droplets of cell suspensions (approximately 20-50 μL). Due to the surface tension, liquid can maintain droplets when the lid is inverted and cells settled at the bottom of the droplet, air-liquid interface [9]. A simpler method for spheroid production involves liquid overlay of a cell suspension over a non-adherent surface, such as agar-coated plates. Spheroids can also be formed by culturing in spinner flasks or bioreactors, which can provide dynamic conditions preventing cell-substrate contact and promoting cells to form aggregates by either stirring or rotating bioreactors. The earliest method employed in cancer biology, that is widely used today, is spinner flask culture, where fluid turbulence prevents attachment and promotes cellular aggregation. This system can produce large numbers of relatively consistent spheroids, but they both require specialized equipment and additional pro-

cessing steps when used for drug testing. One of the major uses of human tumor spheroids has been as a preclinical screening tool for anticancer drug candidates, including traditional cytotoxic drugs, antibody-based therapies, and various experimental therapeutic approaches. Cancer cells from a wide variety of tumor types consistently display greater resistance to anticancer drugs when grown within spheroids, compared to monolayer controls, replicating what is often observed in the clinical settings. The increased chemoresistance in spheroids compared to monolayer cultures may be explained in part by increased cell-cell contact, 3D cellular architecture, enhanced deposition of tumor-derived ECM within the spheroid, a lower overall cell proliferation rate, or a combination of these factors. Although a 3D system with cancer cell lines cannot recapitulate the genetic heterogeneity found in tumors, modeling cellular heterogeneity can be achieved to a certain degree with heterotypic multi-cellular models. Examples of 3D co-culture models are formed by tumor cells and fibroblasts or a further increase in the complexity of the model can be achieved by implementing endothelial cells [7]. 3D heterotypic tumors cultures enable tumor cells to establish cell-cell and cell-ECM interactions, which are important elements in tumor signaling and which modulate tumor responses to therapeutic agents. Spheroids are convenient and relatively simple techniques to simulate *in vivo* solid tumor. Cells within spheroids display cell-cell interactions and produce *in vivo* tumor-like biochemical responses compared to 2D cell culture [9]. In spite of these advantages, the lack of interstitial fluid dynamics, which is highly relevant to drug transport within the TME, is one of the major limitations. It is therefore likely that the diffusion of most drugs, which are typically much larger than oxygen and carbon dioxide molecules, will be limited within spheroids as well [43].

Tumor cells embedded in gels

Considering that microenvironment controls tumorigenesis, ECM analogs have been introduced as cell culture systems in order to embed cells in a 3D

context and display the appropriate physical, chemical and mechanical cues for cell fates. Because spheroid culture only succeeds in mimicking a small part of the *in vivo* microenvironment, more advanced 3D cancer models have been developed using biological gels as a substrate for spheroid growth. Pioneering work has been based on the use of biomaterials from natural origins, principally Matrigel and collagen [45]. Matrigel is a basement membrane extract derived from the Engelbreth-Holm-Swarm mouse sarcoma that contains a diverse array of components, including collagen type IV, laminin, and other ECM molecules, as well as various soluble signals, such as cytokines and growth factors [43]. Spheroids developed from culturing cell lines within collagen gel culture have been used in chemotherapeutic testing and show increased drug resistance compared to the same cell lines grown in monolayer cultures [43]. Alginate is other natural polymer gels used for cancer cell cultures, derived from brown seaweed. It has been used as a scaffold for encapsulation of various types of cells. The main advantage associated with alginate is that gelation can be accomplished at room temperature after adding the cells to the polymer. Hydrogels also provide the possibility of conjugation with defined adhesion ligands or delivery of specific biomolecules (growth factors, pro-angiogenic factors, amongst others) [46]. When encapsulated within a 3D gel, cancer cells will often aggregate into 3D spherical structures. Experiments have revealed that phenotypically differences between malignant and normal epithelial cells can be exclusively observed in 3D cultures, in which malignant cells lose tissue polarity and organization, phenomena not commonly detected in 2D. Therefore, the remarkable plasticity of cancer cells under different experimental conditions can be easily reproduced by using 3D cultures, which enable reestablishment *in vitro* crosstalk among neighboring cells and their surrounding stroma [45].

Microscaffold based approach

Besides using self-assembled multicellular spheroids as *in vitro* models for the testing of novel drugs, carrier or delivery systems, there are also a comparable

number of studies that make use of scaffolds for *in vitro* tumor modeling [42]. Scaffold-based systems provide a platform where cells are grown in a semi-solid matrix that allows the study the influences of mainly external physical factors on microspheroid growth and signaling [7]. 3D scaffolds mimic ECM of connective tissues and provide architectural support for tissue engineering and regeneration with select cell types [23]. To attain an accurate recreation of *in vivo* TME, the scaffold material of choice to replicate ECM would need to satisfy two key requirements: molecular composition and stiffness. In general, scaffolds can be categorized into two groups: natural and synthetic scaffolds [42]. Based on the nature of the scaffolding materials, they are either biodegradable or non-biodegradable and biocompatible or non-biocompatible. Biomaterials, either natural or synthetic, that are biodegradable and biocompatible are highly demanded in tissue engineering and 3D tumor models [23]. Natural scaffolds are mainly composed of a wide range of hydrogels. Generally, the hydrogels are mechanically weak but they provide a biomimetic environment that supports cell proliferation and differentiation. Most of the hydrogels used are made up of naturally occurring materials or proteins found in the ECM. One of the many examples is collagen type I. A recent study have demonstrated the ability of collagen type I hydrogels in supporting the development of 3D *in vitro* biomimetic engineered tumors. The fidelity of this tumor model in mimicking parts of pre-vascularized stages of the native solid tumor progression, such as the development of necrotic regions and intracellular hypoxia with increasing tumor size was validated by the expression and upregulation of hypoxia-inducible factor (HIF)-1α [42]. Besides collagen gels, HA hydrogels represent another type of natural scaffold that many studies have explored for use in engineered 3D tumor models [42]. These matrices have produced important conceptual advances, since they have achieved the over-expression of tumor genes (EMT markers, MMPs, pro-angiogenic factors) and the acquisition of drug resistance compared to 2D cultures, mimicking the *in vivo* cellular response. On the other hand, the *in vivo* stiffness values can be easily recreated by increasing concentration or

cross-linking density of these biomaterials. The composition and stiffness of the tissue can be a critical variable depending on the animal origin and the isolation and purification procedures, compromising assay reproducibility. To overcome all these drawbacks, a further step in cancer biology involved the development of synthetic biomaterials. With advancements in the biomaterial field, scaffolds can be readily fabricated from various synthetic polymers, which are biodegradable and easily adapted into the appropriate shapes for use in different applications. These synthetic polymers, with better mechanical strength as compared to their natural counterparts, have been actively employed for use in the construction of 3D tumor models [42]. Polyethylene glycol (PEG), poly(lactide-co-glycolide) (PLG), poly(lactic-co-glycolic acid) (PLGA) and polylactic acid (PLA) [45] materials are among the wide range of synthetic scaffolds utilized for this purpose (Fig. 1.5). Most of these scaffold-based systems allow controlling spheroid size by adjusting pore-size and density. Among the studies on 3D cancer cell growth within synthetic scaffold, *Mooney and colleagues* (2007), employed a porous PLG scaffold to investigate the angiogenic properties of cancer cells in a 3D environment. They found that comparisons of angiogenic factor secretion and drug responsiveness of tumors engineered in the PLG scaffold or in standard 3D Matrigel culture indicate that, in some situations, tumors grown in the PLG scaffolds may be more appropriate models to study certain aspects of cancer progression [32].

Selection of the ideal biomaterial scaffold for a given cell type is problematic and has been accomplished to date mostly by trial and error. Even if the right biomaterial is available, achieving a high enough cell density and the homogeneous cell distribution necessary to construct a viable tissue is extremely time consuming. Furthermore, preshaping the scaffold may present further difficulties. To overcome these limitations, recent efforts have been concentrated on scaffold-less tissue engineering and bottom-up approaches aimed at generating a larger tissue construct by the assembly of smaller building blocks, which mimics the *in vivo* tissue structure of repeating func-

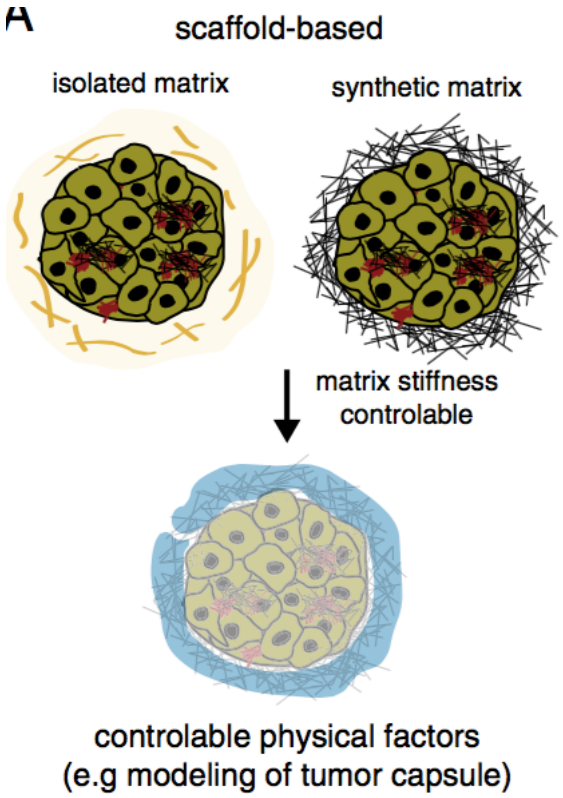

Figure 1.5: Scaffold based-models either with a natural isolated matrix (Matrigel, left) or synthetic matrix (bottom) controlling matrix stiffness and influencing physical factors [7].

tional units. An example of a bottom-up approach was used by *Du et al.* (2008), to direct the assembly of cell-laden microgels to generate 3D tissue with tunable microarchitecture and complexity [49]. *McGuigan and Sefton* (2006), proposed another interesting use of modular components for generating tissue. In their approach, rod-shaped collagen microgels that were seeded with HepG2 hepatocytes on the inside and endothelial cells on the surface were "packed" together within a bioreactor and perfused with medium [50]. *Netti and co-workers* (2010), produced a new microtissue precursor assembly strategy (μTP) to produce pieces of viable 3D tissue-equivalent to resemble and capture the major features of native tissue. In particular, μTP were

obtained by means of dynamic cell seeding of bovine fibroblasts on porous gelatin microcarriers using a spinner flask bioreactor [51] (Fig. 1.6). They suggested that the porous structure of microcarriers created a suitable environment for the development of fibroblasts, as the cells within the interior will experience lower shear forces than those encountered with non-porous carriers. Furthermore, under optimal culture conditions cells were able to adhere, proliferate and in particular synthesize ECM components to form a thin layer of tissue around the microbeads [44].

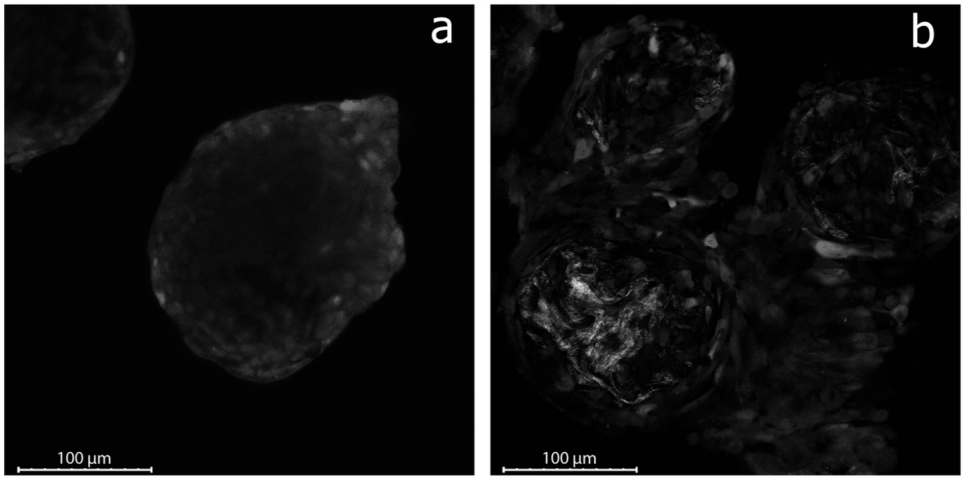

Figure 1.6: CAF-spheroid *vs* CAF-μTP. Multiphoton image of CAF-spheroid (a) and CAF-μTP (b). Light grey indicates SHG signal. Scale bar 100 μm [44].

Ultimately, 3D cultures, both spheroids and scaffold based-models, can contribute to the reduction in animal testing and allow for economical savings as well as become a powerful model to optimize drug candidates for enhanced tissue distribution and efficacy [45].

1.3 Microfluidics in tumor biology

1.3.1 General principles of microfluidics

Microfluidics - the science of manipulating small amounts (10^{-9} to 10^{-18} L) of fluids in microfabricated hollow channels - is a microsystem technology that has been used to generate and precisely tune dynamic fluid flows and spatio-temporal gradients, as well as deliver nutrients and other chemical cues to cells in a controlled manner [52]. Owing to their small size, fluid flow in microfluidic systems is entirely laminar (no turbulence) and virtually no mixing occurs between neighboring streams that flow beside each other within the same hollow channel [52]. Microfluidics typically comprises systems involving fluids with geometries having characteristic length dimensions on the order of tens to hundreds of microns. Microfluidics possesses a large number of advantages, including being easy to fabricate, low reagent consumption, parallel and rapid processing ability, and large-scale integration [53].

Materials

Initial development of microfluidic devices focused on the application of conventional silicon and glass micro-machining processes, but the emergence of BioMEMS fabrication techniques such as replica molding has spawned the development of microfluidic cell culture models in an array of materials platforms including synthetic and natural materials as well as bioresorbable systems. Important considerations for the selection of substrate materials for microfluidic cell culture models include optical transparency for cell imaging, the desired degree of mechanical rigidity or flexibility, surface chemistry and reactivity, and the ability to functionalize materials with chemical moieties for modulation of cell-surface interactions. Synthetic polymers such as PolyDiMethylSiloxane (PDMS) are the most common platforms for microfluidic systems and have been applied to cell culture models based on their high oxygen permeability, optical transparency, and ease of fabrication [54].

PDMS, a thermosetting polymer, is an attractive choice for the fabrication of microdevices for the culture of cells and tissues. First, it has a high gas permeability that ensures sufficient oxygen supply to cells in microchannels, eliminating the need for separate oxygenators that are commonly required in silicon, glass and plastic devices. Another advantage of PDMS is its optical transparency from ultraviolet to the near infrared wavelengths [52]. While the high permeability of PDMS to oxygen is often used to great advantage in cell culture systems, its tendency to absorb, retain and release other chemicals and some organic solvents in an unpredictable fashion has been a problem for many applications [54]. Other materials with greater chemical stability that have been used in microfluidics include cyclic olefin copolymers (COPs), poly(methyl methacrylate) (PMMA), polycarbonate (PC), and polystyrene (PS), the material traditionally used in static tissue culture dishes [54].

Fabrication

Methods for constructing microfluidic devices encompass a broad range of microfabrication techniques. The most commonly used approach is soft lithography, in which a thermosetting polymer (often PDMS) is poured onto a silicon mold featuring channel geometries, and is then cured and demolded. Two pieces of the polymer are then laminated to generate a closed microchannel. Master molds are typically fabricated using SU-8 photolithography, but deep reactive ion etching, xenon difluoride, electroplating, and ultrasonic milling have also been demonstrated to achieve a range of desired channel geometries. In addition to solvent casting, other methods of fabricating devices include hot embossing and injection molding COPs and polystyrene, and traditional machining of materials such as polycarbonate [54].

1.3.2 Microfluidics for mimicking tumor microenvironment

Applications of microfluidic systems based on cell and tissue culture are now emerging as platforms for high-throughput screening, drug discovery and toxicity testing, and future directions include the development of organ assist and organ replacement devices [55]. Today there are a vast number of approaches using microfabrication to develop new cell culture platform that recapitulate the characteristics of the *in vivo* environment [8]. Hence, the combination of tissue engineering and microfabrication affords the development of novel *in vitro* approaches to quantitatively assess constitutive microenvironmental features that are frequently neglected by conventional tissue culture methods or obscured by the complexity of *in vivo* models [11]. Microfluidic devices often accommodate fluid flow, an important physiological condition not present within static culture dishes. Flow conditions in microfluidic devices are useful for the application of fluid mechanical forces to cells, the formation of gradients of oxygen, growth factors and other biochemical signals, and maintenance of cell-cell communications [54]. Besides the need to better understand the repercussions of fluid flow in the tumor microenvironment, the inclusion of perfusion is also a potential strategy to overcome the diffusional limitations associated with most 3D tumor models. To achieve this goal of recapitulating tumor-associated fluid dynamics, tight integration of the two most relevant engineering disciplines, microfluidics and tissue engineering is necessary [43]. Recent advances in microfluidic technology have made it possible to create a novel assays that allow precise control of the cellular microenvironment [56]. Cells are embedded into a network of channels and subjected to continuous flow [47]. A clear advantage is the control of the liquid flow at *in vivo* relevant (capillary) dimensions, wchich makes it possible to regulate nutrient and drug concentrations at the levels of single cells or small clusters [8]. The laminar flow regime can easily be created in a microchannel and are characterized by low turbulence and mixing of parallel streams by diffusion only [8]. This condition presents the opportu-

nity to mimic concentration gradients typical of the tumor niche, with better recapitulation of drug transport and transient biological processes occurring down to the single cell level [43]. Generally, the chemical gradients generated by microfluidics include static and dynamic modes. The static modes often rely on molecular diffusion in static liquid, so that continuous concentration gradient can be formed. The formation of concentration gradients in dynamic modes, instead, is mainly based on the diffusion and the convection of flowing liquid in laminar flow [53].

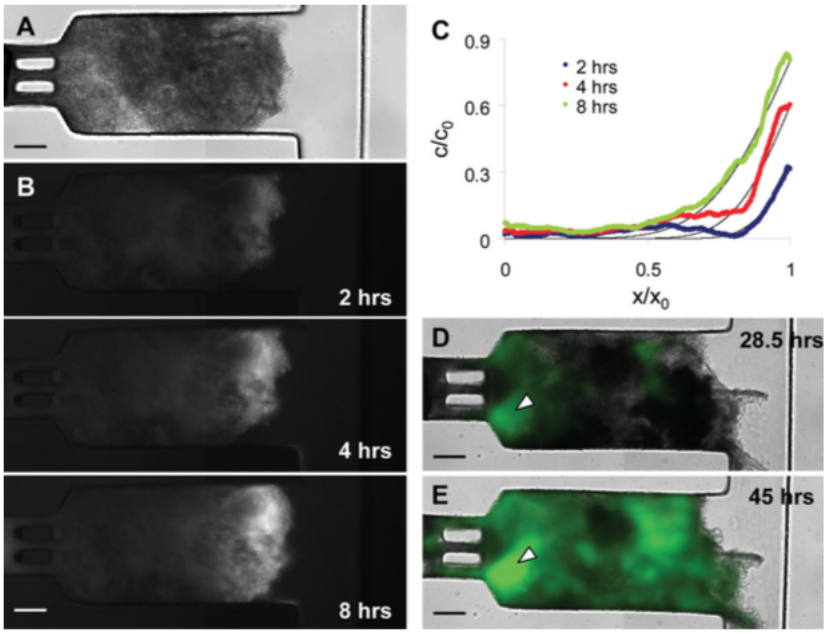

Figure 1.7: Diffusion and penetration of doxorubicin and therapeutic Salmonella bacteria [57].

One of the most prominent manifestations of this research direction is represented by the work of *Jang et al.*, who developed a platform able to evaluate up to 100 different drug combinations, in line with the emerging importance of combinatorial drug therapy for chemoresistant patients. The development of microfabrication techniques such as microcontact printing and soft lithography further enhanced microfluidic capabilities, that is, bet-

ter control over topology and surface chemistry, hence paving the way for more sophisticated mechanistic investigations of tumor biology [43]. In order to address the lack of interstitial fluid dynamics, recent studies tried to integrate spheroids into microfluidic platforms where spheroids were subjected to interstitial fluid flow. In these models, spheroids were cultured within polymeric matrices to mimic cell-matrix interactions *in vivo*, allowing for the generation of spatial gradients of growth factors and pH. *Walsh et al.* (2009), have created the pH gradient of the perfused spheroid culture on a microfluidic platform, and visualized the doxorubicin diffusion through the tumor spheroids (Fig. 1.7) [57].

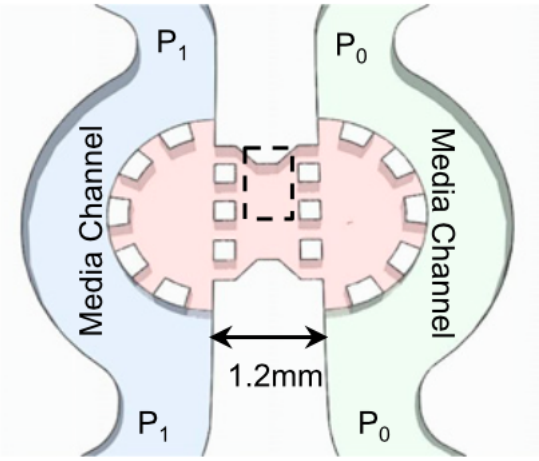

Figure 1.8: Microfluidic cell culture system for investigating the effects of interstitial flow on tumor cell migration [58].

Beyond being able to mimic the multicellular cross talk within the TME, microfluidic culture systems have recently been shown to have utility in investigating the effect of interstitial flow on tumor cell migration. *Polacheck et al.* (2011), developed a microfluidic platform to mimic stable pressure gradients and fluid flow across the tumor interstitium. In this model, breast cancer cells (MDA-MB-231) were seeded in type I collagen matrix and cultured under the perfusion of interstitial flow created by pressure difference across the matrix. By controlling the pressure of each media channel, the flow

rate could be precisely controlled and its effects on cell migration behavior were studied (Fig. 1.8) [58].

Recently several studies have been reported on microfluidic 3D environments for co-culturing different types of cells. *Liu et al.* (2010), have developed a microfluidic device for co-culturing tumor cells and CAF in an *in vivo*-like 3D microenvironment and investigated the role of CAF in tumor invasion *in vitro*. Communication between CAF and tumor cells could be established via medium diffused in matrix (Fig. 1.9) [19].

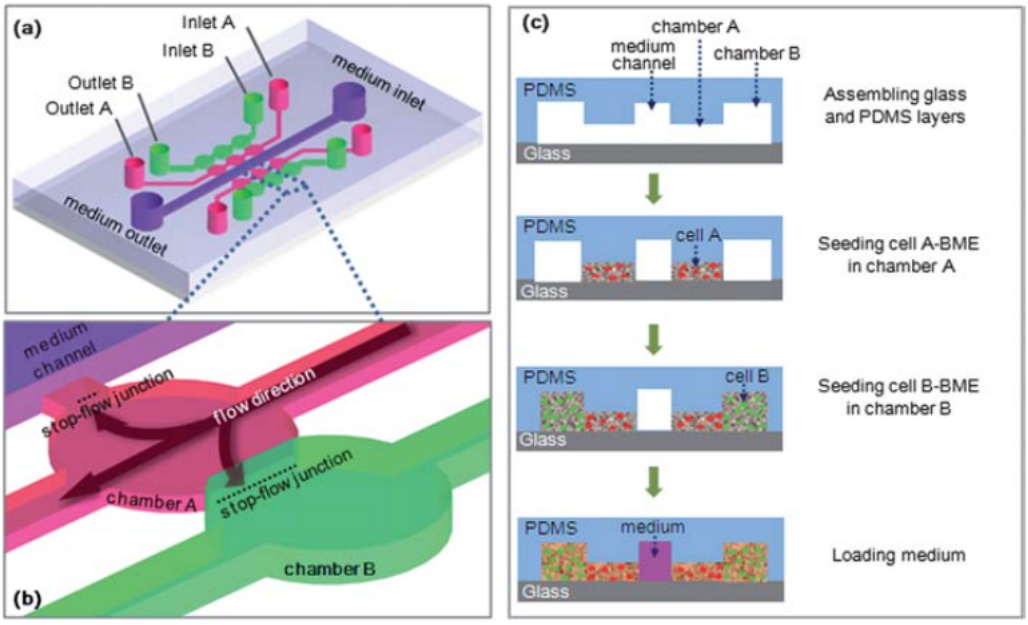

Figure 1.9: Chip design and cell-loading steps. (a) Schematic representation of the microfluidic chip for 3D cell co-colture. (b) A magnified illustration of one co-colture unit. (c) Cross section of two co-colture units and medium channel showing cell-loading steps [19].

Drifka et al. (2013), introduced an *in vitro* microfluidic model of pancreatic ductal adenocarcinoma (PDAC) microenvironment incorporating the *in vivo* complexities of multicellularity, ECM components, and a rationally-defined 3D microarchitecture (Fig. 1.10) [59].

Choi et al. (2015), described a biomimetic microengineering strategy

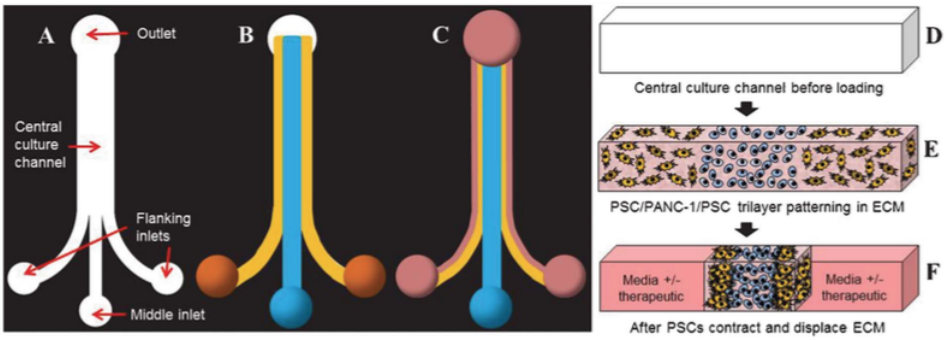

Figure 1.10: Design and operation of the microfluidic device. (A) a device after trilayer patterning (B) and a contarcted trilayer culture with media (pink) added (C) three cell-ECM droplets are placed on the inlet ports and simultaneously drawn into the central culture channel from the outlet. The process of culture etablishment is depicted in cross-section (D-F) [59].

to reconstitute 3D structural organization and microenvironment of breast tumors in human cell-based *in vitro* models. They developed a microsystem that enabled co-culture of breast tumor spheroids with human mammary ductal epithelial cells and mammary fibroblasts in a compartmentalized 3D microfluidic device to replicate microarchitecture of DCIS (Fig. 1.11) [60].

1.4 Intravital microscopy to study tumor - stroma interface

An approach to characterize TME components and observe its change following pharmacological intervention with high spatial and temporal resolution is with *in vivo* or *intravital microscopy*. Quantitative intravital microscopy requires four components: first, a tissue preparation that allow visualization; second, a molecular probe that can be detected by a microscope; third, a microscope and detection system; and fourth, computer algorithms and mathematical models that can be used to extract parameters of interest from the optical information. The tissue preparations fall into two broad cate-

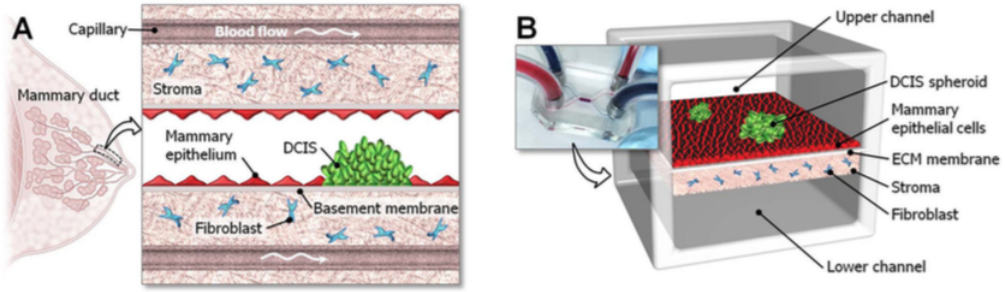

Figure 1.11: (A) DCIS is embedded in a mammary duct consisting of the mammary epithelium and a basement membrane surrounded by stromal tissue that contains fibroblasts. (B) The microarchitecture comprises of the upper and lower cell culture chambers separated by an ECM-derived membrane that mimics a basement membrane *in vivo* [60].

gories: chronic-transparent windows and *in situ* preparations. Depending on the experimental aim, an appropriate exogenous or endogenous molecular probe is used [61]. Intravital microscopy includes a number of techniques such as single-photon microscopy, multiphoton (MP) microscopy and optical frequency domain imaging. Among them, MP microscopy technique is a powerful tool that has provided unprecedented mechanistic insights into TME. It can be used to monitor and image the expression of specific protein (for example Second Harmonic Generation SHG for fibrillar collagen) and can be applied for the evaluation of different treatment strategies [10]. Intravital imaging can be also used to understand tumor cell invasion dynamics and how the native tumor environment can impact invasion and metastasis. SHG is an optically nonlinear coherent process where the emitted light has exactly half the wavelength of the two incident photons. The energy is thus conserved and no absorption occurs. This makes SHG a powerful tool for detecting and visualizing the 3D collagen network without labeling or staining. Collagen fiber type I has the crystalline and non-centrosymmetric properties required for generating the second-harmonic signal. Fibrillar collagen type I consists of a triple helical macromeolecule that self-assembles into fibrils

and fibers. The molecular organization, amount and distribution of fibrillar collagen type I are important for the structural and mechanical properties of tissue and play an important role in wound healing and in diseases such as cancer [62]. The other forms of collagen (II, III, V) can be stained by Picro-sirius red, an acidic dye, because they cannot be visualized by SHG technique for their loss crystallinity.

Many groups have incorporated two-photon techniques to analyze collagen SHG signals in an attempt to differentiate healthy and tumor tissue. Morphological collagen changes, such as the shape of fibrillar collagen or its orientation with regards to the border of primary tumor, have been investigated in order to differentiate between healthy and malignant tumors [13]. In particular, collagen changes at the tumor/stromal boundary can be imaged and classified as markers of mammary carcinoma progression, called tumor-associated collagen signatures (TACS). During tumor formation, mammary tumors exhibit a localized increase in collagen deposition near tumor lesion (termed TACS-1). It is unclear whether: 1) a pre-tumor dense region is present that serves to stimulate tumor formation, 2) the dense region of collagen is pulled into a grouped cluster through increased contraction of an epithelial tumor mass or motile cells at the tumor boundary, or 3) fibroblast activation results in increased local collagen deposition [40]. As tumor increases in size, a straightening of collagen fibers that are aligned parallel to the tumor boundary is noted (TACS-2). Remodeling of the stroma progresses to the final stage, which is the reorientation of collagen such that multiple collagen fibers are bundled and aligned perpendicular to the tumor boundary and promoted tumor invasion (termed TACS-3). TACS-3 corresponds to sites of focal invasion into the stroma. These specific definitions of TACS are consistent with the general and well-known feature of desmoplasia, a fibrous stromal deposition, surrounding tumors and help to identify breast tumors in experimental animal models as well as human cancer and fresh tumor biopsies [14] (Fig. 1.12).

Hompland et al. (2008), have studied the content and structure of colla-

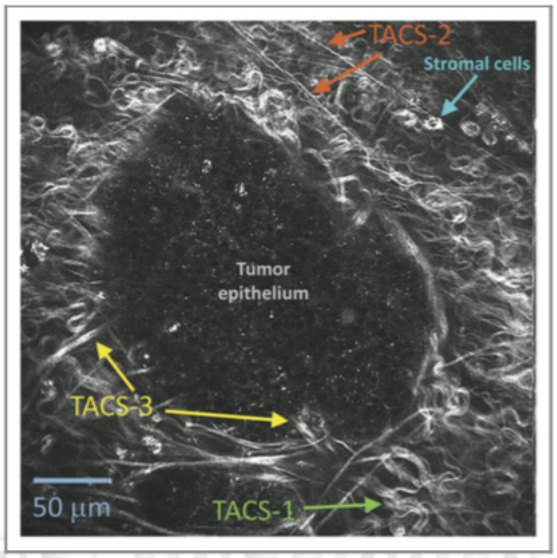

Figure 1.12: Tumor associated collagen signatures (TACS)[14].

gen by SHG signal in frozen sections from three tumor tissues (osteosarcoma, breast carcinoma and melanoma) and compared them with corresponding normal tissues (bone, breast, dermis/skin). They found a strikingly difference in collagen network between tumor and normal tissue, suggesting that the collagen network in tumor tissue have lost most of their normal functions. The osteosarcoma and breast carcinomas showed similar distributions. The collagen cap in the periphery represented approximately 50 to 60% of the area in this region, whereas only 0 to 9% of the section contained collagen farther into the tumor. The cap was formed by long collagen fibers oriented along the outer periphery and shorter fragments facing inward [62]. *Burke et al.* (2013), utilized a quantitative analysis of the ratio of forward and backward propagating SHG signal (F/B ratio) to monitor collagen throughout ductal and lobular carcinoma development. In ductal carcinoma, there is no significant alteration in fibrillar collagen microstructural properties compared to healthy breast tissue, but there is an alteration in them as the tumor progress from an *in situ* to an invasive carcinoma. This is consistent with the fact that the majority of SHG collagen fibers in healthy tissue are

surrounding the ducts, so as the tumor cells exclusively fill in the ducts in DCIS, the surrounding collagen microstructural properties remain relatively unaffected. It is only when the tumor cells begin to invade the breast tissue outside of the duct that they induce changes in microstructural properties of the surrounding fibrillar collagen. ILC, instead, causes a change in the fibrillar collagen microstructural properties in breast tissue, as indicated by a decrease in the F/B ratio relative to healthy tissue (Fig. 1.13) [13].

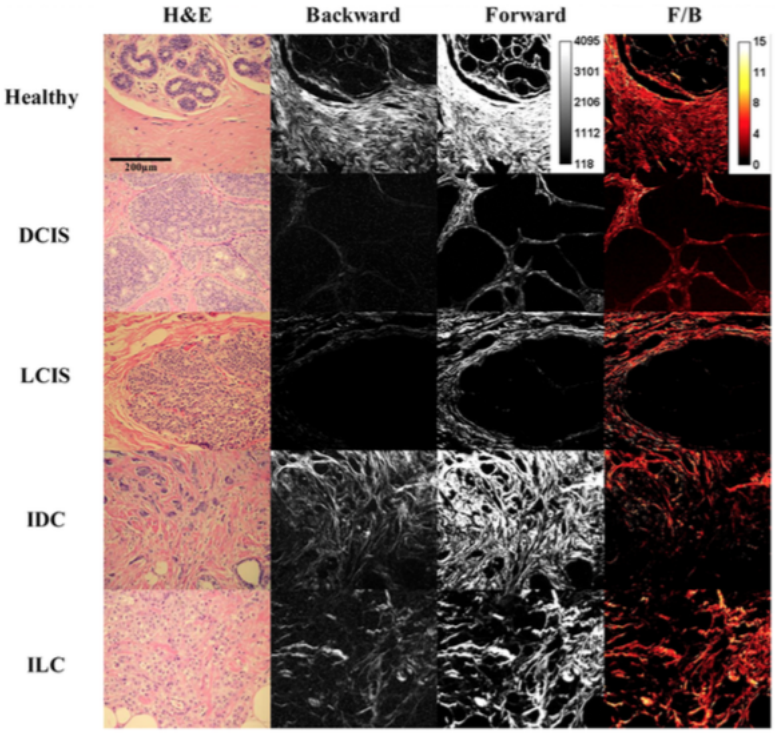

Figure 1.13: Sample images of five types of tissue analyzed: healthy tissue, DCIS, LCIS, IDC and ILC. The left column shows H-E staining, the middle columns show backward- and forward- scattered SHG, and the right column the F/B ratio image[13].

The morphology of collagen fibers revealed by SHG can also be quantitatively described by Texture analysis. Texture analysis approaches can be categorized into statistical, structural, model-based and transform-based methods. As the most frequently cited statistical method, the gray level co-

occurrence matrix (GLCM) has been applied to a variety of field for decades, including texture analysis to quantitatively analyze the collagen fibers. Generally, GLCM features along one or two of the four specific directions of 0 deg, 45 deg, 90 deg and 135 deg can be extracted to quantitatively analyze SHG images. Since the orientation is an important characteristic of collagen fibers with a filamentous structure, the GLCM features calculated along the dominant orientation of collagen fibers are different form those calculated along the other directions. By combining the dominant orientation of collagen fibers into GLCM analysis, the GLCM curves calculated may provide more information for detailed morphological characterization of the collagen fibers, thus leading to further sights into various physiological and pathological processes, such as the structural modification of the extracellular matrix during the migration and invasion of tumor cells [63].

Zhuo et al. (2010), established a quantitative link between collagen alteration and epithelial tumor progression using SHG microscopy. They found that SHG microscopy could provide quantitative features to effectively evaluate epithelial tumor progression and to determine the margin of tumor regions. To relate the collagen fibril structure, they used the correlation feature that is a measure of intensity correlation as a function of pixel distance. As seen in (Fig. 1.14), normal correlation fell off sharply with pixel distance indicating distinct, linear fibrils, whereas the precancerous and cancerous fibrils correlation remained elevated as pixel distance increased, implying less defined fibrillar structure [64].

Adur and co-workers (2014), showed similar results working with ovarian tumors. Using this methodology they found that it is possible to discriminate between cancerous and healthy tissue with clear cut distinctions between normal, benign, borderline and malignant tumors of serous and mucinous ovarian tumor types (Fig. 1.15) [65], [66].

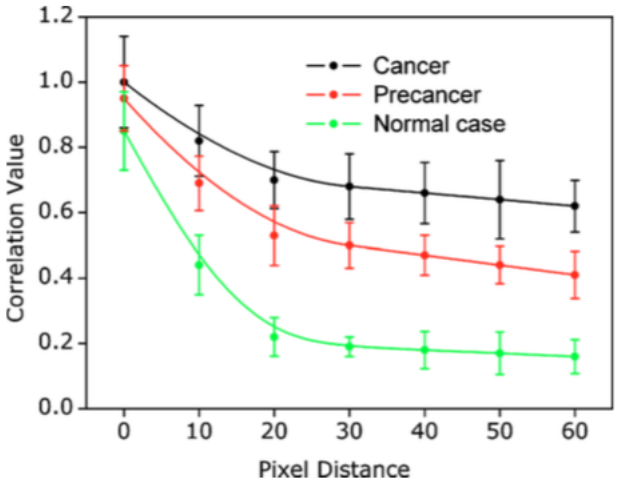

Figure 1.14: Correlation value as a function of pixel distance from normal, precancerous and cancerous epithelial tissues [64].

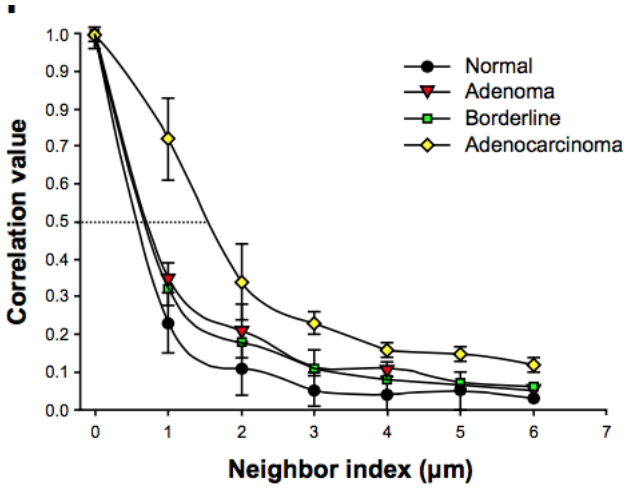

Figure 1.15: Correlation values in serous ovarian tumors versus distance [66].

1.5 Nanotechnology in cancer treatment and diagnosis

Conventional chemotherapeutic agents are distributed non-specifically in the body affecting both normal and tumoral cells. Given the potency of modern

pharmacological agents, tissue selectivity is a major issue. The ultimate goal of cancer therapeutics is to increase the survival time and the quality of life of the patient by reducing the systemic toxicity of chemotherapy. In this context, the tumor targeting of nanomedicine based therapeutics has emerged as one approach to overcome the lack of specificity of conventional chemotherapeutic agents [67]. The field of nanomedicine has recently attracted tremendous attention, particularly for applications in cancer drug delivery. Owing to the advancements in material science and new manufacturing methods, nanoparticle (NPs) drug delivery platforms can now be fabricated to an almost unlimited number of configurations with respect to size, shape, and payload, allowing for versatile applications for the detection, prevention and treatment in oncology [68]. Nanoparticles can be designed to target tumor cells, vasculature or different types of cells such as immune cells to achieve anti-tumor responses such as anti-angiogenic therapy, immunotherapy or cytotoxic therapy. In a systematic point of view of an *in vivo* system, it is necessary to understand how nanoparticles can target tumors, how they diffuse through the TME and how they interact with individual cells to perform their therapeutic function (Fig. 1.16) [69].

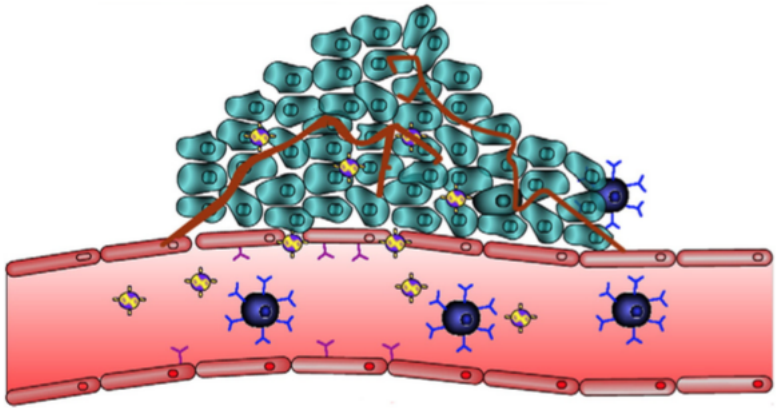

Figure 1.16: The concept of biomimetic tissue-engineered for evaluation of nano-based therapy. Colors: glod/blue: nanoparticle; green: cancer cells; red/pink: blood vessel, endothelial cells; blue: immune cells [69].

Several nanostructured particles are being developed for therapeutic applications with different chemical nature such as metallic, polymeric or ceramic and different morphologies such as nanospheres, nanorods, nanotubes, nanowires, nanocubes and nanocages. Their surface may be functionalized with biomolecules such as antibodies, peptides, oligonucleotides or polymers like PEG [69]. Nanotherapeutics such as liposomes, polymeric micelles and inorganic NPs possess a distinct functional advantage or conventional small molecule chemotherapy regimens by overcoming severe systemic toxicities that limit the clinical application of most chemotherapy drugs. Furthermore, nanoparticle drug delivery platforms permit significantly prolonged circulation when compared to small molecule drugs alone [68]. Recent advances in nanotechnology have led to the development of particles with controllable size and surface charge and with the potential to be used for cancer detection and treatment [70]. Examples of applications include both the preclinically investigated nanoformulation (liposomes, polymeric micelles) and FDA approved NPs of liposomal doxorubicin (Doxil) and albumin-bound paclitaxel (Abraxane) [68]. To achieve effective targeted drug delivery, various strategies have been proposed to exploit these pathophysiological characteristics of the TME. Currently NPs are designed based on so-called "passive" and "active" targeting strategies, which rely on increased extravasation and ligand-receptor interactions, respectively. The passive targeting is based on the fenestration and prolonged circulation by PEGylation. The term "active targeting" is used to describe a strategy bind to the target tumor cells or endothelium. Active targeting becomes effective only after the NPs reach the vicinity of the target tumors [9].

Now there is an emerging need for better understanding of how these particles diffuse in the ECM and for prediction of the particle properties that optimize their delivery to cancer cells [70].

1.5.1 Drug distribution in solid tumors

The complex TME poses multiple barriers that inhibit transport and action of drugs. First, the TME serves as a biophysical barrier that impedes effective transport of drugs to target cancer cells or associated stromal cells. After being administered into a patient's bloodstream, drugs are thought to be subjected to complex and multi-faceted transport processes prior to reaching the cancer cells [9]. In general, the intratumoral delivery of macromolecules and NPs require several steps in transport, including:

1. vascular transport;
2. transvascular transport;
3. interstitial transport;
4. cellular binding, internalization and metabolism [68] (Fig. 1.17).

1.17

Within the tumor stroma, convective and diffusive forces are intrinsic mediators of the biochemical landscape that sustains neoplastic development. The predominant conduits of mass transport, microvascular networks define the spatial distribution of oxygen, nutrients, endocrine signals, and therapeutic drugs. Moreover, as a consequence of diffusion-limited nutrient and waste transport, the absence of a functional vasculature regulates the development of hypoxia and acidosis during tumor initiation and at interior regions of advanced cancers [11]. Compared to healthy vasculature, tumor-associated blood vessels exhibit increased leakiness, tortuosity, instability via absence of mural cells and subsequent aberrant fluid mechanical forces. Notably, by contributing to elevated fluid pressure in the tumor, dysfunctional vasculature compromises drug delivery and modulates interstitial flow at the tumor margins [11]. To better understand the biophysical underpinnings of these transport barriers, *Jain and his colleagues* (2010), have developed several mathematical models to simulate the intratumoral behaviors of NP [71]. For the modeling of vessel and trans-vasculature transport, the tumor

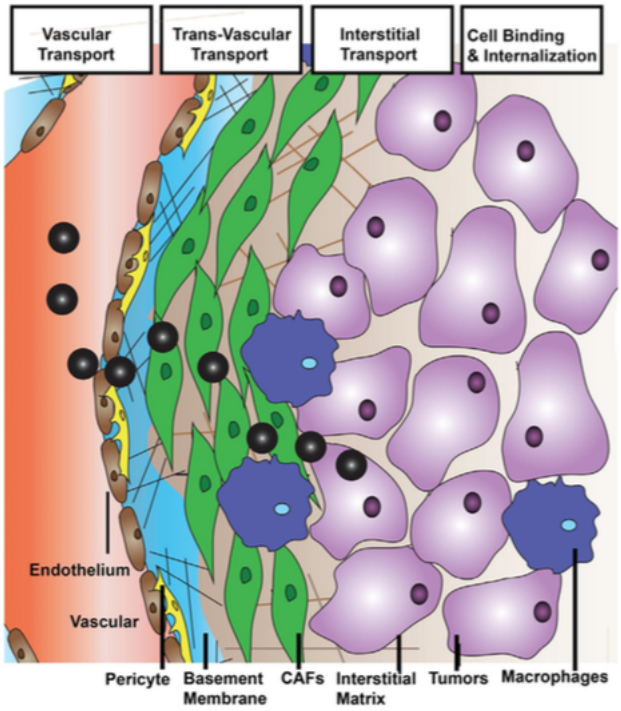

Figure 1.17: Scheme of NP intratumoral transport [68].

vasculature was represented by a two-dimensional percolation network with one inlet and one outlet that resembles the vascular structure and function of tumors. Vessel transport is mainly dominated by convection (flow rate governed by pressure gradient) and is quantified based on the perfusion rate of blood flow (Q). Poiseuille's law was used to simulate vessel transport, suggesting that blood flow is proportional to the vascular pressure gradient and blood viscosity [68]. The transvascular flow was set proportional to hydraulic conductivity of the vessel wall, the surface area of the vessel and also the influence of IFP. Interstitial transport, mainly indicating the diffusion of NP through the ECM toward tumor cell targets, is another significant step in determining NP penetration [68]. This phenomena is dependent on convection and diffusion [41]. The sum of convective J_C and diffusive J_D fluxes is given by the following equation (Darcy's theory):

$$J_s = J_D + J_C = -D\nabla C + v_f f C \tag{1.1}$$

where D is the effective diffusion coefficient, C is the solute concentration, f is the retardation coefficient, and v_f is the interstitial fluid velocity, determined by the solution to the Brinkman equation for flow through porous media:

$$\mu\nabla^2 v_f - \frac{v_f}{K} - \nabla\rho = 0 \tag{1.2}$$

where μ is the fluid viscosity, K is the hydraulic conductivity and ρ is the hydrostatic pressure difference between the vascular and lymphatic vessels [41]. After extravasation, the drug is transported through the tumor interstitial space against elevated tumor IFP and abnormal ECM structure. The IFP of a solid tumor stays at an elevated level and sharply decreases at the periphery of the tumor [9].

In general, diffusion of macromolecules or NP in the ECM was modeled *in vitro* using matrigel or collagen confined diffusion chamber models. Diffusion coefficients were determined using these *in vitro* ECM models by non-linear fits of intensity gradients to a diffusion model (Fickian model) or can be quantified *in vivo* using either single-photon Fluorescence Recovery After Photobleaching (FRAP) or two-photon Fluorescence Correlation Spectroscopy (FCS) [68]. Convection depends on gradients of pressure (both hydrostatic and osmotic) between vascular and interstitial space; vessel permeability and the surface area of exchange. In the case of tumor, the combination of leaky vasculature and dense ECM increases IFP and inhibits convection-mediated transport. Consequently, drug-delivery within tumor stroma primarily depends on diffusion. Hypoxia can also induce the activation of cell survival or pro-angiogenic genes, leading to certain populations of cells that become drug-resistant. Additionally, drugs that rely on an oxygen-based free-radical mechanism cannot function on cells in a hypoxic (oxygen low) environment. pH is also low in the extracellular space of hypoxic tumors, causing weakly basic drugs to become protonated, hindering their ability to cross the cell membrane. Composition and organization of the tumor ECM can also determine whether drugs can penetrate into the tumor. Exces-

sive ECM deposition due to fibrotic remodeling physically hinders diffusion of large anti-tumor molecules through the interstitium [41]. However, dense cellular and matrix components represent diffusion barriers that hinder transport through the interstitium in conjunction with elevated IFP (Fig. 1.18). Specific parameters that regulate diffusion efficiency through the stroma include: 1) diffusion distance, 2) available volume fraction of pores (accessible space where molecules can pass through), 3) tortuosity of pathway, 4) hydrodynamic resistance, and 5) ECM affinity of the molecule of interest. All of these parameters are affected by tumor stroma remodeling. For example, desmoplasia-mediated enhancement of ECM density and structural changes decrease the available volume fraction of pores and increase the tortuosity of the void space, both of which reduce the rate of diffusion through the stroma [41].

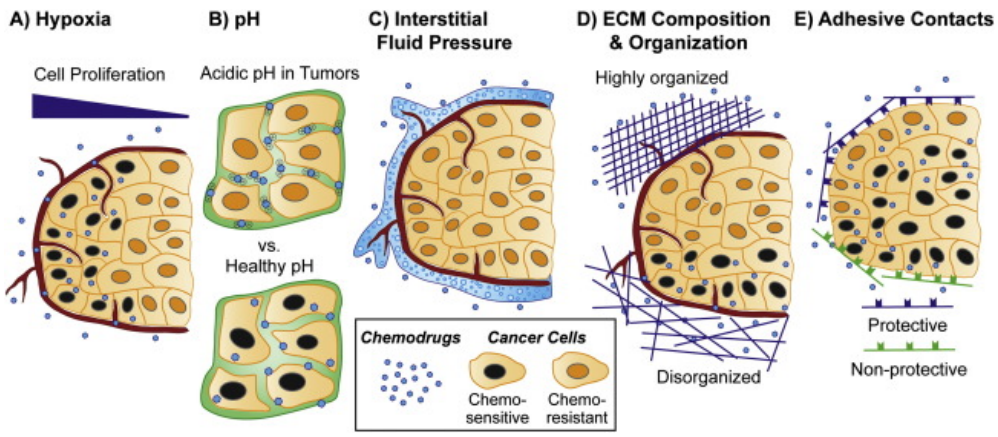

Figure 1.18: ECM-conferred barriers to treatment [25].

Furthermore, properties of drugs (size, charge and configuration) influence the diffusion of drug [41]. Drugs or molecular probes perform Brownian random walks through the spaces between network structures and are influenced by components of the matrix in three distinct ways: 1) they collide with matrix fibers (steric interactions); 2) as they diffuse near fibers, restricted thermal motion of water molecules due to proximity to the fibers slows their diffusion (hydrodynamic interactions) and 3) for charged parti-

cles, electrostatic interactions with charged components of the ECM contribute an additional force [70]. *Stylianopoulos et al.* (2010), presented a mathematical framework to study the effect of charge on the diffusive transport of macromolecules and NP in the ECM of biological tissues. The TME consists of fibers whose diameter ranges from a few nanometers (HA, collagen oligomers) up to a few micrometers (collagen fibers) and their charge can be either positive (collagen) or negative (HA). Therefore, neutral particles should diffuse faster than cationic. Since cationic particles are preferred because they target tumor vessels, the optimal NP for delivery to tumor tissue should be initially cationic to selectively target tumor vessels, but change charge to neutral after entering the ECM [70]. Diffusion of drugs is also limited by binding in tissue or by their rapid metabolism once they have extravasated. An important determinant of drug distribution within tissue is the half-life of the drug in the circulation; drugs having a long half-life have a better opportunity to achieve equilibrium within TME [72]. For example, the poor penetration through tissue of a most common used drug, doxorubicin, is due to binding to DNA and sequestration in acidic endosomes of cells that are proximal to the vasculature [73]. The specific structure of ECM components also modulates diffusion fluxes of therapeutic molecules. Analysis of collagen fiber orientation via SHG revealed that increased malignancy is associated with collagen fiber re-orientation. While collagen in initiating tumors is characterized by isotropic orientation, progression leads to tangential and ultimately radial alignment in expanded and invading tumors, respectively. These changes in ECM fiber network orientation can promote diffusion anisotropy without affecting the overall diffusion coefficient of the drug. For example, fibers tangentially aligned to the tumor boundary could redirect drug diffusion away from the tumor and therefore, impair therapy efficacy during the initial stage of tumorigenesis. Theoretically, radially aligned fibers should mediate the opposite effect; however at this stage tumor cells may have developed resistance phenomena rendering them unresponsive to therapy. The opportunity for enhancing drug transport by modifying tumor

matrix was demonstrated in a mouse model of pancreatic cancer, where gemcitabine delivery was improved through depletion of desmoplastic stroma by inhibition of Hedgehog signaling [74]. A recent report by *Lu et al.* (2015), indicated that cellular density is another factor affecting interstitial transport. Densely packed tumor cells induce a solid stress and reduce the interstitial space for NP transport [68]. Many anticancer drugs exert their action by binding to macromolecules. Earlier studies using tumor cell spheroids have shown that penetration of protein-binding drugs such as doxorubicin and paclitaxel is limited to the periphery [75]. High binding affinities between drugs and the target site are generally seen as an advantage by increasing the internalization of drug. However, the use of targeted drug with high binding affinity may elicit a binding site barrier. This regards a phenomenon where drug binding to target cells paradoxically reduces diffusion deep into tumors [68]. Once the drugs are transported through the tumor interstitial space, they should act on tumor cells, but their efficacy may also be limited due to complete or partial drug resistance. Multidrug resistance (MDR) is thought to be caused by a group of membrane proteins that extrude cytotoxic molecules, thus maintaining the intracellular drug concentration below effective levels. These proteins belong to the ATP binding cassette superfamily of membrane transporters, most of which use the energy of ATP hydrolysis for the efflux of drugs (active transport). This family includes the well-characterized P-glycoprotein (Pgp) encoded by MDR-1 gene, the multidrug resistance protein (MRP) and the mitoxantrone resistance protein (MXR), also known as the breast cancer resistance protein (BCRP). In addition to the over-expression of these transporter proteins, cellular drug resistance also appears to be mediated by the binding of tumor cells to the ECM [9].

Chapter 2

Metabolic activity, mechanical properties and ECM composition evolution of spheroid and microtissue model

2.1 Introduction

The progression of cancer is no longer being considered as an independent event which only relates to the genetic mutation and uncontrollable growth of cancer cells [76]. There is growing evidence that biological behavior of cancer cells, such as proliferation, invasion and metastasis, is profoundly influenced by the presence of host stromal cells [2]. Among stromal cells, fibroblasts are the major components that surround cancer cells [2]. It is well known that fibroblasts play an important role in the carcinogenic process [77]. In addition to provide a mechanical support, fibroblasts are also involved in the deposition of extracellular matrix (ECM), in controlling proliferation and invasion of cancer cells as well as in enhancing of therapy resistance [78], [2]. On the other side, fibroblasts undergo changes in the upregulation of a variety of molecules such as growth factors, matrix degrading enzymes, an-

giogenic factors and cytokines in stromal compartment [79]. This dynamic interplay between tumor and fibroblasts cells is probably due to a substantial phenotypic transformation from normal to activated cancer fibroblasts (CAF) [80]. Furthermore, during tumorigenesis, the continuous remodeling of ECM by CAF contribute in modifying mechanical properties of stromal fibroblasts [81]. As the same time, tissue mechanosignaling activates protumorigenic signal pathways that simultaneously promote carcinogenesis and metabolic alterations [81]. CAF play an active role in supporting metabolic reprogramming of tumor cells by recycling products of anaerobic metabolism in order to sustain cell survival [82]. For these reasons, the complex mechanisms of tumor progression cannot be investigated without the presence of tumor stroma [83]. It has been widely demonstrated that the complexity and heterogeneity of the tumor microenvironment cannot be replicated in two-dimensional (2D) models due to unreliable clinical response [84]. On the contrary, three-dimensional (3D) culturing methods provide a valid alternative to better recapitulate *in vitro* the *in vivo* structure of tumor tissue [85]. Whereas the morphological properties and cell-matrix interactions of tumor and stromal cells are flattened in 2D systems, these aspects can be reliably distinguished when cells are cultured as aggregates (spheroids), grown on 3D scaffold materials, or embedded in gels [86]. Among them, spheroids are the most used models in cancer research. Despite their success, they have experimental limitations since only few works incorporate stromal cells in spheroid models [87]. As result of progresses in tissue engineering, some research groups are focused on the realization of scaffold materials to create a more reliable 3D cancer models [44]. Microtissue precursors (μTP) are an example of scaffold-based tissue model [51]. In such models, cells are induced to grow onto microcarriers surface and within their pores are able to synthesize endogenous ECM under controlled culture conditions [6].

In this work we focalize only on the stromal component of tumor microenvironment consisting of fibroblasts. In particular normal fibroblasts and CAF are seeded on porous gelatin microcarriers in a dynamic culture

system according to previous works [6], [51]. In parallel the same typology of cells were grown in spheroid configuration. The intention is to monitor the dynamic evolution of the metabolic activity, mechanical properties and ECM compositions in both investigated models (spheroids and μTP). Interestingly, only in μTP configuration phenotypic differences between normal and activated fibroblasts were found.

2.2 Materials and Methods

2.2.1 Cell type

Human normal mammary fibroblasts (NF) and cancer associated fibroblast (CAF), kindly donated by Kojima's group, were sub-cultured onto 150 mm Petri dishes in Dulbecco's Modified Eagle Medium (DMEM) with high glucose, containing 10% fetal bovine serum, 100 μg/ml L-glutamine, 100 U/ml penicillin/streptomycin. Cells were maintained at 37 °C in humidified atmosphere containing 5% CO_2.

2.2.2 Microscaffold production

Gelatin porous microbeads (GPMs) have been prepared according to a modified double emulsion protocol (O/W/O) [88]. GPMs have been stabilized by crosslink reaction with GPMs glyceraldehydes (GAL), in order to make them stable in aqueous environment at 37 °C, as previously described [6]. GAL at 5% w/w of the microbeads has been used to perform all the experiments.

2.2.3 Homotypic cell culture

All cell cultures on microscaffolds were performed in spinner flask (Integra). For homotypic culture (NF, and CAF) 50 mg of GPMs were loaded together with $7.5*10^5$ cells (30 cell/GMP ratio). To promote cell seeding on GMPs an intermittent stirring regime (30 min at 0 rpm, 5 min at 30 rpm) for 6 h has been performed. To monitor the seeding efficiency during the post-inoculum

time, the disappearance of free cells from the inoculated spinner cultures was calculated as $[(C_0 - C_t) * 100]/C_0$ where C_0 is the concentration of the cells at the inoculum time and C_t the concentration of the cells in the culture medium. Then, dynamic cultures were kept under continuous stirring at 30 rpm for up to 12 days. Medium was changed on the first day and every 3 days until the end of the experiments. From the second day of dynamic culture, 50 μg/ml of ascorbic acid were added. Microtissues (μTP) samples were taken for further investigations at days 1, 4, 8 and 12 for homotypic cultures and fixed.

2.2.4 Spheroid formation

Cells were trypsin-treated and counted. Subsequently, they were seeded onto round bottom non-tissue culture treated 96 well-plates (Falcon, BD NJ, USA) at a concentration of 2500 cells/well in DMEM High Glucose, 10% FCS supplemented with 20% methyl cellulose stock solution. For preparation of methylcellulose stock solution we autoclaved 3 grams of methylcellulose powder (M0512, Sigma-Aldrich) in a 250 ml bottle containing a magnetic stirrer. The autoclaved methylcellulose was dissolved in preheated 125 ml basal medium (60 °C) for 20 min (using the magnetic stirrer). Thereafter, 125 ml medium (RT) containing double amount of FCS (20%) was added to a final volume of 250 ml and the whole solution mixed overnight at 4 °C. The final stock solution was aliquoted and cleared by centrifugation (5000 g, 2 h, RT). Only the clear highly viscous supernatant was used for the spheroid assay (about $90 - 95\%$ of the stock solution). For spheroid generation we used 0.24% methylcellulose. Spheroids were grown under standard culture conditions (5% CO_2, at 37 °C) and harvested at different time points for further investigations.

2.2.5 Tissue micromodules/entities morphology

A 200 μl aliquot of NF and CAF μTP homotypic culture at time 4, 8 and 12 day on a 35 mm Petri dish were observed with a light microscope (Olympus, BX53). Ten images were taken at the same magnification for each sample at every time-point. 1 ml of μTP and spheroids suspension was fixed in a solution of 10% neutral buffered formalin for 1 h at RT, dehydrated in an incremental series of ethanol (75%, 85%, 95% and 100% twice, each step 30 min at RT) treated with xylene and paraffin embedded. Successively, the samples were sectioned at a thickness of 7 μm. Masson's trichrome (Sigma Aldrich) staining was performed according to standard protocols. At last, the sections were mounted with Histomount Mounting Solution (Bioptica) on coverslips and the morphological features of μTP and spheroids were observed with a light microscope (Olympus, BX53).

2.2.6 Cell proliferation

At the day 1, 4, 8 and 12 of culture, 1 ml aliquots were collected for cell growth monitoring on the GPM. Briefly, 200 μl of the same aliquots was transferred to a cell culture dish (w/2 mm grid Nunc) for microcarrier counting, after which the microcarrier suspension was placed in a new 2 ml tube and washed twice with PBS. To detach cells from microcarriers, μTP were digested by collagenase A (Roche Life sciences, Italy) 60 min at 37 °C, centrifuged 5 min at 2000 rpm, and incubated 5 min in Trypsin (Lonza, Italy). The detached cells were then counted using a hemocytometer. In the same way, a 96-well plate (Falcon, BD NJ, USA) of NF and CAF spheroids was trypsin-digested for each time point in order to obtain the cell number for spheroids at each time-point.

2.2.7 Oxygen consumption kinetics measurement

In order to evaluate the oxygen consumption kinetics, a known amount of NF and CAF μTP, and NF and CAF spheroids were spilled from the spin-

ner flask and round bottom 96 well-plates respectively at day 4, 8 and 12 days of culture and placed in three different vials of frosted glass. The vials were filled with fresh culture medium, placed in an incubator and kept at 37 °C, under gentle agitation. The vials were, then, sealed in order to avoid oxygen exchange with the surrounding environment. The decrease of oxygen concentration in the medium, due to cell metabolism, was measured by means of an optical detector (OXY-4 PreSens) placed in the vials. The measurements were performed until the oxygen was completely consumed. The oxygen consumption took place in 4-5 h depending upon the number of μTP and spheroids used. The partial pressure was converted in oxygen concentration (mM) by means of Henry's law. As a control, the same measurements were performed in three vials containing only medium at the same conditions. In parallel, a known amount of μTP and spheroids were enzymatically treated and the cell number was counted in order to obtain the cell number per μTP and spheroid respectively. By performing centred time derivative of the oxygen concentration curve, it was possible to obtain the plot of the consumption rate versus the oxygen concentration for each construct. This curve was fitted by the following Michelis-Menten Eq. 3.1:

$$R = \frac{\rho V_{max} C}{K_m + C} \tag{2.1}$$

where ρ is the cell number divided by the volume of the vial, V_{max} is the maximum rate of consumption, K_m is the oxygen concentration at which the rate of oxygen consumption is half of the V_{max} value and C is the oxygen concentration. The fitting parameters were V_{max} and K_m.

2.2.8 Evaluation of pH tissue microenvironment

The pH value of the culture medium was read out for both NF μTP and spheroids and CAF μTP and spheroids respectively. For each tissue construct, the culture mediums were collected from spinner flask and round bottom 96 well-plates and the corresponding pH were read by using a pH-meter (mettler-toledo) respectively at day 4, 8 and 12 days of culture. A

simple of 5 ml of NF and CAF μTP were spilled by spinner flask after cell seeding and placed in a low attachment petri dish (corning) until the 4th day for first acquisition point. In parallel, the mediums of 25 wells of NF and CAF spheroids were collected for pH measure. The μTP and spheroids were enzymatically treated and the cell numbers were counted in order to obtain the total cell number for each construct. The pH, closely depend upon the cell number and the culture medium volume, whereby the value was converted in [H+] expressed in mol/L following the Eq. 3.2:

$$[H^+] = 10^{-pH} \tag{2.2}$$

In order to obtain the contribution of H^+ ions per cell ($'H^+$), $[H^+]$ was multiplied by the total volume of culture medium and divided by the total cell number for each tissue model following the Eq. 3.7

$$'H^+ = \frac{[H^+]V}{N} \tag{2.3}$$

where V is the total volume of culture medium and N is the total cell number in the spinnes flask. This operation was repeated at 8 and 12 days, and each measure was repeated in three independent experiments.

2.2.9 Multi-particle tracking

A custom-made multiple particles tracking microrheology (MPT) apparatus was used to probe the local mechanics of the cytoplasm by monitoring and tracking the motion of particles embedded in the samples. Fluorescent polystyrene particles (100 nm Polyscience) were shot in the cells using a ballistic gun (Bio-Rad, Hercules, CA). Helium gas at 2200 psi was used to force a macrocarrier disk coated with particles to crash into a stopping screen. The force of collision was transferred to the particles, causing their dissociation from the macrocarrier and the bombardment of the cells. Then, the samples were placed in a microscope stage-incubator at a controlled temperature and CO_2 (37 °C and 5%, respectively). Movies of embedded particles were

recorded via a gated intensified highspeed camera (Lambert Instruments, Roden, The Netherlands) mounted on an inverted epifluorescence microscope (Olympus IX70, Olympus, Melville, NY) at 100 X magnification. The displacements of particle centroids were monitored by a time-lapse acquisition of 6 s at a rate of 50 frames per second. Movies of particles were analyzed by a self-developed algorithm in Matlab (Matlab 6). It detects each position in every frame by intensity measurements and links this point detection into trajectories, based on the principle that the closest positions in successive frames belong to the same particle (proximity principle). Once the trajectories had been obtained, mean square displacements (MSD) described by the Eq. 3.8:

$$MSD =< \Delta r^2 >=< [x(t-\tau) - x(t)]^2 + [y(t-\tau) - y(t)]^2 > \qquad (2.4)$$

were obtained. In the Equation 3.8 the symbol " <> " means time average, is the time scale and t the elapsed time. The MSD provides information about the mechanical properties of cytoplasmatic environments. Indeed, it was demonstrated that the MSD amplitude is inversely related to the rheological properties of living cells [89] here we evaluated MSD after 12 days of culture to gather information about the mechanical organization of the cells in each configuration.

2.2.10 Multiphoton imaging

Two-photon excited fluorescence was used to induce Second Harmonic Generation (SHG) and obtain high-resolution images of unstained collagen structures in μTP' ECM. Homotypic μTP samples were used for SHG analysis. Hence, all the samples were imaged by two-photon excited fluorescence at λex = 840 nm to induce SHG of unstained neo-synthesized collagen structures by collecting the emission wavelength in the range λem = 420 $\pm$ 5 nm.

2.2.11 Collagen amount quantification

SHG images from NF and CAF μTP and NF and CAF spheroids were analyzed by using ImageJ software. In order to quantify the collagen fraction in the endogenous ECM, for μTP images, the ROI were chosen by excluding the signal rising from the microbeads. The collagen portion in the ECM space was represented by the bright pixels (N_c) in grayscale rising from the SHG signal, while the non-collagen portion appeared as black pixels (N_b). We define collagen fraction (CF) as the ratio between bright pixels to total pixels in the selected ROI, as reported in Eq. 3.9:

$$CF = \frac{N_c}{N_c + N_b} \tag{2.5}$$

where N_c and N_b represent the number of pixels from the collagen and non collagen portion, respectively.

2.2.12 Evaluation of collagen assembly degree

The degree of collagen assembly (CAD) network was evaluated by analyzing the intensity of the SHG signal. The analysis was performed within the μTP space where the SHG signal was present. All SHG images were subjected to noise subtraction and the average intensity in the two different zones was evaluated as described by the Eq. 2.6:

$$CAD = \frac{\sum_{i=1}^{255} I_i p_i}{\sum_{i=1}^{255} p_i} \tag{2.6}$$

where CAD is proportional to I the average intensity, I_i is the intensity corresponding to the pixel p_i, while the index $i = x_i y_i$ runs in the gray value interval from 1 to 255. The intensity I of collagen network is known to be proportional to the degree of assembly of the newly synthesized collagen.

2.2.13 Immunostaining

For immunofluorescence staining, formalin-fixed and paraffin embedded μTP and spheroids slices were unmasked by heat antigen retrieval protocol by citrate buffer; washed with PBS containing 0.2% Triton X-100, blocked with FBS and 5% BSA solution and incubated with sheep anti-human Hyaluronic acid and mouse anti-human Fibronectin. All the antibody were purchased at Abcam (UK). Secondary antibody incubation and DAPI staining were performed, before closing the slices with glycerol solution.

2.2.14 Statistical analysis

Data are expressed as mean $\pm$ standard deviation and show the results from three independent experiments. Differences between groups were determined using one-way analysis of variance (ANOVA). Significance between groups was established for $p < 0.05$ after Tukey's post test.

2.3 Results

2.3.1 Time evolution of μTP and spheroids stroma models

The μTP and spheroids models evolution was evaluated during 12 days of culture. The bright field images of the NF-μTP (Fig. 2.1 A-C) highlighted that the size did not change during culture time, although in the spinner flask the culture conditions promote the aggregation phenomena. The unchanged size was due to the balance between the aggregation and contraction phenomena caused by cells activity. Concerning CAF-μTP (Fig. 2.1 D-F) the contraction was more predominant in comparison to the aggregation phenomena, leading to a size reduction during time. Instead for the both spheroids models, such as NF-sph (Fig. 2.1 G-I) and CAF-sph (Fig. 2.1 L-N) the final size was the same as the initial size.

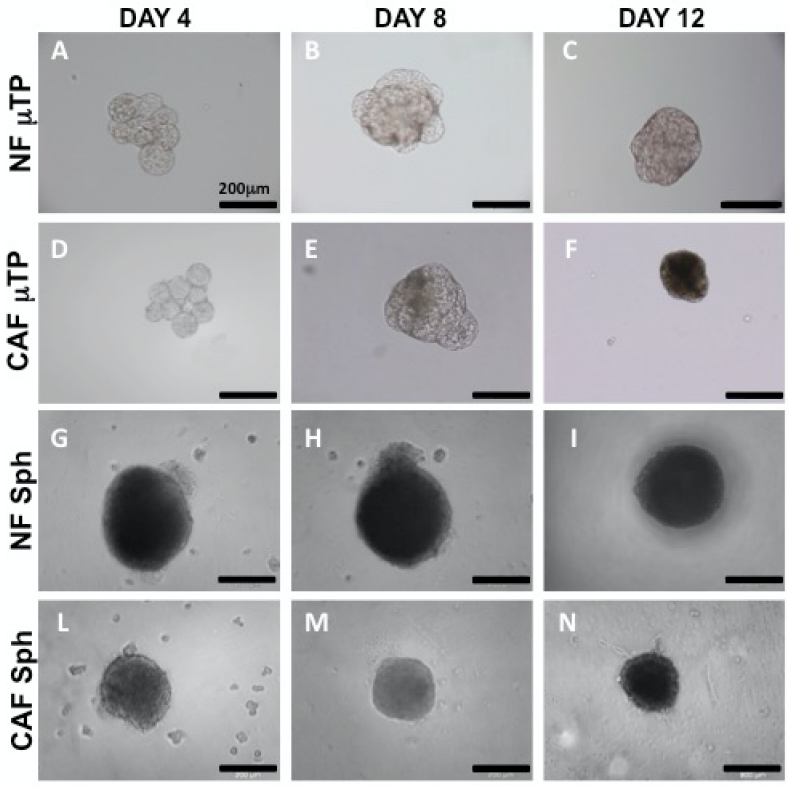

Figure 2.1: Brightfield images of time evolution morphology of NF-μTP (A-C), CAF-μTP (D-F), NF-sph (G-I) and CAF-sph (L-N) at day 4,8 and 12.

Fig. 2.2 reported the histological sections stained by Masson's trichrome of the four compared models. In particular for the both NF-μTP (Fig. 2.2 A-C) and for CAF-μTP (Fig. 2.2 D-F) was possible to distinguish the red signal related to the microbeads, the purple signal due to the cells staining and blue signal of the endogenous ECM. On the contrary, for both spheroids models NF-sph (Fig. 2.2 G-I) and CAF-sph (Fig. 2.2 L-N), the Masson's trichrome staining showed mostly a cellular aggregate in which just few blue pixels were detected.

In Fig. 2.3 was reported the fold change of the growth curve per unit; for the both NF-sph and CAF-sph the cells number remained constant during the investigate time window, in particular, as reported in the Table 2.1, they started with 2300 $\pm$ 103 and 2400 $\pm$ 93 cells respectively at day 1, and after

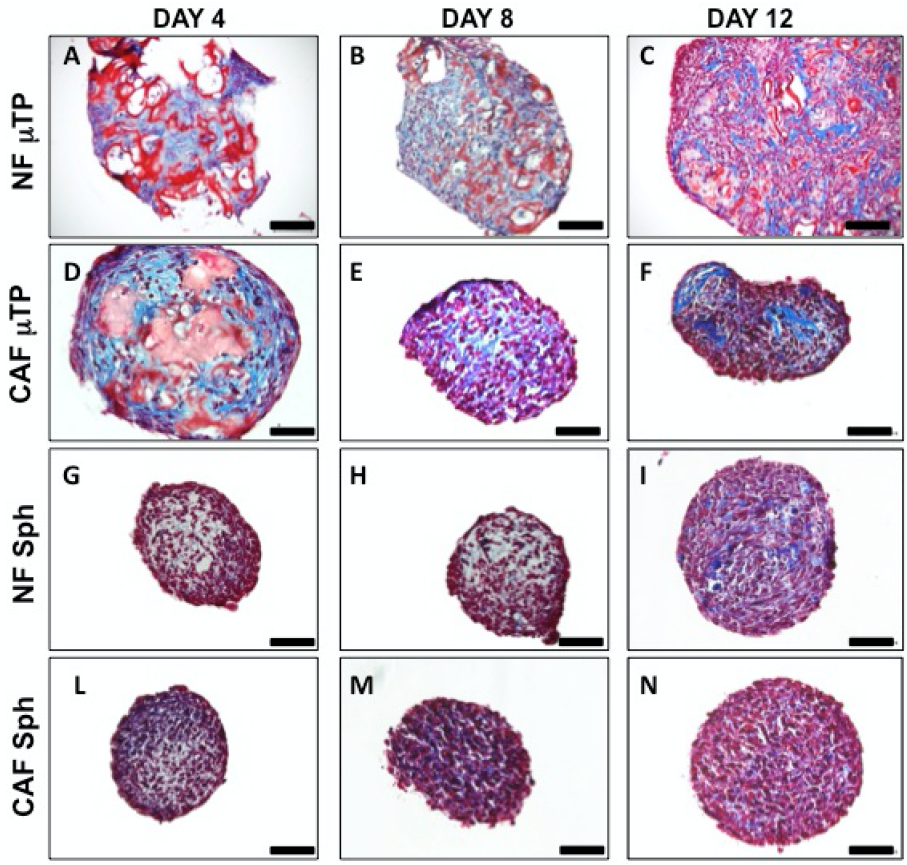

Figure 2.2: Masson's Trichrome staining images of matrix composition evolution in NF-μTP (A-C), CAF-μTP (D-F), NF-sph (G-I) and CAF-sph (L-N) at day 4, 8 and 12.

12 days of culture they present a final cells number of 2000 $\pm$ 116 and 1600 $\pm$ 126 without any statistical difference. The NF- and CAF-μTP showed a different trend, in particular NF-μTP started from 36 $\pm$ 7.8 cells/microbead up to 830 $\pm$ 14 cells/microbead. The growth curve showed how, in this model, between 8 and 12 days no statistical difference was detected, evidencing that between this two time points the cells were in the stationary phase. On the other hand, CAF-μTP started from 30 $\pm$ 1.7 cells/microbead up to 950 $\pm$ 88 cells/microbead, but in this model, the cells were still in exponential phase (Fig. 2.3).

Table 2.1: Cell growth in μTP and spheroids.

Type	Day 1	Day 4	Day 8	Day 12
NF μTP	$3.6 \pm 7.8 * 10^1$	$2.3 \pm 40 * 10^2$	$7.5 \pm 100 * 10^2$	$8.3 \pm 14 * 10^2$
CAF μTP	$3 \pm 17 * 10^1$	$6 \pm 70 * 10^1$	$2 \pm 24 * 10^2$	$9.5 \pm 88 * 10^2$
NF spheroids	$2.3 \pm 103 * 10^3$	$1.1 \pm 114 * 10^3$	$1.8 \pm 98 * 10^3$	$2.0 \pm 116 * 10^3$
CAF spheroids	$2.2 \pm 93 * 10^3$	$2.4 \pm 86 * 10^3$	$1.7 \pm 115 * 10^3$	$1.6 \pm 126 * 10^3$

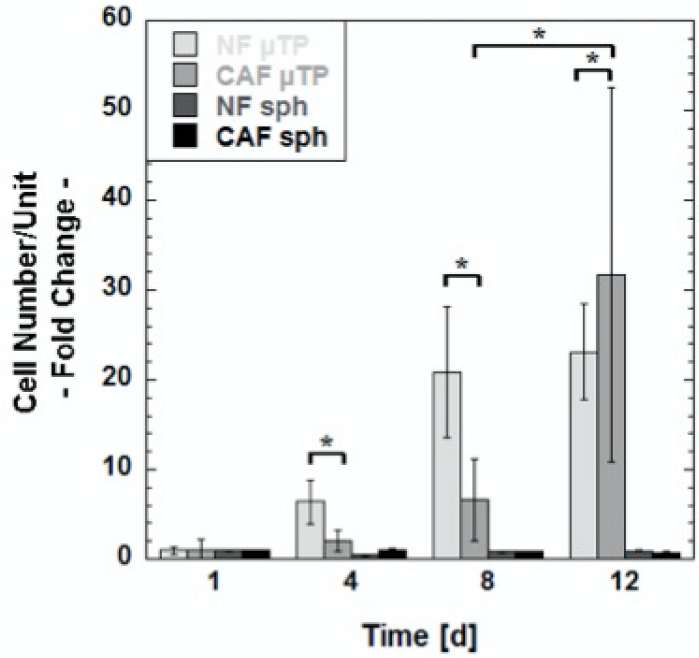

Figure 2.3: Cell number per unit (μTP or spheroids, fold change) from day 1 to day 12.

2.3.2 Metabolic activity

The Fig. 2.4 A-B showed the maximum oxygen consumption rate (V_{max}) for each model, in particular in Fig. 2.4 A the V_{max} trends were reported for the μTP models (NF and CAF); in Fig. 2.4 B the V_{max} trends were reported for the spheroids models (NF and CAF). For all models investigated the measured trend is the same, in particular at day 4 the V_{max} value was highest respect to the next measured values, while between 8 and 12 days

the difference of the oxygen consumption rate was less marked for spheroids models compared to μTP models. In particular, the V_{max} trend for CAF-μTP is statistically higher than NF-μTP, the initial measured values were $8.85 * 10^{-8} \pm 1.77 * 10^{-8}$ and $2.31 * 10{-}8 \pm 6.15 * 10^{-9}$ respectively, while the final values were $2.65 * 10^{-8} \pm 7.90 * 10^{-9}$ and $3.58 * 10^{-9} \pm 1.42 * 10^{-9}$ respectively.

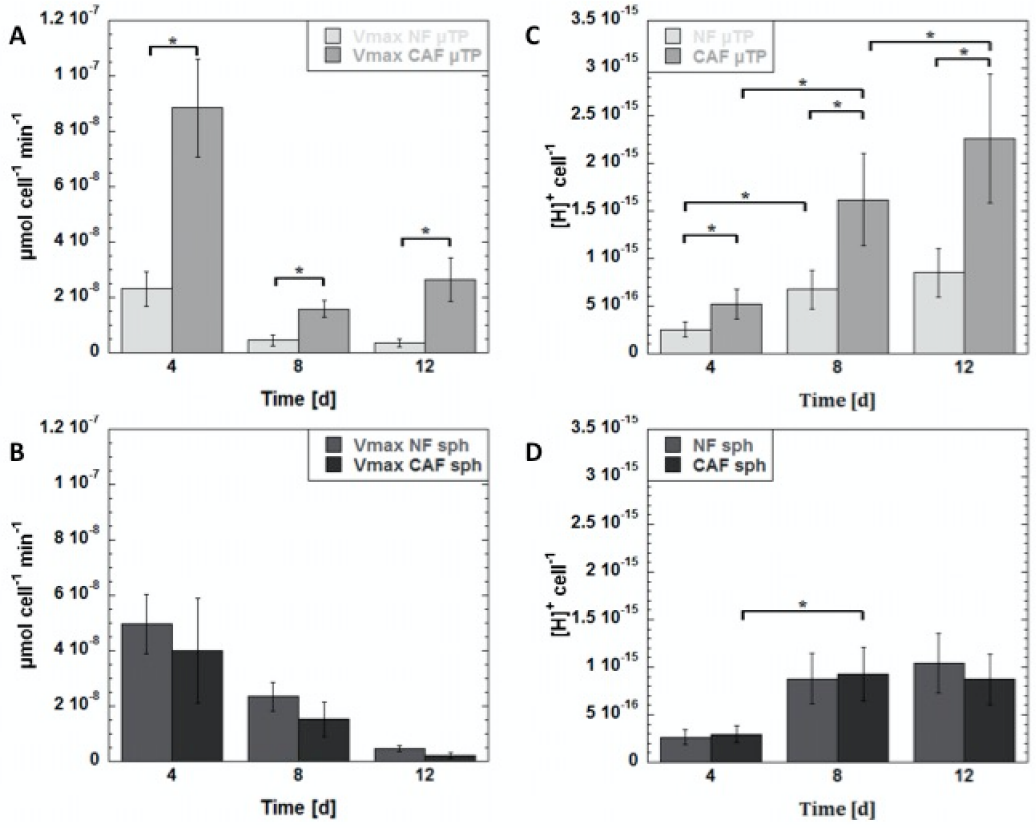

Figure 2.4: Maximum rate of oxigen consumption - V_{max} - over culture time in NF- and CAF-μTP (A) and in NF- and CAF- sph (B); contribution of H^+ ions per cell in NF- and CAF-μTP (C) and in NF- and CAF- sph (D).

However, though these differences in V_{max} value, were detected in μTP models, due to the cells activities, they become undetectable in spheroids models. Indeed the V_{max} values for CAF-sph and NF-sph were not statistically different; the initial measured values were $4.01 * 10^{-8} \pm 1.89 * 10^{-8}$ and

$4.98 * 10^{-8} \pm 1.07 * 10^{-8}$ respectively up to $2.13 * 10^{-9} \pm 1.01 * 10^{-9}$ and $4.69 * 10^{-9} \pm 1.01 * 10^{-9}$ respectively as final value. The Fig. 2.4 C-D reported the quantitative contribution of each cell to the acidification of the medium for μTP models and spheroids models respectively; concerning the NF-μTP model, a variation between first two time points was detectable, while no difference reported between 8 and 12 days, and the final measured value was $8.51 * 10^{-16} \pm 2.55 * 10^{-16}$. On the contrary, for CAF-μTP model, the trend was always growing during time and the final value of $2.26 * 10^{-15}$ was considerably higher than the corresponding value for NF-μTP. Furthermore, for the spheroids models the trend was comparable with NF-μTP trend, and in any time point no statistical differences were detected.

2.3.3 ECM composition and architecture

The analysis of the composition and architecture of the ECM was performed at the end point (12 days of culture). In Fig. 2.5 A-D were reported the SHG images rising from newly formed collagen signal in the NF-μTP (Fig. 2.5 A) and CAF-μTP (Fig. 2.5 B) to NF-sph (Fig. 2.5 C) and CAF-sph (Fig. 2.5 D). SHG was used to estimate the collagen fraction (CF, according to Eq. 2.5) in the ECM that was reported in Fig. 2.5 E; concerning NF-μTP and CAF-μTP, a statistical significance ($p < 0.05$) was found between quantified values of 40% $\pm$ 11% and 54% $\pm$ 9% respectively, while, for each spheroid model very low/no collagen fraction was detected. Furthermore from SHG images it was also possibile to have information about the collagen assembling degree (CAD, Fig. 2.5 F), in particular, according to Eq. 2.6, the measured CAD was highest for the NF-μTP (18.65% $\pm$ 7.15%) and was about doubled if compared with the CAF-μTP (10.83% $\pm$ 3.20%). As mentioned before, for spheroids models this kind of analysis gave values close to zero. In parallel, to evaluate the effect of matrix stiffness on NF and CAF cells biophysical properties, MPT technique was used to probe their mechanical properties. MSD analysis reported in Fig. 2.6 A showed that there was a significant difference in the distance traveled by the particles probes embedded in cyto-

plasmic environment between NF- and CAF-μTP ($8.2 * 10^{-5} \pm 8.99 * 10^{-6}$ and $1.14 * 10^{-4} \pm 1.99 * 10^{-5}$ respectively; this difference was not detectable for the NF-sph and CAF-sph ($4.1 * 10^{-5} \pm 1.94 * 10^{-5}$ and $3.13 * 10^{-5} \pm 1.66 * 10^{-5}$) (Fig. 2.6 B). To verify the intrinsic cellular features, NF and CAF cells were cultured in 2D systems, on polyacrylamide matrices of varying Young's modulus, 3 kPa (Fig. 2.6 C) and 30 kPa (Fig. 2.6 D).

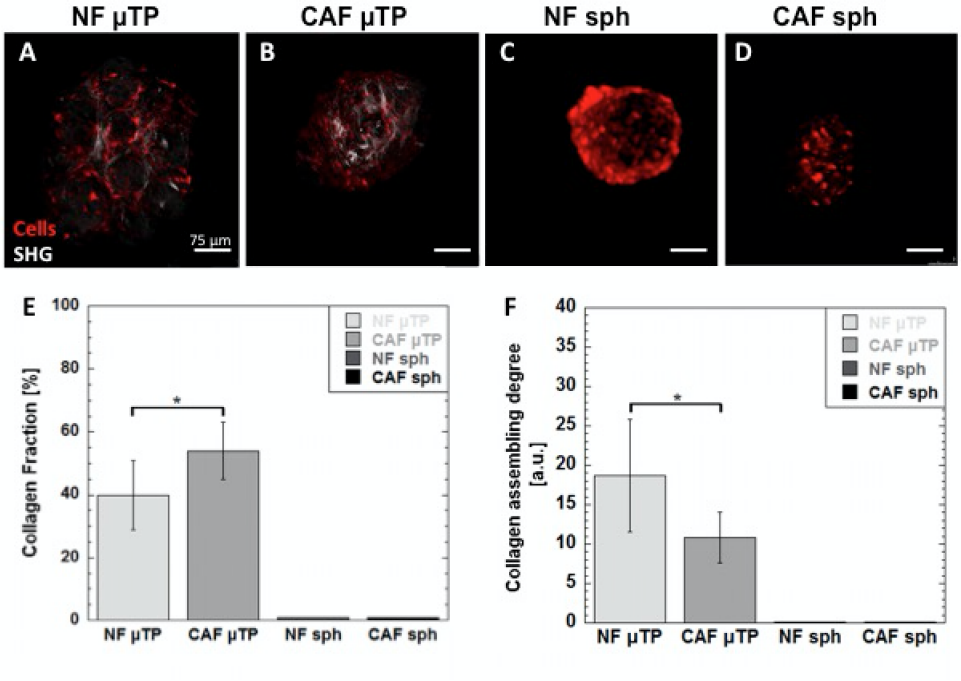

Figure 2.5: SHG (gray scale) and fluorescence (cells in red) images of NF-μTP (A), CAF-μTP (B), NF-sph (C) and CAF-sph (D) at day 12; Collagen fraction - CF - (E) and Collagen assembly degree - CAD - (F) in the newly formed ECM in NF- and CAF- μTP and spheroids.

Particle tracking experiments showed that substrate stiffness modulation significantly affects the dynamics of cell embedded tracers both in NF and CAF. In particular, we measured MSD at τ equal to 0.1 s and the analyses revealed that MSD decreased with increasing substrate stiffness in both cell lines. As already said, the MSD is indirectly correlated to the mechanical properties of intracellular environment, then the reduction of MSD on softer

substrates was probably due to a dynamic remodeling of cytoskeleton, that resulted to be less dense and assembled. These findings indicated that not only NF, but also CAF cells preserved their ability to detect and respond to the matrix elasticity, through a process known as "stiffness sensing".

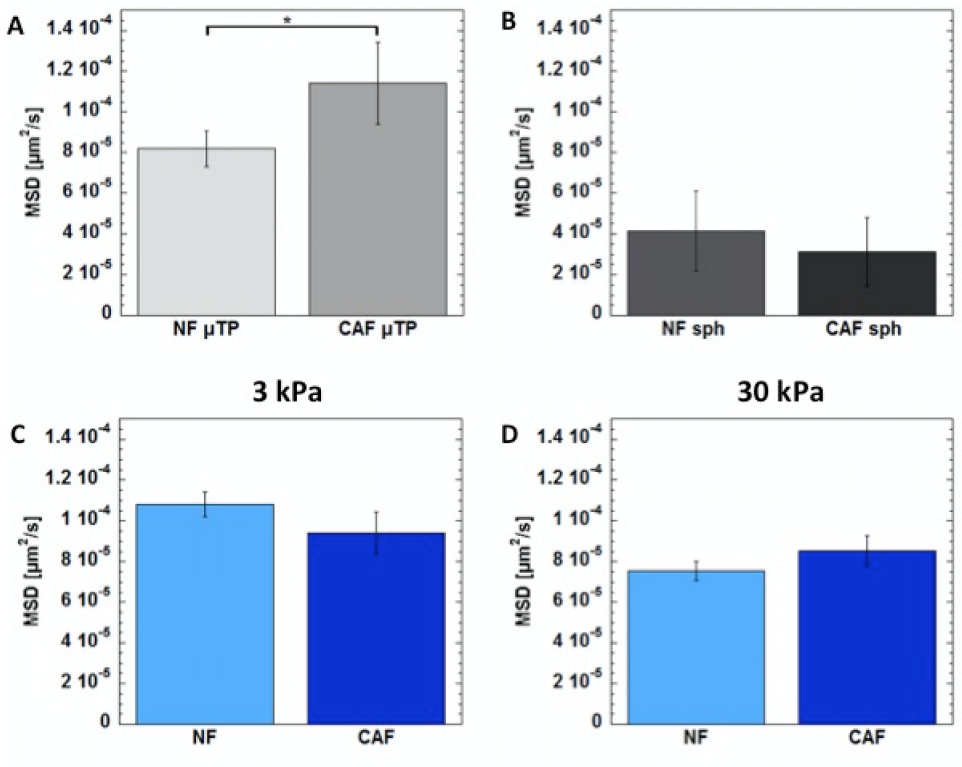

Figure 2.6: MSD values of 500-nm diameter particles at τ equal to 0.1 s in NF- and CAF-μTP (A), in NF- and CAF sph (B) and in NF and CAF cells seeded on 3 (C) and 30 (D) kPa polyacrylamide substrates. The data were presented as media $\pm$ standard error considering the number of observations greater to 100.

To test whether CAF transformation was also reflected in their biophysical properties, we compared MSD of particles embedded in NF and CAF when the cells were on the same stiffness substrate. We found no significant difference between MSD values of particles embedded in normal and cancer associated fibroblasts both on 3 and 30 kPa substrates (Fig. 2.6 C-D). These

results suggested that the activation of cancer fibroblasts was not related to an alteration of their mechanical properties and cytoskeletal organization and a loss of their "stiffness sensing" ability. Thus, it is reasonable that the measured mechanical properties of cancer and normal spheroids were not different, because related principally to the intrinsic properties of NF and CAF cells. In the case of μTP, we think that the mechanical phenotype of cancer fibroblasts was changed by their ability to sense a matrix that was softer, because of a minor content and assembly of protein components. This evidence supported the hypothesis that the cells were responsive in terms of cytoskeleton stiffness respect to the substrate stiffness, whereby the increasing of the MSD for both μTP models was due to the presence of the ECM. Furthermore the increase of the particles mobility corresponded to a variation of the stiffness of the matrix, indeed the highest value was found in CAF-μTP that presented a less assembled ECM.

2.3.4 ECM complexity

Along collagen detection, ECM components as fibronectin and hyaluronic acid were analyzed in stromal μTP and spheroids. In Fig. 2.7 A-B the immunofluorescence staining showed that the fibronectin expression was higher in CAF-μTP in comparison to NF-μTP. On the other hand, few pixels were detected in the case of stromal spheroids (Fig. 2.7 C-D). The ratio between fibronectin/nuclei for μTP and spheroids was highlighted in the graphic in the Fig. 2.7 E, in particular fibronectin/nuclei ratio in NF-μTP and CAF-μTP was 520.4 $\pm$ 331.7 and 2317.8 $\pm$ 547.4, respectively. Otherwise, fibronectin/nuclei ratio in NF-sph and CAF-sph was 73.4 $\pm$ 30.7 and 225.4 $\pm$ 99.3, respectively.

Concerning hyaluronic acid, Fig. 2.8 A-B showed the different fluorescent staining in NF-μTP and CAF-μTP. For stromal μTP, hyaluronic acid is overexpressed in CAF-μTP rather than NF-μTP. On the other hand, there was no difference between the expression of hyaluronic acid in NF-sph and CAF-sph (Fig. 2.8 C-D). Fig. 2.8 E showed the values of the hyaluronic acid

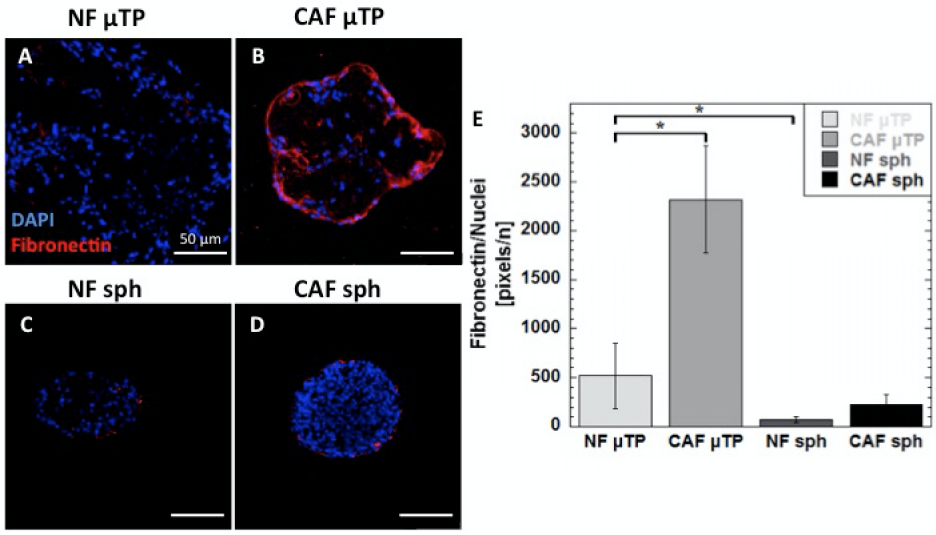

Figure 2.7: Immunofluorescence staining of Fibronectin protein (red) in NF- (A) and CAF-μTP (B), in NF- (C) and CAF sph (D); quantification analysis of Fibronectin obtained from immunofluorescence images (E).

pixels per nuclei in stromal μTP and spheroids. In particular the ratio of hyaluronic acid pixels per nuclei was 636.3 $\pm$ 276.7 and 3861.8 $\pm$ 719.7 for NF-μTP and CAF-μTP, respectively, while it was 225.2 $\pm$ 99.3 and 262.70 $\pm$ 143.7 for NF-sph and CAF-sph, respectively.

2.4 Discussions

In this work, NF and CAF cells were used to create two kinds of 3D models: microtissues and spheroids. μTP were fabricated by seeding each cell line within gelatin porous microbeads. In a previous work, we have already demonstrated that the interactions among fibroblasts and microscaffolds triggered mechanotrasduction pathways involved in collagen remodeling [6]. Consequently, fibroblasts synthesize new collagen molecules and remodeled their microenvironment [6]. Spheroids are cellular aggregates largely used to simulate 3D architecture of solid tumor better than the conventional

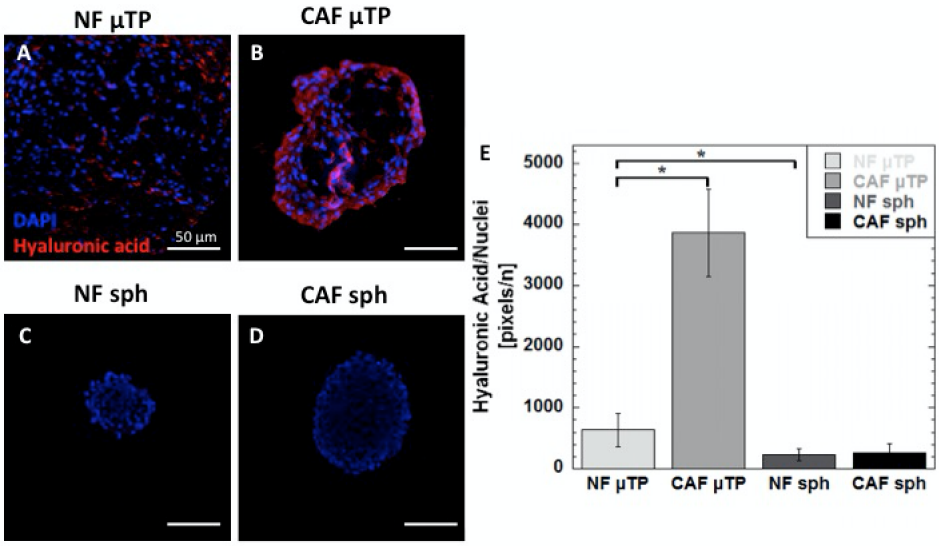

Figure 2.8: Immunofluorescence staining of Hyaluronic Acid protein (red) in NF- (A) and CAF-μTP (B), in NF- (C) and CAF-sph (D); quantification analysis of Hyaluronic Acid obtained from immunofluorescence images (E).

monolayer cell culture [90]. Arranging the cells in these two 3D models, different behaviors in terms of metabolic activity, mechanical properties and ECM remodeling were detected. Indeed, the 3D environment in which the cells grow, plays a crucial role in maintaining their own characteristics, and the different architecture of the model gives back different global features. In terms of size, spheroids, independently from the cells used to build up the model, present a low contraction capability; indeed the cells are closely arranged and engaged in intercellular membranes contacts and cell-cell junctions [86]. On the other hand, for μTP models, the contraction phenomena, related to force generation, migratory behavior, focal adhesion formation and cytoskeleton organization are evident. In particular the highest contraction is detectable in CAF-μTP model, in which the activated cell contraction is governed, as in tumor connective environment, by the balance between four biophysical processes: generation of contractile forces, transmission of the contractile forces via integrins to the surrounding extracellular matrix, the

cytoskeleton remodeling, and enzymatic degradation of the matrix network [37]. The spheroids, due to their structure, do not present an increasing of the total cells number, indeed, despite a consistent number of cells of the more external layer were under duplication cycle, the replacement occurs through the expulsion of the cells that migrate outside the model. On the contrary, the μTP are made starting from few cells that are able to duplicate themselves, and the microbeads surface allows the proliferation without replacement. Furthermore, the different nature of the used cells (NF and CAF) means two different trends; in particular the CAF cells retain the greater proliferative capability such as tumor associate cells *in vivo* [91]. From the metabolic point of view, the oxygen consumption rate of the CAF-μTP result constantly higher than NF-μTP, probably due to the evidence that in tumor activated cells, the metabolic pathways in which the oxygen is a substrate, are faster than health cells (i.e. duplication, nucleotide synthesis, migration, fatty-acid synthesis) [92]. Moreover, the tumor cells produce ATP molecules not by oxidative phosphorylation, but by glycolysis pathway also in the presence of abundant oxygen, a phenomenon known as aerobic glycolysis or the "Warburg effect" [82]. This metabolic pathway is 16 times less efficient than oxidative phosphorylation, but 200 times faster, indeed in the time unit leads to obtain 13 times more ATP molecules. Our results correlate with recent findings reporting the higher consumption of glucose in CAF rather than normal fibroblasts, as well as the increased production of lactate. Recent evidences introduced the new idea, anmely "Reverse Warburg Effect", suggesting that aerobic glycolysis may be performed by cancer associated fibroblasts, reather than by epithelial cancer cells themselves [93]. Interestingly, previous metabolic studies with skin myofibroblasts have demonstrated that they perform aerobic glycolysis, with increased glucose uptake and lactate secretion, suggesting that the "Reverse Warburg Effect" may be a general feature of both myofibroblasts and CAF [94]. Since CAF seems to be deputed to the metabolic request and the cancer cells activated the normal stroma, turning it into a factory for the production of energy-rich metabolites for

cancer progression and angiogenesis, it became important to replicate tumor model *in vitro* where the fibroblastic stromal component is not negligible. In this scenario, lactate secretion released in the extracellular space leads to an acidification of the environment that can be considerate an indirect proof of the metabolic activity a powerful predictive biomarker for recurrence, metastasis and poor clinical outcome [95]. Again, our stroma model, both normal and tumoral, is able to maintain the pathophysiological differences founded *in vivo* and used as model for the study of tumor progression or as a tool for drug testing. In our results we have shown how a difference between health ad cancer activated fibroblasts was detectable only in μTP configuration; as a consequence we can deduce that, although phenotypically different, the cells are no longer able to reproduce *in vivo* phenomena in spheroid model. It has already known that cells immediately adjacent to a tumor were no more considered a passive structural element. Indeed, recent studies assessed that contrary to being an idle spectator, the surrounding microenvironment, actively contributes to tumor progression. Furthermore, tumor progression is sustained by a reciprocal paracrine loop between CAF and cancer cells. Cancer cells trigger the fibroblast-activated phenotype which, in turn, produces a series of growth factors and cytokines that sustain tumor progression by promoting ECM remodeling, cell proliferation, angiogenesis and EMT. On the basis of evidence reported in this work, we could assess that only a 3D model as μTP that take into account the presence of endogenous ECM, with regulatory functions could recapitulate the real microenvironment, both in physiological and pathological features. In this context the ECM plays a pivotal role, indeed only in the μTP models the cells are engaged in ECM remodeling phenomena. In spheroid model, although there are the ECM proteins, they are much less expressed than μTP and non-correctly assembled. This substantial difference between these two models has an impact also in cellular mechanical properties, in particular the MSD results show how, only in μTP configuration, the cells are able to change their own mechanical properties in relationship to the different assembly degree of the ECM.

In particular, CAF-μTP present an ECM less assembled and consequently the MSD are higher than NF-μTP, indicating a less structured cytoskeleton [96]; on the contrary, the NF structure their cytoskeleton respect to a hard substrate (more assembled ECM). These findings demonstrated how the different organization of ECM in μTP configuration influences the mechanical properties of cells [97]. Our results demonstrate how, arranged in spheroids architecture, the cells show the same MSD value, this represent a strong limitation for this model that worse replicate the *in vivo* environment and depress the morphological and metabolic differences between the NF and CAF. Collagen, primarily type I collagen, is capable of producing an SHG signal that can be detected in biological samples and used as a technique for monitoring the changes in ECM structure throughout tumor development [13]. Collagen I is a peculiar marker for fibrosis in several type of cancer and we are able to fabricate 3D μTP where collagen is over expressed by CAF in comparison to NF. However we cannot support the 3D spheroid model that do not show the SHG signal for Collagen I. In order to validate the ECM features and the difference between normal and tumoral stromal 3D model, we decided to analyze as the expression of fibronectin and hyaluronic acid, two relevant ECM components. These ECM components have been shown to be over-expressed in tumor microenvironment. Fibronectin can be a ligand for several integrins and regulates collagen fibril structure; moreover, its expression has been associated to tumor metastatic potential and MMP secretion, playing important roles in cell adhesion, migration and growth [31]. CAF mediated the overexpression of hyaluronic acid within the tumor microenvironment, and played a role in the recruitment of cancer-associated macrophages, which are key regulatory cells involved in cancer angiogenesis through endothelial cell recruitment [16]. Moreover, as previously reported, tumor cells prefer anaerobic metabolism and generate lactate, even in the presence of oxygen. Lactate could induce fibroblasts to deposit hyaluronan and to express CD44, thereby participating in the process of cancer invasion and metastasis [98]. The right modulation of these ECM proteins in μTP but

not in spheroid models, made the former a valuable tool for the recapitulation of *in vivo* microenvironment. Indeed in μTP fibronectin and hyaluronic acid not only were expressed and organized within the ECM but also were over-expressed in CAF-μTP, resembling the tumor microenvironment. Thus, cancer cannot be considered as a result of deregulation of intracellular signaling pathways, because ECM exerts a regulatory activity on cell fate and the pathological derailment that leads to cancer transformation. Due to the relevant and essential role of ECM in tumor progression it become necessary fabricate tumor model that take into account the role of the ECM and stroma cells in terms of metabolism, mechanical properties and ECM composition in order to validate new therapeutics or study the tumor growth and metastasis.

2.5 Conclusions

In this work normal and tumoral microtissues were compared to the respective spheroids. Different behaviors in terms of metabolic activity, mechanical properties and ECM remodeling were detected. In particular, only in μTP configuration, we found differences between normal and activated fibroblasts. From the metabolic point of view, only when CAF are present in μTP configuration, show an alteration in metabolic energy compared to normal counterparts. Furthermore only in μTP model the stromal cells are able to produce and synthesize endogenous ECM that has an impact also in cellular mechanical properties. In spheroid model, although there are the ECM proteins, they are much less expressed than μTP and non-correctly assembled. Therefore although phenotypically different, the cells are no longer able to reproduce *in vivo* phenomena in spheroid model. These findings represent a strong limitation for spheroid model that worse replicate the *in vivo* environment and depress the morphological and metabolic differences between the NF and CAF. On the basis of evidence reported in this work, we can assess that the μTP model is adaptable as a valuable tool for the recapitulation of tumor microenvironment *in vitro*.

Chapter 3

On-line monitoring of transport properties and ECM remodelling of tumor activated stroma in a chip

3.1 Introduction

Tumor microenvironment and its interactions with cancer cells plays an essential roles in tumor progression and metastasis [99]. Stroma and extra cellular matrix (ECM) represent a pivotal and dynamic elements of such tumor microenvironment [31]. Indeed, tumor stroma orchestrates the interactions rising among such different cell types and, in turn, undergoes several alterations during tumor cell migration and invasion [100]. To date, one of the most relevant weaknesses of the *in vitro* tumor models is the non-recapitulation of the ECM-associated dynamics featuring the tumor microenvironment, during tumor progression. One of such ECM-associated dynamics concerns the ECM remodeling itself, occurring when tumor cells invade the surrounding stroma. As tumor evolves, the stroma undergoes a transition from "healthy" to "activated" status, changing its architecture, composition

and transport properties aiding the tumor progression by means of a reciprocity mechanism [31], [43]. Due to its active role in cancer progression and invasion, tumor stroma and its mutation during tumorigenesis, are becoming one of the main target in cancer therapy [101], [102]. The lacking of reliable *in vitro* model prevents the opportunities to investigate and therapeutically target such clinically relevant pathological target. Indeed, tumor response *in vitro* is still studied basically at cellular level [59], making the animal models the only milieu in which stroma modification can be taken into account [103]. To date, two-dimensional (2D) monolayer and three-dimensional (3D) model (spheroids, cell-populated biomatrices) have been extensively used as tumor model *in vitro* [43], showing several limitations. In particular, in 2D systems and 3D spheroids the most relevant biological interactions are restricted to cell-cell interactions while the cell-ECM ones result almost absent. At last, cells embedded in 3D gel of ECM-derived biopolymers (*i.e.* collagen, Matrigel) have the advantageous in that the ECM composition and cell types can be tailored to the disease under investigation; nevertheless, due to their exogenous character fail in replicating both the structural and the morphological changes occurring during pathologic events [104]. For this reason both on line and off line extrapolation of the architectural, morphological and other physical parameters concerning the ECM modification is denied. The stroma evolution can be currently detected only in xenograft animal models coupled with non-invasive optical techniques such as multiphoton microscopy or optical coherence tomography [61], [105], [106]. On the other hand, animal models exhibit significant drawbacks including cost, time consuming, unpredictable characteristics and difficulty in correlating observed results with human responses [59], [60]. In this scenario microfluidic technology has enabled the development of promising in vitro platforms that address the challenges of reconstituting, integrating, and interrogating many variables of the tumor microenvironment [59]. Microfluidic devices can be fabricated in a compartmentalized fashion creating cell-cell interfaces recapitulating specific cellular cross talk, under controlled laminar flow [59]. Furthermore, they

enable studying of complex phenomena such as drug distribution and penetration [107], [57] or vascular network growth / ingrowth in 3D matrices [108]. Additionally, optical accessible microdevices enable *in situ* imaging of living cultures with high spatiotemporal resolution [109], [110]. In this direction, several studies have incorporated the aforementioned *in vitro* model in the microfluidic device to simulate the complex stroma-cancer relationship [59], [60], [109], [111] and evaluate the efficacy of potential therapeutics against cancer pathology [57], [59], [60], [112]. With the aim of measuring in real time the ECM dynamics associated to the stroma activation, in this work we replicated the cross-talk between epithelial tumor and the surrounding stroma in a chip. The optically accessible microfluidic chip hosted two compartments for accommodating stromal and tumor microtissues respectively, separated by an interface that allows their physical contact. The 3D stromal microtissues are composed by an engineered system in which fibroblasts are continuously engaged in synthesizing, assembling and disassembling their own ECM [51], [113]. The combination of such innovative 3D microtissues with microfluidic technology, allowed us to detect in real time the modification occurring at ECM level via confocal and multiphoton microscopy. We found that the stroma tissue underwent the same modification found *in vivo* at both cellular and extracellular level. In particular, it was investigated the production of hyaluronic acid and fibronectin; the real time investigation of both collagen network architecture and the related variation of the diffusion coefficient by *in situ* fluorescence recovery after photobleaching (FRAP) technique.

I

3.2 Materials and Methods

3.2.1 Microfluidic device design and fabrication

An optical accessible microfluidic device was designed by means of computer-aided design software. It was conceived in order to allow the culture of 3D-

μTP under dynamic flow conditions. Fig. 3.1 shows the configuration of the microfluidic device composed of two chambers (inner/tumor chamber 370 x 780 x 300 μm and outer/stromal chamber 1200 x 1370 x 300 μm) for 3D-μTP accommodation, separated by arrays of regularly spaced posts (120 x 120 x 300 μm).

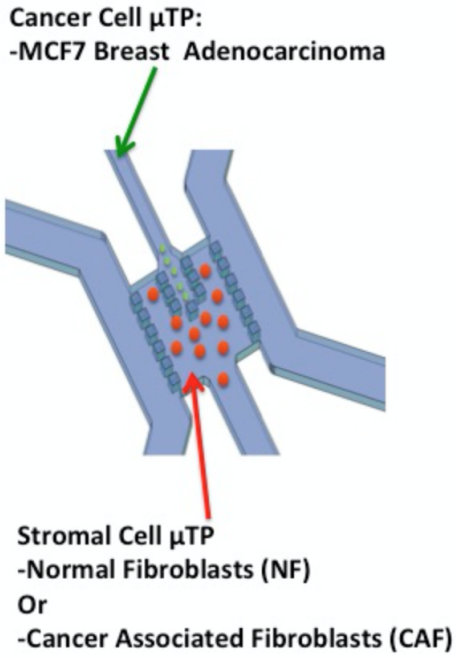

Figure 3.1: Schematic representation of the microfluidic device for 3D microtissue loading. The microfluidic system is composed of two chambers for tumor and stromal μTP accommodation and two lateral media channels.

The two chambers were provided by a dedicated channel for loading 3D-μTP (200 x 4000 x 300 μm and 400 x 4000 x 300 μm for tumor and stromal loading respectively), while the other two lateral channels (500 x 1800 x 300 μm) allowed the culture medium to flow guaranteeing nutrient supply and waste removal. Before fabrication, the file CAD was converted into file CAM using DESKAM software. The microfluidic device was created by replica molding technique. The master was carved onto a Poly(methyl methacry-

late) (PMMA, Goodfellow) slab with a micromilling machine (Minitech CNC Mini-Mill). Polydimethylsiloxane PDMS (Sylgard 184, Mascherpa) base and curing agent were mixed thoroughly in the weight ratio 10:1, degassed under vacuum for 20 minutes in order to remove unwanted air bubbles. Then the liquid PDMS was carefully poured on PMMA master and cured in an oven for 1 h at 80°C. After cooling, the PDMS layer was gently peeled off from the master. Inlet and outlet holes were made by punching through the PDMS with a 1.5 mm and 2.5 mm biopsy punch (DifaCooper) for chambers and lateral channels, respectively. The PDMS layer and a coverslip (Menzel-Glaser 24 x 60 mm, # 1.5) were bonded by oxygen plasma treatment for 1 min at 50 W in an oxygen plasma oven (Plasma Femto, Diener). After the plasma treatment the device was maintained at 80°C in the oven for at least 1 h to strengthen the bond.

3.2.2 Stromal and tumor 3D-μTP production

Cell line

Normal mammary fibroblasts (NF) and cancer associated fibroblast (CAF), kindly donated by Kojima's group, were sub-cultured onto 150 mm Petri dishes in Dulbecco's Modified Eagle Medium with high glucose, containing 10% fetal bovine serum, 100 μg/ml L-glutamine, 100 U/ml penicillin/ streptomycin. Human breast adenocarcinoma cells (MCF7) were kindly donated by Daidone's group and sub-cultured in RPMI-1640 (Roswell Park Memorial Institute) medium supplemented with 10% fetal bovine serum, 100 μg/ml L-glutamine, 100 U/ml penicillin/ streptomycin. Cells were maintained at 37°C in humidified atmosphere containing 5% CO_2. Fibroblasts were stable transfected with pLVX-DsRed-express2-N1 (Î»ex 554nm, λem 591nm) viral vector, while MCF7 cells were transfected with pLVX-ZsGreen1-N1 (λex 493nm, λem 505 nm). Viral vector were purchased at Clontech, USA. Three kinds of μTP were produced: NF-μTP, CAF-μTP and MCF7-μTP. For 3D-μTP production three dynamic spinner cultures in parallel were performed

by seeding NF, CAF or MCF7 cells on gelatin porous microcarriers (GPMs) as previously reported [6].

Microscaffold production

The microscaffolds were produced by following a previously established protocol [6]. For the of this work microscaffolds at 5% w/w of crosslink have been used to perform all the experiments. Before using, dry microscaffolds were sterilized in absolute ethanol 24 h on a rotating plate. Then, microscaffolds were washed twice in sterile phosphate-buffered saline (PBS) without calcium and magnesium solution. Finally, before cell seeding, PBS was replaced with fresh culture medium.

3D-μTP production

Spinner flask bioreactors were used to fabricate 3D-μTP. For each spinner culture 50 mg of microscaffolds were loaded together with 7.5 x 10^5 cells corresponding to an initial ratio of 30 cell/microscaffold for each cell line (NF, CAF or MCF7). To help cell seeding on microscaffold an intermittent stirring regime (30 min at 0 rpm, 5 min at 30 rpm) for 6 h has been performed. Then, dynamic cultures were kept under continuous stirring at 30 rpm for up to 12 days. Medium was changed on the first day and every 3 days until the end of the experiments. Ascorbic acid (final concentration 50 μg ml$-$1) was added to each spinner culture from day 2.

3.2.3 Tumor-on-chip culture

Device preparation

Before using, the device was sterilized by dipping into pure ethanol and after into PBS (supplemented with 2% of penicillin/streptomycin) in order to remove residual ethanol. The device was placed under UV light for 30 min. Tygon tubes (CM Scientific, UK, ID 1/16") were inserted into the inlets and outles of the lateral channels using an interface of male luer lock connectors

attached to barbed female luer lock connectors (Harvard Apparatus). Tubes and connectors were sterilized previously in autoclave. The flow assembly was set up using 1 and 3 ways stopcocks (Harward Apparatus). The stopcocks were sterilized in ethanol and washed in PBS. Before 3D-μTP loading, a 5 ml syringe filled with medium was connected to the inlet stream of one side channel in order to fill the channels with medium.

3D-μTP loading

The 3D-μTP suspensions were injected in the corresponding chamber using a simple pipette-driven loading process. We prepared three different device configurations:

- NF-μTP, obtained by loading NF-μTP in the stroma chamber and kept from T_0 (0 h) to T_2 (48 h);
- CAF-μTP, obtained by loading CAF-μTP in the stroma chamber and kept from T_0 (0 h) to T_2 (48 h);
- Activated-NF-μTP (AC-μTP), obtained by loading NF-μTP at time T_0 (0 h) and then loading MCF7-μTP at T_1 (24 h) and kept up to T_2 (48 h).

All the experiments were repeated in triplicate. Once the chamber was filled, the inlet and outlet of the chambers were closed with a 250 μm PDMS membrane (realized with spin coater 500 rpm for 30 s), a gate for medium outflow was opened in the opposite direction and the syringe pump was started (Harward Apparatus). A nominal flow rate of 3.0 μl min^{-1} producing an average linear velocity similar to that of blood in tumors was performed 2. The device was placed inside a 37 °C incubator with 5%CO_2 and 95% relative humidity for 48 h. The microfluidic device was observed daily by an inverted optical microscope.

3.2.4 *In situ* and on line tissue imaging

Immunofluorescence staining, imaging and quantification

α-sma, PDGFRβ-r, MMPs, Fibronectin and Hyaluronic Acid Imaging

Immunofluorescence assays were performed directly in the microfluidic device to detect α-SMA, PDGFβ-r MMP-9, MMP-2, fibronectin and hyaluronic acid in the stromal chamber of microdevice. To perform the immunofluorescence assay, at the end of the experiment (T_2, 48 h) a washing solution of PBS was flew in the devices for 50 min (5 μl min$_{-1}$); then 4% Paraformaldehyde was flew for fixing for 20 min, and then in PBS washing solution for 50 min. Subsequently the permeabilizing solution (0.2% Triton X-100 + 3% BSA + PBS) was injected with syringe pump for 50 min and blocked for 2 h. Then primary antibody (fibronectin 1:400, hyaluronic acid 1:50, MMP-9 1:200, MMP-2 1:100, α-SMA 1:250 and PDGFβ-r 1:200, Abcam) was introduced in the device. After overnight incubation, it was introduced in sequence PBS for 50 min, 0.2% Triton X-100 + PBS for 50 min, secondary antibody (Alexafluor) for 90 minutes. Finally a slow flow of PBS for 1 h was used to wash the tissues in the device.

α-sma, PDGFRβ-r, MMPs, Fibronectin and Hyaluronic Acid quantification

The amount of MMPs, Fibronectin and Hyaluronic Acid in the new formed ECM, was obtained processing the corresponding fluorescent images. After threshold in ImageJ, it was quantified the fraction of fluorescence signal in different regions of interest (ROI). In the same ROI, it was evaluated total cells number by counting their nuclei. Finally, it was evaluated the fraction of signal *per* cell [114].

On-line imaging and quantification

Collagen network imaging

Two-photon excited fluorescence (Leica TCS SP5 II coupled with a Multiphoton Microscope Chamaleon Compact OPO-Vis, Coherent) has been used to induce Second Harmonic Generation (SHG) and obtain high-resolution images of unstained collagen structures in the ECM of NF- and CAF-μTP (λex = 840 nm and λem = 420 $\pm$ 5). Images of 1024 x 1024 pixels and eight SHG z-stacks (10-15 μm step size) were acquired along the length of the stroma chamber under identical conditions (objective 25X/0.95 NA water immersion) and laser power (90 mW). The SHG stacks were then z-projected using a maximum intensity approach. The acquisition were performed as follow:

- NF-μTP and CAF-μTP were imaged at T_0 (4 h after loading), T_1 (24 h after loading) and T_2 (48 h after loading);
- AC-μTP, were imaged at T_0 (4 h after NF-μTP loading), T_1 (4h after MCF7-μTP loading) and T_2 (48 h after T_0).

Collagen network quantification

In order to quantify the collagen fraction in the endogenous ECM of the stromal tissues, SHG images were analyzed by using ImageJ software. Selected ROI were chosen by excluding the signal rising from the microscaffold. The collagenous portion in the ECM space was represented by the bright pixels (N_c) in grayscale originating from the SHG signal, while the non-collagenous portion appeared as black pixels (N_b). We define the collagen fraction (CF) the ratio between bright pixels to total pixels in the selected ROI, as reported in Eq. 3.1:

$$CF = \frac{N_c}{N_c + N_b} \tag{3.1}$$

where N_c and N_b represent the number of pixels from the collagen and non collagen portion, respectively. Moreover, to quantitatively assess the col-

lagen related changes, we perform Gray-level Co-occurrence Matrix (GLCM) texture analysis, using the ImageJ plug-in "Texture" on SHG images [104]. The GLCM was formed by counting the number of occurrences of a gray level adjacent to another gray level, at a specified pixel distance and direction. In particular, we calculated the correlation feature (Cor), a measure of intensity correlation as a function of pixel distance. The correlation was calculated for distances ranging from 1 to 16 μm in the horizontal (0°) and vertical (90°) direction. The Eq. 3.2 of Cor is given as below [63]:

$$Corr = \sum_{i,j} \frac{(i-\mu_i)(j-\mu_j)p(i,j)}{\sigma_i \sigma_j} \tag{3.2}$$

where μ_i, μ_j, σ_i and σ_j are given by:

$$\mu_i = \sum_{i,j} ip(i,j) \tag{3.3}$$

$$\mu_j = \sum_{i,j} jp(i,j) \tag{3.4}$$

$$\sigma_i = \sqrt{\sum_{i,j} (1-\mu_i)^2 p(i,j)} \tag{3.5}$$

$$\sigma_j = \sqrt{\sum_{i,j} (1-\mu_j)^2 p(i,j)} \tag{3.6}$$

In particular p(i,j) is the probability of gray level i occurring next to gray level j, μ_i, μ_j, σ_i and σ_j are the means μ and standard deviations σ of column i and line j of the matrix, respectively [103]. All parameters have a maximum value of 1 and a minimum value of 0 or -1 [103]. The Cor curve is an index of the architecture of the network, with a fast decay for fine textures and slow decay for coarse structure. From the Cor curve it is possible to obtain the correlation length λ, defined as the distance at which the Cor decay is equal to 0.5. Lower is λ finer is the texture. At last we analyzed SHG images to calculate the Collagen Assembly Degree (CAD) of collagen network [115]. To this purpose, all SHG images were subjected to noise subtraction and the

average intensity in the two different zones was evaluated as described by the Eq. 3.7:

$$CAD = \frac{\sum_{i=1}^{255} I_i p_i}{\sum_{i=1}^{255} p_i} \tag{3.7}$$

where I the average intensity, I_i is the intensity corresponding to the pixel p_i, while the index $i = x_i y_i$ runs in the gray value interval from 1 to 255. The intensity I of collagen network is known to be proportional to the degree of assembly of the newly synthesized collagen [115], [116], [110].

3.2.5 On-line measurement of the transport properties

The transport properties of the neo-formed tissues were measured in the devices, by means of real time application of Fluorescence Recovery After Photobleaching (FRAP) technique [117]. 3 kDa FITC-Dextran solution (5 μg ml^{-1} in Dulbecco's Modified Eagle Medium with high glucose, containing 2% fetal bovine serum, 100 μg ml^{-1} L-glutamine, 100 U ml^{-1} penicillin / streptomycin) was overnight flew in the devices at 3 μl min^{-1} and 37°C before the experiments. Prior to perform the FRAP experiments, ROI containing neo-formed collagen were detected by using SHG signal. Then, the FRAP measurements were conducted with a laser scanning microscope (TCS SP5, Leica). Samples were illuminated with a 25X (NA 0.95) objective and 488 nm excitation line from Argon laser operating with 5% output power. The bleaching time was 5.16s and the total ROI fluorescence images after photobleaching were collected at intervals of 0.263s at 512 x 512 pixel resolution using a pinhole of 600 μm, zoom factor 2.5 (with a zoom-in during bleaching) and 1000 Hz. Briefly, the mean fluorescence in the bleached region over time was converted to normalized fractional fluorescence intensity [118] (Eq. 3.8

$$f = \frac{F_t - F_0}{F_\infty - F_0} \tag{3.8}$$

where F_t is the fluorescence intensity at time t, F_0 is the fluorescence intensity immediately after bleaching, and F_∞ is the fluorescence after com-

plete recovery. The normalized fractional fluorescence intensity was plotted versus time and fitted with an exponential curve. The equation of curve was used to determine the half-recovery time (τ) at $f = 0.5$. Finally, the diffusion coefficient can be calculated as follow (Eq. 3.9:

$$D = \frac{\omega^2}{4t} \tag{3.9}$$

where ω is the initial spot radius.

3.2.6 Statistical analysis

The differences between two or more groups were evaluated (p_{value} ¡ 0.05) using one-way analysis of variance (ANOVA). A Gaussian distribution for each population was assumed. For pair-wise comparisons within each experimental group, Tukey's post test was used.

3.3 Results and Discussions

3.3.1 Breast cancer microenvironment on chip

In this work, an optically accessible microfluidic device was designed for the real time monitoring of the phenotypic, morphological and transport changes occurring in the healthy stroma (NF-μTP) activated by the interaction with epithelial breast tumor microtissues (MCF7-μTP). To replicate the tumor microenvironment the device was conceived in order to guarantee both compartmentalization and interaction between stromal and tumoral tissue allowing the imaging of distinct regions (Fig. 3.1). The geometrical configuration has been chosen to better recapitulate the *in vivo* pathophysiological conditions, where cancer cells are confined to the ductal system of the breast surrounded by stromal cells [107]. Cells *in vivo* are physically organized in 3D patterns surrounded by other cells as well as ECM that provide physical support and signaling molecule. The co-culture carried out in the microfluidic device presents the prominent advantage to recreate the dynamic

tumor-stroma cross talk, crucial in tumor development. For each experiment three microfluidic devices were performed in parallel: two microdevices were loaded with stromal-tissue, NF-μTP (Fig. 3.2 A) and CAF-μTP (Fig. 3.2 B) respectively; the third device was used for co-culturing NF-μTP and MCF7-μTP (Fig. 3.2 C).

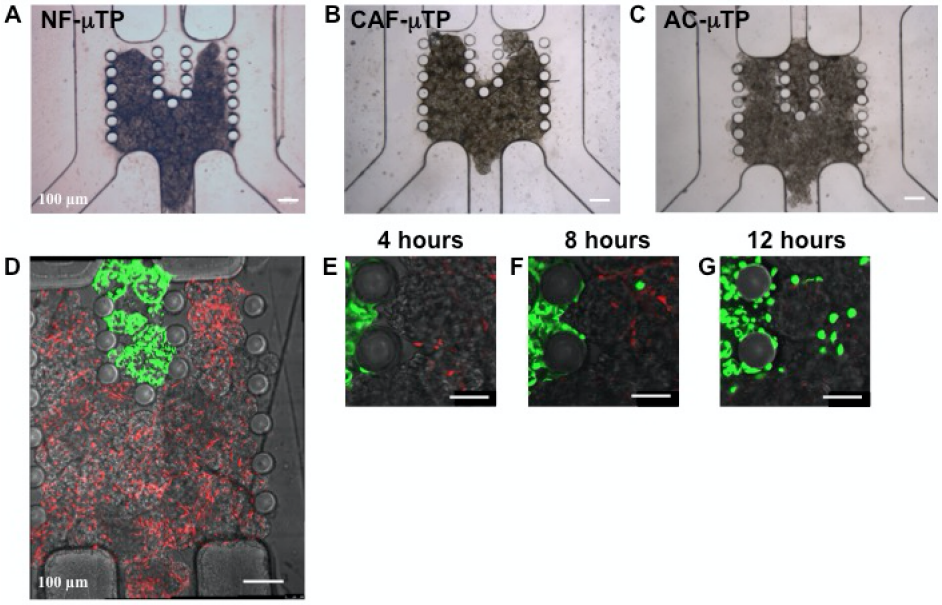

Figure 3.2: Bright field images of the stromal and tumor chambers containing NF-μTP (A), CAF-μTP (B) and AC-μTP (obtained by loading NF-μTP at time T_0 and then loading MCF7-μTP at T_1) after 48 h of loading (T_2). D: fluorescence images of NF-μTP (in red) and MCF7-μTP (in green). Time-lapse images of MCF7 and NF-μTP after 4 (E), 8 (F), 12 (G) h of MCF7-μTP loading. Scale bar = 100 μm.

In Fig. 3.2 A-C, the bright field images of all loaded microdevices at T_2 were reported, showing the μTP well packed in the dedicated chambers. In the microdevice dedicated to co-culture, NF-μTP and MCF7-μTP were in contact along the array of pillar separating tumor and stromal chamber. Since the NF and MCF7 were clearly distinguishable due to their intrinsic fluorescence (Fig. 3.2 D), it is possible to observe in real time invasion of

tumor cells towards the adjacent chamber (Fig 3.2 E). Just after 8 hours it is possible to observe single tumor cells that left the MCF7-μTP to migrate towards the stromal chamber where NF-μTP were accommodated (Fig 3.2 F), after 12 hours the numbers of tumor cells invading the stromal chamber increased (Fig. 3.2 G). These results are in agreement with previous works demonstrating that fibroblasts arranged in a 3D configuration induced the invasive behavior of tumor cells. This was due also to the increase of paracrine-signaling molecules occurring in 3D compared to 2D cultures [119]. In our experiments a syringe pump controlled the flow rate in the microfluidic device and the entire setup could be readily accommodated on the microscope stage in a climate-controlled incubator. By using such configuration, nutrients and eventual therapeutics can easily reach the cells of 3D-μTP via continuous perfusion of the medium and, at the same time, metabolic wastes can be removed. Recently, several studies have combined microfluidic techniques with 3D tumor models, like spheroids, to better recapitulate tumor microenvironment found *in vivo*. However, spheroids only partially recapitulate the tumor complexity seen *in vivo* because due to the lack of a controlled microarchitecture and a significant presence of ECM components. As previously described [51], [113], the 3D-μTP model used in this work, can represent a more realistic tool to recapitulate the ECM dynamic *in vitro*. Indeed in such configuration the fibroblasts are engaged in the ECM turnover: assembly and disassembly of collagen, elastin and hyaluronic acid [113]. The presence of such condition in the tumor stroma is crucial in the in the effort of mimicking the behavior of some tumor types featured by a dense desmoplastic stromal reaction like breast adenocarcinoma [120]. For these reasons, the integration of the engineered 3D-μTP within the microfluidic device will offer a novel tool to investigate cancer progression at both cellular and ECM level.

3.3.2 MCF7-μTP induces NF-μTP activation at cellular and ECM level

Phenotypic activation and MMPs over-expression in activated tissues

Firstly, we investigated if a period of 24 h of co-culture of MCF7-μTP and NF-μTP in the microfluidic device could activate the NF and turn them into myofibroblasts. It is well known that one of the major marker proteins to identify myofibroblasts is α-SMA [121]. In addition, there are several observations suggesting that the presence of PDGF receptors in stromal cells is an important indicator of the desmoplastic reaction in tumors [122].

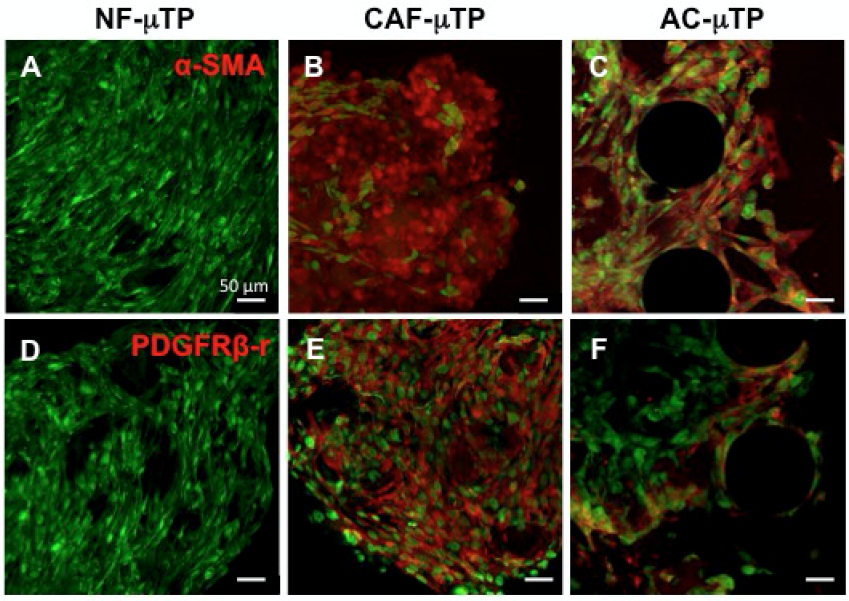

Figure 3.3: α-sma and PDGFβ-r fluorescence images (red signal) in NF-μTP (A, D), CAF-μTP (B, E) and AC-μTP (C, F). Green fluorescence is related to cells. Scale bar = 50 μm.

For this reason, the over-expression of PDGF receptors in breast tumors is recently correlated with tumor progression and invasion becoming a novel drug target [123]. As consequence, in addition to α-SMA we identified PDGF

receptors as markers of NF activation and we performed immunofluorescence analyses to reveal their presence directly in the microfluidic devices. The results of immunofluorescences at T_2 are reported in Fig. 3.3 and showed that as expected, CAF-μTP (Fig. 3.3 B and E) were positive for both α-SMA and PDGFβ-r (red signal in pictures) while at the same time point NF-μTP did not express the proteins (Fig. 3.3 A and D). In contrast, in co-culture conditions immunofluorescences reveal the presence of both the proteins in the NF-μTP, suggesting that the co-culture with MCF7-μTP induced the activation of NF into myofibroblasts generating the AC-μTP. These data are in agreement with previous works that have demonstrated the activation of normal fibroblasts into myofibroblasts after their physical contact with cancer cells in a microfluidic device [124].

In addition we further investigated the expression of MMPs (Fig. 3.4), enzymes responsible for matrix degradation that have been shown to play a significant role in tumor progression [125], [126]. Indeed, the ability of cancer cells to migrate through 3D environments likely depends on their possibility to stimulate fibroblasts in the production of MMPs in a paracrine fashion. The over-expression of MMPs in the tumor microenvironment is often associated with adjacent normal tissues rather than the tumor cells themselves, suggesting that neoplastic cells can use MMPs produced by normal cells to facilitate their invasion and progression [127]. Among MMP family, MMP-9 and MMP-2 are known to play an important role in the context of tumorigenesis and metastasis, especially in breast tumor, because they degrade collagen IV and weaken the basement membrane. Degradation products of ECM, including fragments of collagen IV, can act as signaling substances regulating tumor cell motility [128]. We found an over-expression of MMP-9 and MMP-2 in CAF-μTP (Fig. 3.4 B and E) compared to NF-μTP (Fig. 3.4 A and D), while AC-μTP (Fig. 3.4 C and F) showed an over-expression of MMP-9 (Fig. 3.4 G) but not of MMP-2 (Fig. 3.4 H). Previous works reported that depending on the culture-system, co-culturing tumor-derived or normal fibroblasts with breast cancer cells should result in an increased expression of

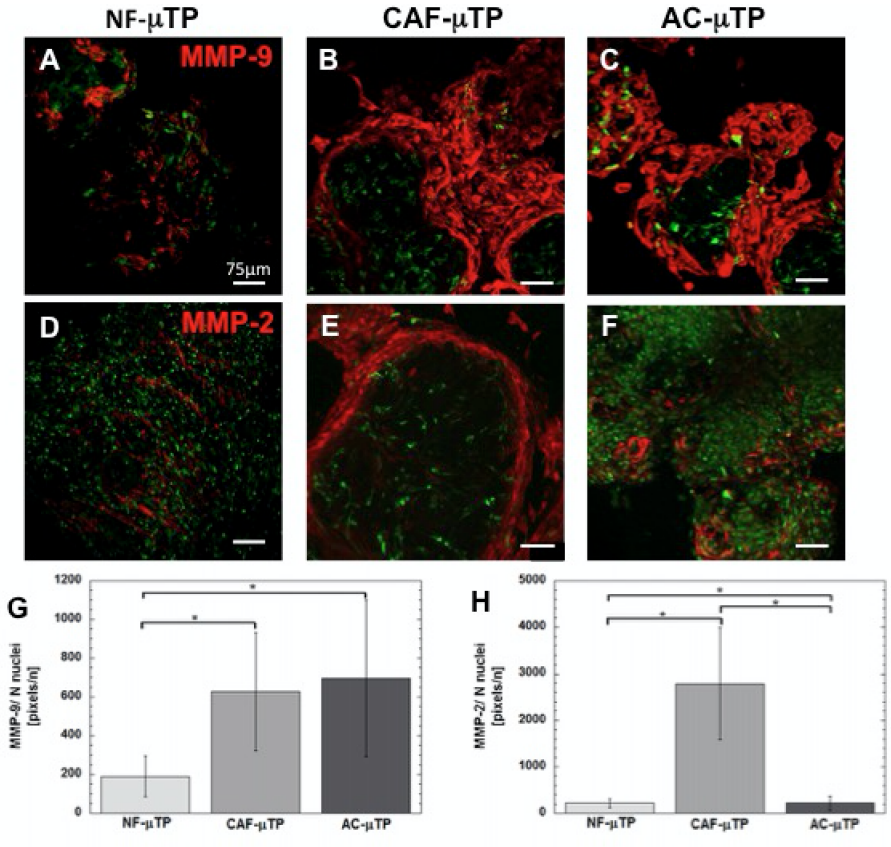

Figure 3.4: MMP-9 and MMP-2 fluorescence images (red signal) in NF-μTP (A, D), CAF-μTP (B, E) and AC-μTP (C, F). Green fluorescence is related to cells. Scale bar = 75 μm. Quantification of MMP-9 (G) and MMP-2 (H) expression (pixels / nuclei) in NF-μTP (light gray), CAF-μTP (middle gray) and AC-μTP (dark gray). Whiskers and asterisks indicate statistical difference with $p < 0.05$.

MMP-2 by either partner [128]. In particular, the co-culture of the breast cancer cells and fibroblasts resulted in an increase of MMP-2 in culture supernatants in a manner that was largely, although not entirely, dependent on direct contact between the two cells types [129], [130], [131], [132]. However, this process has only been demonstrated when the co-culture was carried for more than 2 days [129]. In our case, the compartmentalization created by pillars between the stroma and cancer chambers in the microfluidic device

allows the physical contact among the cells but the time of contact (24 h) is probably not enough to induce MMP-2 over-expression in the AC-μTP. Regarding MMP-9 expression, our data are in accordance with previous findings *in vitro* showing the increased production of MMP-9 in the co-cultivation of fibroblasts and breast cancer cells after 24 hours of cell contact in a Boyden chamber [133]. In conclusion these results suggest that although MMP-2 and MMP-9 are both gelatinase, the time needed to record their overexpression in stromal cells in contact with tumor cells is different. This aspect can seem controversial but can be explained by the fact that their trigger mechanism is probably different [132].

3.3.3 ECM components over-expression in activated tissue

To better understand the dynamic nature of the 3D microenvironment surrounding cells, it is mandatory to have a tissue model in which the cells are embedded in a 3D matrix. As ECM surrogates, collagen and other biopolymers partially recapitulate the whole tissue dynamics. Indeed, we have demonstrated that the mechanism of tissue remodeling in terms of synthesis, assembly and degradation of the ECM are depressed in cell-populated collagen gels [104]. Only engineered tissues composed by cells embedded in their own ECM are able to replicate *in vitro* the pathophysiological process occurring *in vivo* at extracellular level. This condition allows to monitor and to quantify the active modification of the ECM composition and organization due to the progression of pathologic status [44], [104]. To this end, we investigated the evolution of the keys ECM components involved in the tumor process, such as fibronectin, hyaluronic acid (HA) and collagen (Fig. 3.5).

It is well known that the abnormal structure and function of tumor stroma is largely attributed to the up-regulation and re-organization of matrix remodeling molecules [126]. For example, a significant number of studies show that HA and fibronectin deposition increase in various types of cancer tissues including breast cancer, and the rate of HA synthesis is much higher in

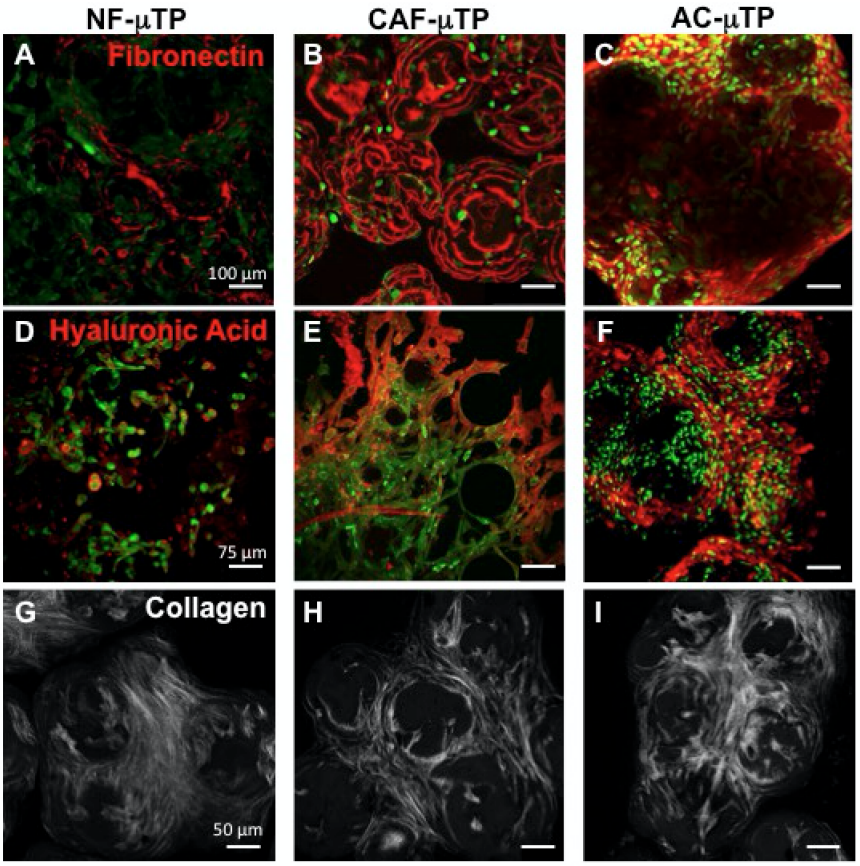

Figure 3.5: Fibronectin fluorescence images (red signal) in NF-μTP (A), CAF-μTP (B) and AC-μTP (C). Scale bar = 100 μm. Hyaluronic Acid fluorescence images (red signal) in NF-μTP (D), CAF-μTP (E) and AC-μTP (F). Scale bar = 75 μm. SHG signal (gray scale) from newly formed fibrillar collagen in NF-μTP (G), CAF-μTP (H) and AC-μTP (I). Scale bar = 50 μm.

cancers than in normal tissues [16]. Unlike studies in which the presence of fibronectin and HA were detected at molecular level [16], [134], in our model fibronectin and HA were correctly assembled and deposited in the extracellular space and then detectable by immunotypization (Fig. 3.5 A-F in red). Furthermore, neo-formed collagen due to its capability to self-assemble in fibrils and fibers could be detected by on-line SHG signal (Fig. 3.5 G-I in

gray scale). SHG signal can be used to get information concerning both the collagen composition as well as its structural modification due to the transition of fibroblasts from healthy to activated state [125]. In Fig. 3.6 A-C are reported the quantification of the ECM components: fibronectin (Fig. 3.6 A), HA (Fig. 3.6 B) and collagen (Fig. 3.6 C) in NF-, CAF- and AC-μTP.

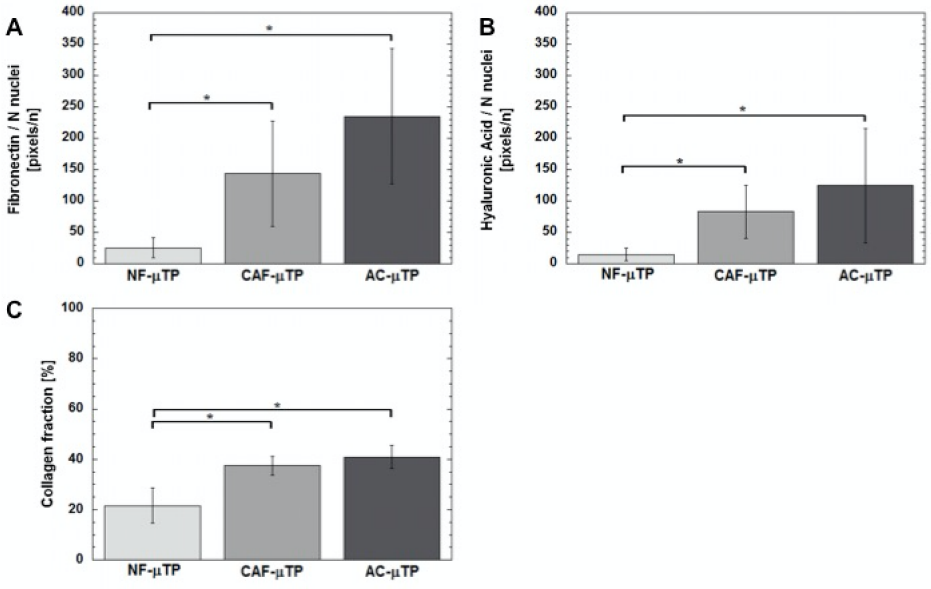

Figure 3.6: Quantification of Fibronectin (A) and Hyaluronic Acid (B) expression (pixels / nuclei) and collagen fraction (C) in NF-μTP (light gray), CAF-μTP (middle gray) and AC-μTP (dark gray). Whiskers and asterisks indicate statistical difference with $p < 0.05$.

Fibronectin and HA were present in higher amount in the CAF- and AC-μTP than in NF-μTP. This suggests a role of the MCF7-μTP in activating pathological events at ECM level in the NF-μTP. It is interesting to point out that we found alterations in the ECM composition just after 24 h of contact between NF-μTP and MCF7-μTP in the microfluidic device. This indicates that the conditions recreated in our microdevice, induced both physical contact and biological cross talk between NF-μTP (healthy zone), and MCF7-μTP (tumor zone). Such ECM-mediated cross talk im-

plied the ECM reorganization resembling its *in vivo* pathologic evolution. In our model the deposition and the up-regulation of HA at extracellular space are not trivial phenomena due to their relevance in the aggressiveness of cancers. Indeed, cell proliferation, invasion, metastasis and tumor-stroma interactions, are mediated by HA level and distribution [16]. Furthermore, HA levels increased with tumor progression from ductal carcinoma *in situ* to later stage invasive carcinoma [135]. Such results on collagenous and non-collagenous over-expression of ECM macromolecules give further support that α-SMA and PDGFβ-r positive fibroblasts in the stroma tissue promote tumor progression [19]. The remodeling of ECM is also correlated with the up-regulation of MMP-9. Taken together these results indicate that the microfluidic system reflects some relevant heterologous interactive processes characterizing the tumor microenvironment.

3.3.4 Time evolution of endogenous collagen network architecture

A cutting edge strategy used *in vivo* to study cancer evolution in a non-destructive manner, is represented by the real time acquisition of the ECM components by means of multiphoton imaging [63]. How collagen architecture changes during pathologic status is currently used as a clinical biomarker for tumor diagnosis and staging [59]. For example, SHG and Third Harmonic Generation (THG) imaging have been used to monitor tumor progression and carcinogenesis. Information about the interactions between tumor cells, extracellular matrix and epithelial-stromal communication, as well as the initiation of collagen remodeling, can be obtained [66]. It is well known that collagen organization is altered in tumor tissue in comparison to normal one. We implemented real time SHG imaging in the microfluidic device to monitor the collagen organization during the activation period (from T_1 to T_2) of NF-μTP in AC-μTP. In particular, we used two methods to obtain information about time evolution of structure, organization and architecture of collagen fibers: GLCM [136] and CAD [115], [113]. In particular, by using

GLCM we evaluated the correlation (*Cor*) in order to detect the transition of the collagen network from a fine to a wavy, crimped or coarse architecture [137]. The CAD index, instead, gives information about the degree of assembly of the collagen network [115], [113]. In Fig. 3.7 the behavior of *Cor* (Fig. 3.7 A-D) and CAD (Fig. 3.7 E) is reported for NF-μTP, CAF-μTP and AC-μTP.

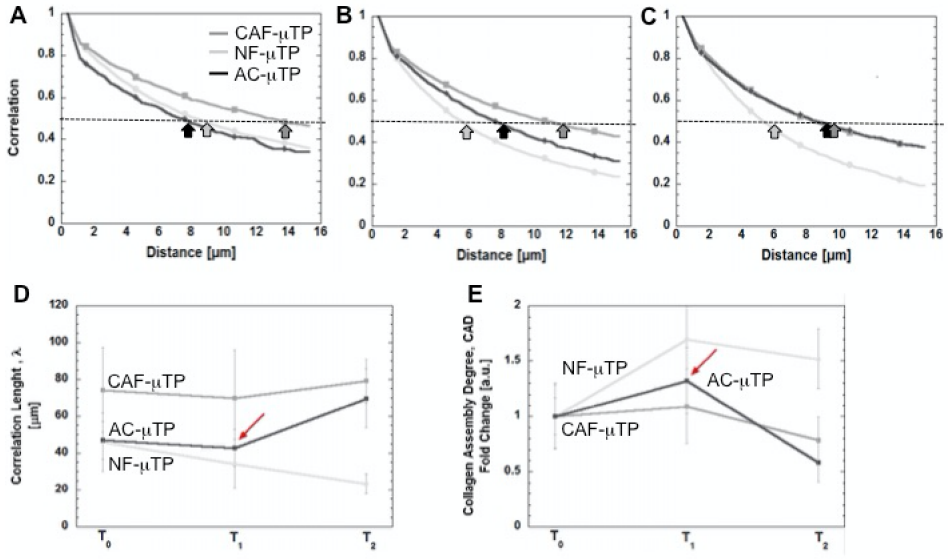

Figure 3.7: Correlation curve as a function of distance in μm in NF-μTP (light gray), CAF-μTP (middle gray) and AC-μTP (dark gray) at time T_0 (0 h, A), T_1 (24 h, B) and T_2 (48 h, C). Correlation length - λ - obtained by fitting parameters from normalized correlation curves (D) and fold change of collagen assembly degree - CAD - in NF-μTP (light gray), CAF-μTP (middle gray) and AC-μTP (dark gray) during culture time (from T_0 to T_2). Statistical difference was determined using ANOVA test ($p < 0.05$).

At time T_0 (Fig. 3.7 A) the correlation curve of both healthy tissues NF-μTP and AC-μTP ($T < T_1$), decayed faster than CAF-μTP one. This indicates that the collagen assembled by normal fibroblasts had a finer structure than that of CAF-μTP [137]. As time increased to T_1 (Fig. 3.7 B) the correlation curves of the NF-μTP continued to decay faster than those

of the CAF-μTP. On the contrary the AC-μTP correlation curve started to tend toward the CAF-μTP curve. At the end of the culture time (T_2, Fig. 3.7 C), we found that the NF-μTP curve still decreased faster than *Cor* of CAF-μTP. Interestingly, the AC-μTP curve completely overlapped the CAF-μTP curve. The phenomenon of collagen remodeling can be better pointed out by plotting the value of λ versus culture time. In Fig. 3.7 D the λ values of the NF-μTP decreased as culture time increased. This represents the healthy evolution of the tissue: as collagen is synthesized, it is remodeled by fibroblasts in an even finer structure. On the contrary the λ of the CAF-μTP remained constant over culture time and its value was always higher than NF-μTP. This dissimilar trend is a function of the different ECM remodeling mechanisms of the cells; indeed, depending on tumor type and stage, fibroblasts assemble the collagen network that is featured by a coarser structure compared with healthy collagen. The λ of AC-μTP started to decrease as in the case of NF-μTP from T_0 to T_1. After T_1 (activation time), the λ of AC-μTP showed an opposite trend and started to increase reaching a final value close to the value of CAF-μTP. Finally this reflects the fact that there is a link between epithelial carcinogenesis process and progressive loss in the fine fibril structure. These results are in accordance with previous works in which the correlation was applied to human epithelial tumors [137], [64], [138], [65] and in particular to adenocarcinoma tumors [66], [136], as in our case. Indeed those studies have demonstrated that collagen fibers are irregularly distributed without well-defined orientation in pathological samples, while the morphology of the collagen fibers were highly arranged in normal samples. This technique is very useful because it allows discriminating between cancerous and healthy tissue, with clear distinctions between normal, benign, borderline and malignant tumors. Obviously, the possibility to use such a technique *in vitro* is strongly correlated with the opportunity to produce a living tissue model evolving during culture time at cellular and extra cellular level. Further investigations on collagen were performed by CAD analysis (Fig. 3.7 E). In the case of NF-μTP (Fig. 3.7

E), the CAD increased over culture time, indicating that collagen was continuously assembled in the stromal chamber. On the contrary, the CAD in CAF-μTP, remained constant and lower than the NF-μTP for all three time investigated. This coarsening suggested the presence of less defined fibril organization compatible with higher value of λ. Finally, the CAD of AC-μTP, increased in the first time interval (T_0-T_1) then started to decrease after the activation time (T_1-T_2). Taken together such results demonstrated how AC-μTP moved from healthy to cancer status due to the presence of the MCF7. We want to point out that the variation of collagen network architecture is due to several phenomena occurring in the microdevice in the co-culture conditions such as the over-expression of MMPs and the phenotypic activation of NF into myofibroblasts. These conditions imply that the deposited collagen network become coarser and less assembled [64]. These results highlight that our system allows real time recording of the activation of normal stroma at cellular and extra cellular level very easy way, avoiding time consuming and destructive procedures.

3.3.5 Correlation between interstitial diffusivity and ECM evolution

Together with hydraulic conductivity ([139], [140], [141]), diffusivity represents one of the key factors affecting drug delivery in biological tissues. Their real time estimation should be of great interest to accurately design both macromolecule features and therapeutics. By combining multiphoton and FRAP [117] technique (Fig. 3.8 A) we performed real time measurements of FITC-Dextran diffusion coefficient in NF-, CAF- and AC-μTP (Fig. 3.8 B).

The possibility to detect SHG from collagen, allowed to perform FRAP experiments directly in the collagen space (Fig. 3.8 A). Our results show that the diffusion coefficient of FITC-Dextran was significantly higher in NF-μTP compared with CAF- and AC-μTP ($p < 0.05$, Fig. 3.8 B). This difference can be explained by taking into account the effect of ECM architecture and composition on transport properties in tissues [140]. Indeed,

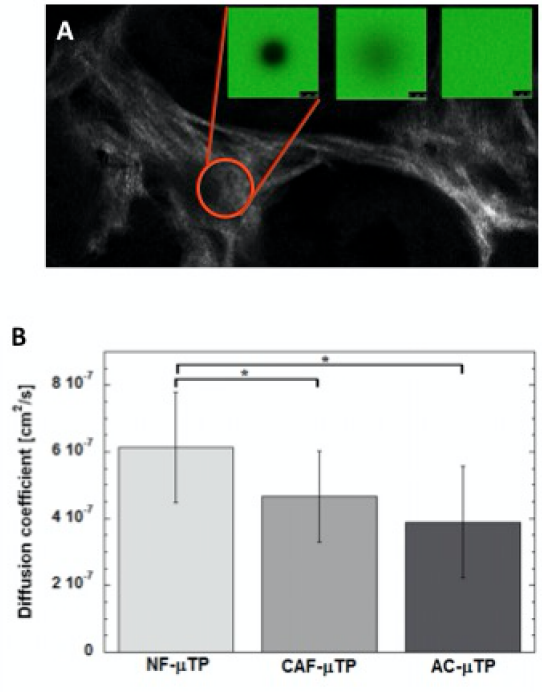

Figure 3.8: SHG and FRAP techniques to investigate transport properties in μTP. The ROI (40 μm) was chosen in the collagen space (A). Diffusion coefficients (B) of FITC-Dextran (3 kDa) in NF-μTP (light gray), CAF-μTP (middle gray) and AC-μTP (dark gray). Statistical difference was determined using ANOVA test ($p < 0.05$).

both non-collagenous components and collagen accumulation in the interstitium depress the diffusion coefficient [142], [143], [144], [145], [146], [147], [148]. On the contrary, the removal or reorganization of these fibers has been shown to improve interstitial transport [71]. The ECM composition and the resultant diffusion coefficient are influenced by tumor-host interactions suggesting that there may be differences between diffusion coefficients measured in tumors respect to normal tissues. Our findings suggest that the interstitial transport resistance is strictly related to the organization, architecture and composition of the ECM. Indeed when we move from the healthy stroma (NF-μTP) to pathologic stroma (CAF-μTP) we observed: (i) the increase of

HA, fibronectin and collagen fraction (Fig. 4.6); (ii) the transition from a fine to a coarse arrangement of the collagen network (Fig. 3.7). Such conditions induced both "interstitium crowding" and reduction of the ECM mesh size that ultimately lead to an increase of frictional interaction between dextran and ECM. Interestingly, the AC-μTP behaved as CAF-μTP in terms of diffusion coefficient (Fig. 3.8 B). This indicates that our system is able to detect the stromal activation also in terms of transport properties.

3.4 Conclusions

In this work a new microfluidic platform was presented as a tool for studying the impact of reciprocal interactions between fibroblasts and tumor cells through the integration of 3D engineered tissue model. The optical accessibility of the microdevice coupled with the high-fidelity features of our 3D tissue model allowed, for the first time, to monitor and to quantify in real time healthy / tumor transition *in vitro* at ECM level. Since to date such information can be obtained only by means of *in vivo* experiments [61], we argue that our system paves the way for a new class of drug screening platform that include, as design criterion, the interaction between therapeutics and tumor stroma. Moreover the versatility of our model could allow the incorporation of tumor vascular component by the introduction of endothelial cells in lateral channels or the perfusion of new therapeutic targets into lateral channels emulating the *in vivo* intravenous injections. On the basis of these observations we believe that our system (microdevice and 3D-μTP) can bridge the gap between current 3D tissue model and animal models reducing expensive and time-consuming protocol nowadays used in preclinical studies.

Chapter 4

Comparison of the behavior of tumor breast spheroids and microtissues in response to free-Doxorubicin treatment

4.1 Introduction

Traditionally, preclinical studies for anti-cancer drug testing are usually performed in two dimensional (2D) *in vitro* culture [149]. In 2D systems, cells are deprived of the extracellular matrix that is fundamental in regulating tumor progression [150]. As consequence of the lack in cell-matrix interactions, these simplified systems do not faithfully recapitulate the complexity of the tumor microenviroment *in vivo* and consequently drug response is controversial [118]. On the other hand, animal testing in clinical research should be limited since their use is time-consuming, also expensive and poor predictive of human response to drug [151].

The 3D cell culture approaches have dramatically improved our understanding of the role of tumor microenvironment incorporating the extracellular matrix (ECM), stromal cells and physical signals [150]. Spheroid is one

of the most studied and established cancer models since it recapitulates the architecture of the tumor core *in vivo*. Several studies have demonstrated the simplicity and high reproducibility of this model, making it suitable as a anti-cancer drug screening platform. However spheroids present some limitations since they are compact cell aggregates that do not interact with their extracellular milieu and do not have physical resistance provided by the ECM [152], [153], [154]. Concerning drug testing, it is already known that tumor ECM plays a key role in triggering mechanisms related to chemoresistance and act as barrier in drug diffusion. Although the ECM is important to regulate this feature, only few works reported the incorporation of stromal cells in spheroid models, underlining the limitation of these models [87]. By this way, there is an increasing need of a more relevant tumor model recapitulating various aspects of cancer including three-dimensional architecture, multiple cell types and an extracellular matrix barrier [87]. With the advance in tissue engineering, microcarriers based approach have been employed to guide cell development into 3D organization to better mimic the native tissue, providing a more reliable tool for drug testing. Unlike what happens in cellular spheroids, in the case of cell-seeded microcarriers, the cells are induced to grow on the microcarrier surface and under controlled culture condition are able to synthesize endogenous ECM. The microcarriers based approach can lead to a more realistic tumor tissue model for *in vitro* applications such as drug screening.

In the present study, we developed an *in vitro* 3D breast cancer microtissue and spheroid model using MCF-7 cell line in monoculture and coculture with cancer-associated fibroblasts (CAF). The 3D microtissue model is obtained by seeding tumor and/or fibroblast cells on porous biodegradable microcarriers in a dynamic culture system according to previous works [6], [51]. Anticancer effects of Doxorubicin (DOX), one of the most widely used chemotherapeutic agent [155], were studied and IC_{50} values were compared between microtissues and spheroids 3D culture model. Moreover drug diffusion in the different model was studied by means of FRAP method. Finally,

we found that breast cancer cells in the 3D model present a different behavior in terms of chemoresistance when they are cultivated in different 3D models in monoculture and coculture. Moreover when they are in coculture with CAF, they resembled some features of xenograft tumor model, bring near this model to the *in vivo* condition. Therefore, tumor microtissues could be valuable candidates for drug screening assay.

4.2 Materials and Methods

4.2.1 Cell type

Human breast adenocarcinoma cells (MCF7) and cancer associated fibroblasts (CAF), (kindly donated by Daidone and Kojima's group, respectively) were sub-cultured onto 150 mm Petri dishes in RPMI-1640 (Roswell Park Memorial Institute) and Dulbecco's Modified Eagle Medium respectively, with high glucose, containing 10% fetal bovine serum, 100 μg/ml L-glutamine, 100 U/ml penicillin/ streptomycin. Cells were maintained at 37°C in humidified atmosphere containing 5% CO_2. CAF were stable transfected with pLVX-DsRed-express2-N1 (Î»ex 554nm, λem 591nm) viral vector (Clontech, USA).

4.2.2 Microbeads production

Gelatin porous microbeads (GPMs) have been prepared by following a previously established protocol [6]. GPMs have been stabilized by crosslink reaction with GPMs glyceraldehydes (GAL), in order to make them stable in aqueous environment at 37 °C, as previously described [6]. GAL at 5% w/w of the microbeads has been used to perform all the experiments.

4.2.3 Dynamic cell seeding

Before using, dry GPM were sterilized in absolute ethanol 24 h on a rotating plate. Then, GPMs were washed twice in sterile phosphate-buffered saline

(PBS) without calcium and magnesium solution. Finally, before cell seeding, PBS was replaced by fresh culture medium. For homotypic culture (MCF7 alone) 50mg of GPMs were loaded together with $7.5*10^5$ cells (30 cell/GMP ratio). To help cell seeding on GMPs an intermittent stirring regime (30 min at 0 rpm, 5 min at 30 rpm) for 6 h has been performed. Then, dynamic cultures were kept under continuous stirring at 30 rpm for up to 12 days. For heterotypic culture (CAF/MCF7-μTP) at day 6th, MCF7 cells were added in a ratio 1:3 to CAF cells into spinner flask. Medium was changed on the first day and every 3 days until the end of the experiments. For fibroblasts, from the day 2nd, 50 μg/ml of ascorbic acid were added.

4.2.4 Homotypic and heterotypic spheroid formation

MCF-7 cells were trypsin-treated and counted. Subsequently, they were seeded onto round bottom non-tissue culture treated 96 well-plates (Falcon, BD NJ, USA) at a concentration of 2500 cell/well in RPMI 10% FCS supplemented with 20% methylcellulose stock solution. For cocultured spheroids we used a total of 2500 cell/well, where CAF were seeded in a ratio 3:1 with MCF7 cells. For preparation of methylcellulose stock solution we autoclaved 3 grams of methylcellulose powder (M0512, Sigma-Aldrich) in a 250 ml bottle containing a magnetic stirrer. The autoclaved methylcellulose was dissolved in preheated 125 ml basal medium (60°C) for 20 min (using the magnetic stirrer). Thereafter, 125 ml medium (RT) containing double amount of FCS (20%) was added to a final volume of 250 ml and the whole solution mixed overnight at 4°C. The final stock solution was aliquoted and cleared by centrifugation (5000 g, 2 h, RT). Only the clear highly viscous supernatant was used for the spheroid assay (about 90-95% of the stock solution). For spheroid generation was used 0.24% methylcellulose. Spheroids were grown under standard culture conditions (5% CO_2, at 37°C) and harvested at different time points for further investigations.

4.2.5 Drug treatment and cytotoxicity

About 10 μL of MCF7-μTP solution and one CAF/MCF7-μTP were transferred into well of a round bottom 96 well plates in order to have the same cell density. Both spheroids and μTP were treated with free doxorubicin (Sigma) at 4, 8 and 16 μg/ml after dilution from a stock solution (40 μg/ml). One row of 96-wells plate was used as control with 200 μL culture medium only. After incubation for 48 and 72 h at 37°C in humidified atmosphere containing 5% CO_2, 20 μL of 3-(4,5-dimethylthiazol-2-yl)- 2,5-diphenyltetrazolium bromide (MTT) solution (5 mg/ml) was added to each well, and the plate was incubated for another 4 h, allowing the viable cells to reduce the yellow MTT into dark-blue formazan crystals, which were dissolved into 100 μL of dimethyl sulfoxide (DMSO). The absorbance of individual well was measured at 470 nm by a microplate reader (Enspire Multimode Plate Reader PerkinElmer). All experiments were done in triplicates.

4.2.6 Doxorubicin penetration imaging

μTP and spheroids treated with doxorubicin (DOX) were washed three times with PBS and fixed in 4% paraformaldehyde (PFA) in PBS for 20 min. Cell nuclei were stained with 1 μg/ml 4',6-diamidino-2-phenylindole (DAPI, Sigma-Aldrich). DOX fluorescence was observed under a confocal microscope (Leica) with excitation at 488 nm and with a 40X water objective (NA = 1.10). For drug penetration study, μTP and spheroids treated with 8 μg/ml of DOX were aquired with a magnification 3.5.

4.2.7 Doxorubicin penetration quantification

All the images were analyzed using ImageJ software. First, the images were converted to grey scale. An adaptive thresholding method was applied to separate the foreground from background. Multiple images were quantified and averaged. To determine drug penetration, we detected the boundary of the region of interest (ROI). Signal intensity per ROI was quantified as image

fluorescent intensity by a specific area in the image [152]. Pixels' fluorescence intensity of regions of interest were counted and normalized by the area.

4.2.8 Diffusion measurement by fluorescence recovery after photobleaching (FRAP)

Diffusion of DOX was measured with fluorescein isothiocyanate with similar molecular weight (389.38 g/mol, Sigma) by Fluorescence Recovery After Photobleaching (FRAP) technique. FRAP measurements were conducted with a laser scanning microscope (TCS SP5, Leica). Samples were illuminated with a 25X (NA = 0.95) objective and 488 nm excitation line from Argon laser operating with 5% output power. The bleaching time was 5.16 s and the total ROI fluorescence images after photobleaching were collected at intervals of 0.263 s at 512 x 512 pixel resolution using a pinhole of 600 μm, zoom factor 2.5 (with a zoom-in during bleaching) and 1000 Hz. Diffusion coefficients were calculated from FRAP experiments. Briefly, the mean fluorescence in the bleached region over time was converted to normalized fractional fluorescence intensity [118]:

$$f = \frac{F_t - F_0}{F_\infty - F_0} \tag{4.1}$$

where F_t is the fluorescence intensity at time t, F_0 is the fluorescence intensity immediately after bleaching, and F_∞ is the fluorescence after complete recovery. The normalized fractional fluorescence intensity was plotted versus time and fitted with an exponential curve. The equation of curve was used to determine the half-recovery time (τ) at $f = 0.5$. Finally, the diffusion coefficient can be calculated as follow:

$$D = \frac{\omega^2}{4t} \tag{4.2}$$

where ω is the initial spot radius (40 μm).

4.2.9 Immunofluorescence staining, imaging and quantification

For immunofluorescence staining, formalin-fixed and paraffin embedded μTP and spheroids were unmasked by heat antigen retrieval protocol by citrate buffer; washed with PBS containing 0.2% Triton X-100, blocked with FBS and 5% BSA solution and incubated with primary antibody (E-cadherin 1:250, Claudin-1 1:250, ZO-1 1:50). All the antibodies were purchased by Abcam (UK). Secondary antibody incubation and DAPI staining were performed, before closing the slices with glycerol solution. The same immunofluorescence staining was made in mouse xenograft model. The fluorescent images, previously acquired by using a multichanneled Leica TCS SP5 II, were analyzed for semi-quantitative evaluation with ImageJ. After threshold, the amount of signal was divided by the total number of cells (previously obtained by counting their nuclei) in each image [114].

4.2.10 Statistical analysis

Differences between two or more groups were evaluated ($p_{value} < 0.05$) using one-way analysis of variance (ANOVA). A Gaussian distribution for each population was assumed. For pair-wise comparisons within each experimental group, Tukey's post test was used.

4.3 Results

In this work two types of 3D cancer models were compared: spheroid and μTP in homotypic (MCF7) and heterotypic (CAF/MCF7) condition. DOX response was investigated in μTP models in terms of cytotoxicity, imaging, drug diffusion and penetration and compared to a classic model used in cancer research, the spheroid model.

4.3.1 *In vitro* imaging and cytotoxicity assay

Both homotypic and heterotypic spheroids and μTP were exposed to DOX for 48 and 72 h and then cell viability was assessed by MTT assay. From this colorimetric proliferation assay it is possible to know the number of viable cells by measuring the quantity of formazan produced at 470 nm. Fig. 4.1 shows the cell survival of MCF7 spheroids and μTP as a function of DOX concentration (4-8-16 μg/ml) for 48 (Fig. 4.1 A) and 72 h (Fig. 4.1 B). In both homotypic models, higher is the DOX concentration lower is the percent of cell proliferation. As we can see, it was necessary an incubation time of 72 h in order to have a reduction of 50% of cell population for both models. In particular, the IC_{50} (concentration for 50% cell death) of DOX for MCF7 spheroids and μTP was calculated to be 8 μg/ml and 4 μg/ml, respectively.

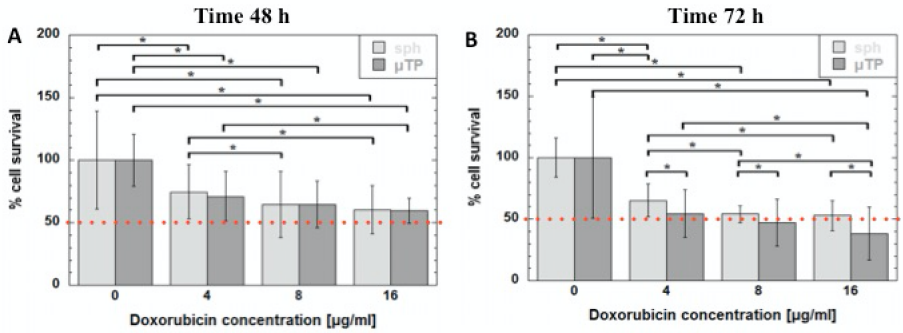

Figure 4.1: Cytotoxicity assay in MCF7 spheroids (light gray) and μTP (middle gray) after treatment with DOX at 4, 8 and 16 μg/ml for 48 (A) and 72 h (B).

In Fig. 4.2 we reported optical (Fig. 4.2 A-D and I-N) and fluorescence (Fig. 4.2 E-H and O-R) images of heterotypic spheroids and μTP after DOX treatment for 48 and 72 h. From spheroids brightfield images (Fig. 4.2 A-D), the effect of DOX is strictly limited to the outer cell layers (death cells detached from the spheroid configuration) but the spheroid diameter remained roughly the same. On the other hand, the size of heterotypic μTP treated with DOX (Fig. 4.2 I-N) was reduced with the extending of exposure

time and the increase of drug concentration. The effect was prominent when treated with DOX at concentration of 16 μg/ml for 72 h. It is well known that reduction in tumor size represents one of the positive effects of an anticancer drug [151].

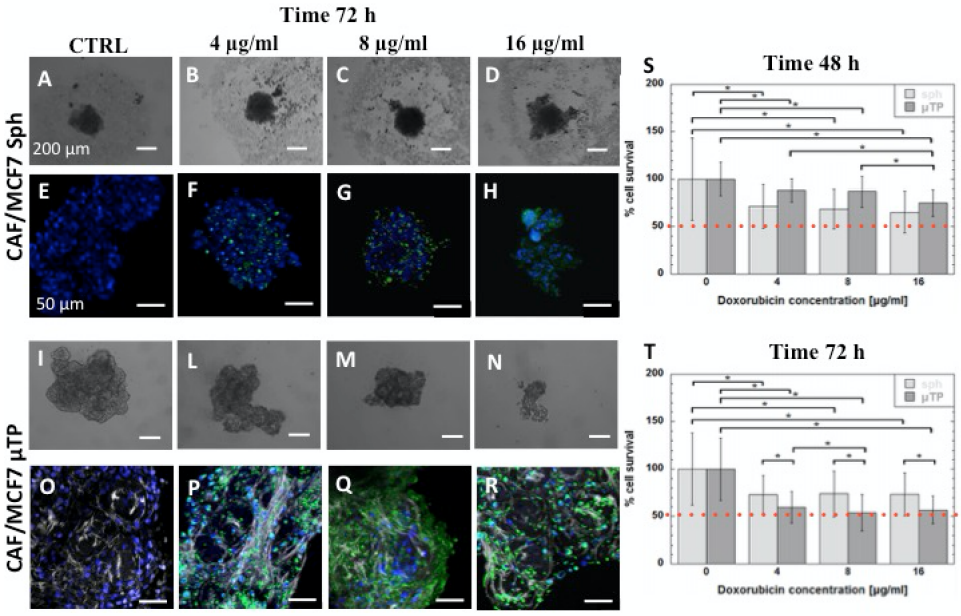

Figure 4.2: Brightfield images of CAF/MCF7 spheroids (A-D) and μTP (I-N) after 72 h of DOX treatment at 4, 8 and 16 μg/ml (A, I controls). Fluorescence distribution of DOX within CAF/MCF7 spheroids (E-H) and μTP (O-R) upon 72 h incubation with DOX at 4, 8 and 16 μg/ml (E, O controls); Cytotoxicity assay in CAF/MCF7 spheroids (light gray) and μTP (middle gray) after treatment with DOX at 4, 8 and 16 μg/ml for 48 (S) and 72 h (T).

Furthermore, the penetration of DOX, which fluoresces in green, was assessed with confocal microscopy. For visualization, cells were stained with DAPI (blue signal). From confocal images (Fig. 4.2 E-H and O-R), is observed an apparent time-dependent DOX penetration for both models. After 72 h of treatment, DOX penetrated into the nuclei of 3D cultured cells in a dose-dependent manner. Especially, DOX displayed a homogeneous and

dose-dependent accumulation region of μTP. After 72 h, DOX penetration is higher in μTP (Fig. 4.2 O- R) than spheroids (Fig. 4.2 F-H) suggesting that μTP structure is less compact than spheroids and thus more readily allows the penetration of drugs at very high concentrations. Furthermore, SHG signal (Fig. 4.2 O-R, in gray scale) was detected only in μTP configuration, indicating the presence of collagen fibers produced and synthesized by fibroblasts. SHG images showed a random distribution of fiber orientations and a wide inter-fiber spacing in tumors. MTT cytotoxicity results shown in Fig. 4.2 S and T, reveals that there is no inhibition effect in cell proliferation after the treatment of CAF/MCF7 spheroids with DOX both 48 and 72 h. On the contrary, the reduction of 50% of cell population in CAF/MCF7 μTP is observed at 8 μg/ml of doxorubicin exposure for 72 h. However, the inhibition of cell viability for CAF/MCF7 μTP was lower than that for the homotypic μTP counterparts. Definitely, MTT results demonstrated that heterotypic cultures with stromal fibroblasts exhibit significantly higher drug resistance that homotypic cultures both in spheroid and μTP model.

4.3.2 μTP and spheroid penetration study

It is well known that the accumulation and penetration of anti-cancer drugs in tumors are essentially to achieve effective chemotherapy responses in cancer therapy. For this reason, the penetration and diffusion of DOX were examined. Penetration was evaluated by analyzing images of DOX fluorescence acquired with magnification 3.5 in order to have a better visualization of DOX intercalation into cell nuclei. For analysis, we chose the intermediate concentration of 8 μg/ml that correspond to the IC_{50} value determined for CAF/MCF7-μTP.

Fig. 4.3 A-B show representative CAF/MCF7 spheroid (Fig. 4.3 A) and microtissue (Fig. 4.3 B) images with 3.5 magnification while Fig. 4.3 C shows quantification of mean fluorescence in both 3D models normalized by area. From quantification analysis, homotypic and heterotypic spheroids showed limited penetration when exposed to 8 μg/ml of free DOX. On the

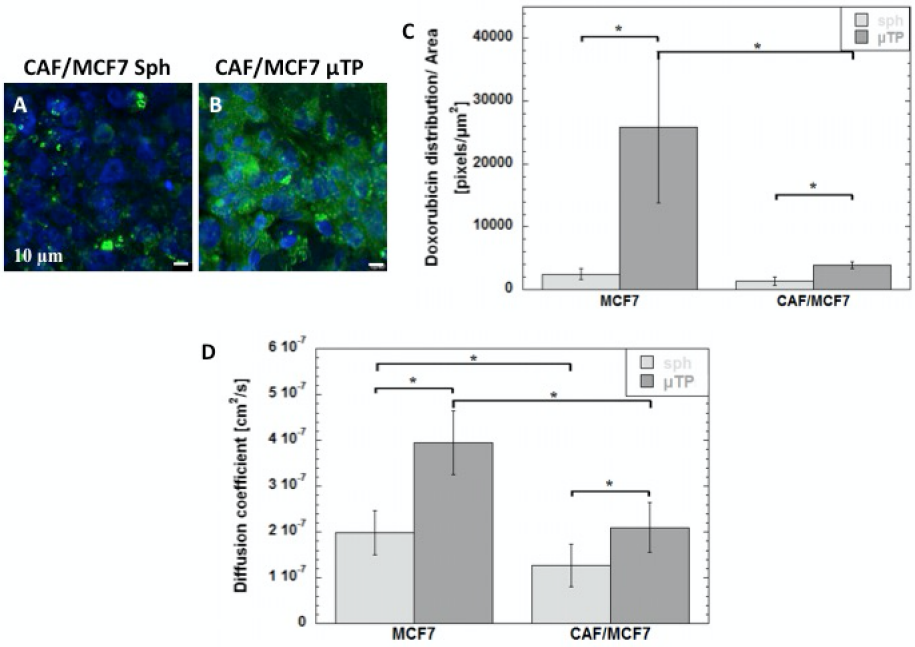

Figure 4.3: Fluorescence images of DOX within CAF/MCF7 spheroids (A) and μTP (B) with magnification 3.4 upon 72 h incubation with DOX at 8 μg/ml; Doxorubicin distribution in CAF/MCF7 spheroids (light gray) and μTP (middle gray) per area after treatment with DOX at 8 μg/ml for 72 h (C); Diffusion coefficients (D) of Fluorescein in CAF/MCF7 spheroids (light gray) and μTP (middle gray). Statistical difference was determined using ANOVA test ($p < 0.05$).

other hand, DOX efficiently penetrated in μTP models, both in homotypic and heterotypic configurations respect to the spheroid counterparts ($p < 0.05$). Furthermore, DOX penetration is lower in CAF/MCF7-μTP respect to MCF7-μTP, because of presence of endogenous ECM. In order to better understand the difference in doxorubicin transport in two models, we have focused on diffusion mechanism through the interstitial space of spheroids and μTP. We measured the diffusion coefficient of fluorescein in homotypic (MCF7) and heterotypic (CAF/MCF7) spheroids and μTP using FRAP, which measures the fluorescent intensity recovery in the bleached region over

time (Fig. 4.3 D). The measured diffusivity within μTP was 3.95 $\pm$ 0.704 E-07 cm^2/s and 2.10 $\pm$ 0.543 E-07 cm^2/s for MCF7 and CAF/MCF7 μTP, respectively. In spheroid model, the diffusion coefficient is equal to 1.98 $\pm$ 0.483 E-07 cm^2/s for MCF7 and 1.27 $\pm$ 0.456 E-07 cm^2/s for CAF/MCF7 culture. In both cases, the diffusion coefficient decreased with the complexity of the system from homotypic to heterotypic culture but increased in μTP configuration respect to spheroid model, at the same cell culture. Definitely, spheroids showed limited diffusion of molecular probe as well as DOX distribution compared to μTP.

4.3.3 Expression of cell adhesion molecules in μTP and spheroid models

Since adhesion molecules play vital roles in cell morphology and function, we also investigated whether the expression of adhesion molecules differed in homotypic (Fig. 4.4 A-B) and heterotypic (Fig. 4.4 C-D) condition in spheroids and μTP.

Since in most solid tumors derived from epithelial tissues, nests of malignant tumor cells are linked through junction proteins such as E-cadherin, claudins and ZO-1 [156], we decided to analyze these three markers by immunofluorescence staining in spheroids and μTP and compared with xenograft models in which MCF7 cells were injected subcutaneously.

Fig. 4.4 A-E show fluorescence images of cell adhesion markers E-cadherin (in red) in homotypic and heterotypic spheroids and μTP, respectively. To better assess the level of expression of intercellular junction, quantification of the staining pattern was carried out using image analysis (Fig. 4.4 F). From quantification analysis we found a higher expression level in the case of spheroids, both homotypic (Fig. 4.4 A) and heterotypic (Fig. 4.4 C) respect to μTP counterparts (Fig. 4.4 B and D) and xenograft model (Fig. 4.4 E) ($p < 0.05$). The same trend was found for Claudin-1 (Fig. 4.5 A-E) and ZO-1 (Fig. 4.6 A-E) expressions in spheroids and μTP. In particular, the level of ZO-1 expression is equal between MCF7 spheroids and μTP (Fig. 4.6 F)

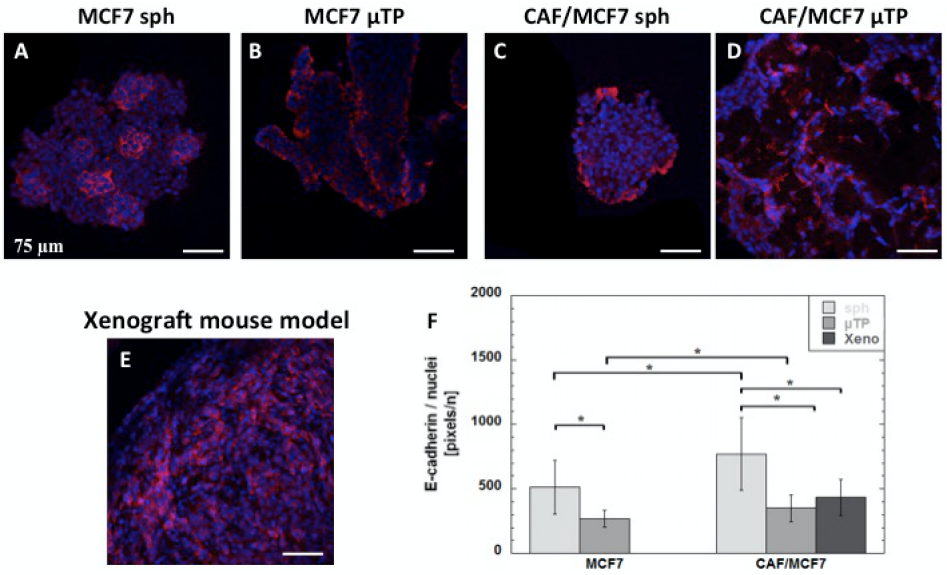

Figure 4.4: E-cadherin fluorescence images (red signal) in MCF7 spheroids (A) and μTP (B), in CAF/MCF7 spheroids (C) and μTP (D) and in xenograft mouse model (E); Quantification of E-cadherin (F) expression (pixels / nuclei) in MCF7 spheroids and μTP, in CAF/MCF7 spheroids and μTP and in xenograft mouse model. Statistical difference was determined using ANOVA test ($p < 0.05$).

($p > 0.05$) but it was shown the loss of this tight junctions when MCF7 were cultured with CAF in heterotypic μTP. These results showed that the expression of adhesion and tight molecules in μTP model was more similar to that of tumors grown *in vivo* than those of spheroid-cultured cells.

4.4 Discussions

In this study, we have compared a 3D homotypic and heterotypic tumor μTP model to the respective spheroid models, in order to assess the difference in terms of chemoresistance between the two models in response to DOX treatment. It is well known that tumor *in vivo* are not merely an aggregation of cancer cells but are composed with other cells of microenvironment that

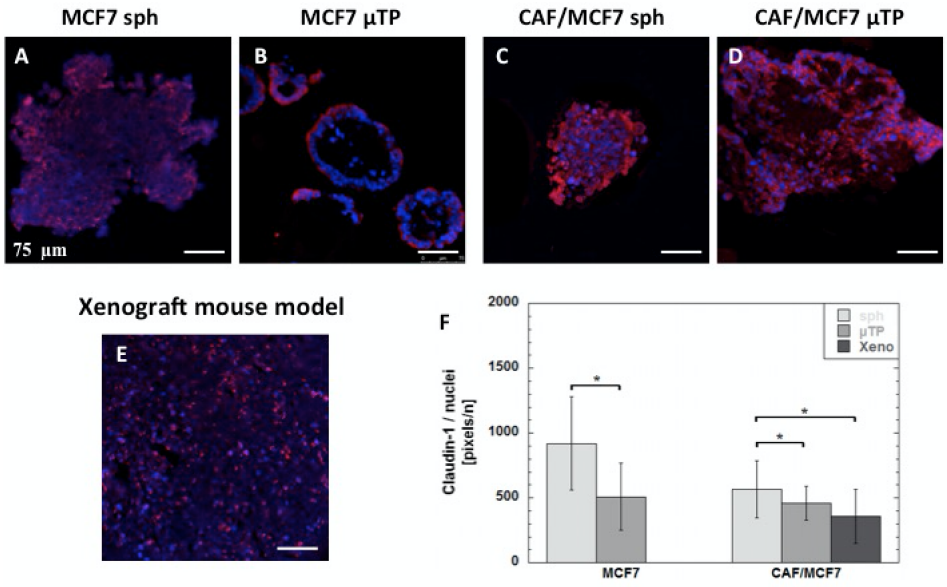

Figure 4.5: Claudin-1 fluorescence images (red signal) in MCF7 spheroids (A) and μTP (B), in CAF/MCF7 spheroids (C) and μTP (D) and in xenograft mouse model (E); Quantification of Claudin-1 (F) expression (pixels / nuclei) in MCF7 spheroids and μTP, in CAF/MCF7 spheroids and μTP and in xenograft mouse model. Statistical difference was determined using ANOVA test ($p < 0.05$).

contribute to drug resistance. Therefore it is important to incorporate this complex structure in models used to study novel cancer therapies. The effect of one of the most commonly used anti-cancer drug, DOX, on MCF7-μTP and CAF/MCF7-μTP was evaluated by cytotoxicity assay, imaging, drug penetration and diffusion studies. The same issues were also investigated on spheroid model, both homotypic and heterotypic. The results of this work demonstrate that CAF/MCF7-μTP are able to better recapitulate the *in vivo* tumor microenvironment, in which cells, in the right context, are embedded in their endogenous ECM, countinously synthesized and remodeled by neighbors fibroblasts cells. In contrast, tumor spheroid that is a multicellular aggregate lacks a controlled microarchitecture and significant ECM re-organization and therefore drug response is distorted. In our model, the

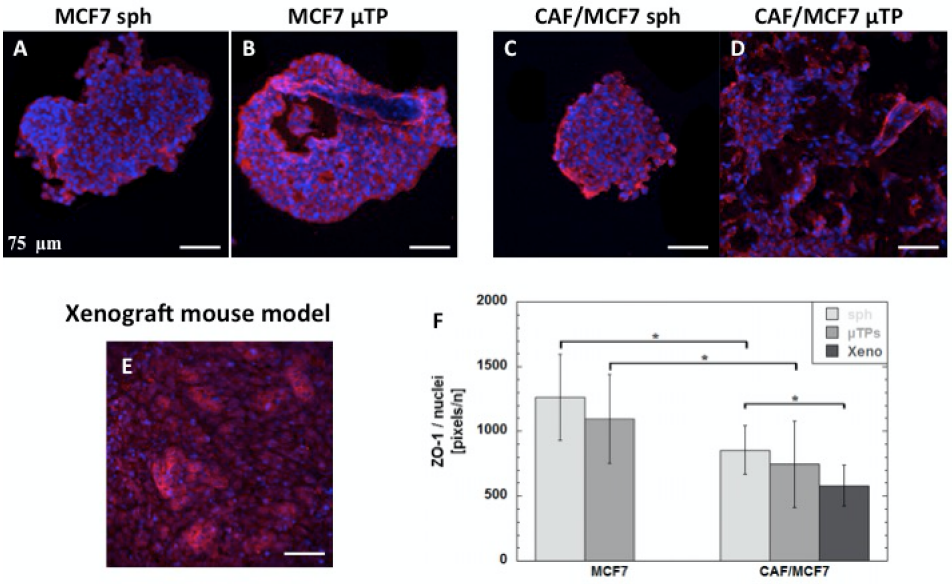

Figure 4.6: ZO-1 fluorescence images (red signal) in MCF7 spheroids (A) and μTP (B), in CAF/MCF7 spheroids (C) and μTP (D) and in xenograft mouse model (E); Quantification of ZO-1 (F) expression (pixels / nuclei) in MCF7 spheroids and μTP, in CAF/MCF7 spheroids and μTP and in xenograft mouse model. Statistical difference was determined using ANOVA test ($p < 0.05$).

presence of the microcarriers allows collagen synthesis and sustains its assembly reproducing the tumor architecture found *in vivo* [44]. Co-culturing cancer cells with fibroblasts in 3D heterotypic μTP can mimic breast cancer heterogeneity, allowing a more physiological response to screening. In both models, the supplementation of fibroblasts into 3D culture not only elicits physico-chemical changes of cancer cells and microenvironment, but also brings about differences in drug response compared to single culture of cancer cells [157].

Furthermore MCF7 spheroid model exhibits higher drug resistance respect to μTP configuration. The possible reasons can be conferred to the spheroid ability to block the diffusion of the drug to the outer layers in

which cells are more proliferative and therefore more sensible to DOX treatment. Indeed, the oxygen gradient within the spheroid provides a hypoxic core consisting of cells more resistant to drug. Consequently a greater drug resistance is showed when MCF7 spheroids are treated with DOX respect to MCF7-μTP. In both cases, the models were limited because of the lack of stromal component and therefore they cannot be used as drug screening platform. When we cultured MCF7 with CAF, drug mass transfer was expected to be much more limited respect to monoculture due to stromal barrier. Recently, a work has demonstrated that heterospheroid conditions with stromal fibroblasts exhibit enhanced resistance to drug over homospheroids [87]. In our study, the co-culture CAF/MCF7 exhibited a significant different sensitivity to DOX when were included both in spheroid or μTP configuration. In particular, drug concentration in CAF/MCF7 spheroids increased over time but it was not sufficient to achieve the IC_{50} value. On the contrary, CAF/MCF7-μTP halved their viability after DOX treatment with a concentration of 8 μg/ml. The different behavior can be attributed to different morphology of models. We also hypothesized that the rapid drug penetration in μTP might be possible due to the greater intercellular space between cells. Therefore, it may be argued that the aforementioned findings are attributable to a diminished drug diffusion rate in spheroids as demonstrated by FRAP experiments. Previous studies using fluorescent drugs or macromolecules have been shown poor penetration of DOX into deeper layers of spheroids [158]. These data strongly confirmed the results obtained in our work in terms of drug penetration in spheroid model. The difference of the cellular distribution of DOX in spheroids and μTP suggested that there are different physical barriers that hinder the diffusion of drugs. The ECM is known to be a physical transport barrier of molecules through tissue. It is composed of fibrous structural proteins (collagen and elastin), adhesive proteins (fibronectin and laminin) and proteoglycans (hyaluronic acid) [156]. Among them, collagen content was a significatively determinant of the diffusive transport of drugs in solid tumors [142]. In our work, we demostrated

the presence of well organized collagen fibers in CAF/MCF7-μTP, but not in CAF/MCF7 spheroids. Furthermore the high porosity and interconnected porous structure in microscaffold lead to quick diffusion of molecules in a liquid environment, which could favor mass transfer for cell aggregates within scaffolds [118]. Although matrix components could be considered a barrier to drug transport, the rapid turnover of ECM on one side and the high porosity and interconnected structure in μTP model on the other side, allowed more drugs to infiltrate more freely inside the matrix structure, increasing DOX anti-cancer activity. These two important aspects enable to have efficient molecular diffusion of drug within the scaffolds present in μTP configuration, similar to small molecular diffusion in the tumor microenvironment *in vivo* [118].

One of the key features of epithelial tumors is the presence of intercellular junctions, which link cells to one another, and act as barriers to the penetration of molecules with a molecular weight greater than 400 Da, as DOX. Several studies have shown that upregulation of epithelial junction proteins was correlated with increased resistance to therapy, including chemotherapeutics [156]. In the last few years, it has become increasingly apparent that cell death, especially apoptosis, strongly depend on cell adhesion [159]. Previous studies using multicellular layer models have shown poor drug distribution into tumors with high packing density [158]. In our case, impaired penetration of anticancer agents through spheroids, both homotypic and heterotypic, derived from cells with tightly packed cells in comparison with loose packing cells in μTP model. Since adhesive properties of cells contribute to resistance to DOX treatment, in this work we further examined one of the most important adhesion junctions, the E-cadherin, in both models. E-cadherin is thought to function as a tumor suppressor in numerous tissues and has been shown to be a useful prognostic indicator for some tumors, illustrating the importance of cell-to-cell adhesion proteins in cancer progression [160]. As reported in recent papers, the presence of strong cell-cell adhesion mediated by E-cadherin prevent cell apoptosis and therefore promote cell survival

[159]. In this way, when CAF/MCF7 spheroids were exposed to DOX treatment, were more resistant to drug due to high cell-cell adhesions. On the contrary, in CAF/MCF7-μTP exhibited lower expression of epithelial cell adhesion markers E-cadherin. The expression of E-cadherin in CAF/MCF7-μTP was quite similar to what found in a xenograft murine model. Moreover, changes in tight junctions have been shown to be an early and key aspect in cancer metastasis [161]. One of the important role of tight junctions is the permeability barrier function that regulates the passage of water, ions and various macromolecules through paracellular spaces [162]. Of the proteins comprising tight junctions, integrate membrane proteins claudin-1 and ZO-1 have been investigated. A previous study reported a significant loss of claudin-1 protein in breast cancer cells, suggesting that this protein may play a role in invasion and metastasis [161]. *Tokes et al.* (2005), have demonstrated a significant loss of claudin-1 protein in breast cancer cells in sections from surgically resected breast specimens by immunostaining [161]. In our work, we reported a loss of claudin-1 and ZO-1 proteins in CAF/MCF7-μTP, showing a quite similar situation in xenograft model. These results are in accordance with previous works in human tumors where levels of ZO-1 were significantly lower in patients with metastatic disease compared with those remaining disease-free [163]. Moreover, these reports of decreased tight junction protein expression in CAF/MCF7 μTP are consistent with the generally accepted idea that tumorigenesis is accompanied by a disruption of tight junctions, a process that may play an important role in the loss of cohesion, invasiveness and lack of differentiation observed in cancer cells [164].

Taken together, comparisons of drug responsiveness of our μTP system with the standard spheroid model indicate that tumors grown in the microcarriers may be more appropriate model to study certain aspects of cancer progression [32]. In particular, the microscaffold provides good spatial interconnectivity between cells, a high surface-to-volume ratio and good porosity for fluid transport. Furthermore, it is also able to mimic the physical interaction of the tumor cells with the microenviroment defined by synthe-

sis of endogenous collagen directly by stromal cells. These results made CAF/MCF7-μTP a more valuable tool for highly predictive drug testing *in vitro*, in comparison to the spheroid model where the cells, being densely packed each other, did not recapitulate the tumor microenvironment *in vivo*.

4.5 Conclusions

In this study, we report a new three-dimensional *in vitro* model that can be used for the investigation of drug response against breast cancer cells. Our system has presented several advantages respect to the classical spheroid model: the biodegradable microscaffolds have a good porosity that provide the spatial interconnectivity between cells and affect the synthesis of endogenous ECM directly by stromal cells. Moreover together with the presence of the ECM, tumor cells have lower expression of adhesion molecules, typical aspect observed during tumorigenesis. Because the morphology of our system is closer to xenograft model respect to the spheroid model observed, it suggests that the μTP system may be a useful *in vitro* screening tool for testing innovative approaches of drug delivery such as nanoparticles sensible to specific characteristic of tumor microenvironment (acidic pH, altered redox potential or up-regulation of specific proteins) [165].

Chapter 5

Delivery of MMP2-responsive Nanoparticles in healthy and tumor microtissues

5.1 Introduction

Conventional cancer chemotherapeutic drugs often fail to kill cancer because their efficacy is altered by nonspecific cell and tissue biodistribution, leading severe adverse effects on normal tissues [166], [167]. This aspect derives from undesirable properties of drugs, such as poor water solubility, low tumor targeting and insufficient cellular drug uptake [168]. Given the progress in material science and pharmaceutics, several typologies of therapeutic nanoparticles have been developed with diverse sizes, architectures and surface properties [167]. These include liposomes, polymeric nanoparticles, micelles, mesoporous silica nanoparticles, dendrimers, carbon nanotubes and inorganic nanoparticles [169]. The clinically significant impact of nanoparticles, regardless of their type, is the improvement of drug efficacy, increasing tumor tissue selectively and minimizing side effects [170]. Indeed, this is achievable by their capacity to increase local drug concentration by carrying the drug to the specific target site [169]. After systemic (intravenous) admin-

istration, drug must first extravasates from the blood system, passes through the ECM (extracellular matrix), binds to cells and then crosses the surface membrane to enter into target cells [166]. During this path, nanoparticles encounter several physiologic barriers such as heterogeneous tumor perfusion, irregular blood flow, high cell density, acidic pH and increased interstitial pressure [171]. In this context, stimuli-responsive nanoparticles are able to achieve controlled drug delivery by exploiting the pathophysiologic characteristic of tumor microenvironment, like lowered interstitial pH or increased levels of enzymes [172]. For example, metalloproteinases (MMPs) are over expressed in a variety of malignant tumors and play a critical role in tumor invasion and progression [173]. Therefore they can be used as a biochemical trigger for drug release during cancer therapy since the inhibition of their proteolytic activity by using tissue inhibitors of the metalloproteinases (TIMPs) was failed [174], [175]. Among MMPs family, MMP-2 (also known as gelatinase A) hydrolyze type IV collagen, degrading ECM matrix and play an important role in metastasis of breast, lung, colorectal and ovarian tumors [176]. In a recent work, *Guarnieri et al.* (2014), proposed the use of a novel nanocarrier able to carry safely doxorubicin in tumor tissues and to respond to MMP-2 enzyme [176]. The nanocarrier is composed by a spherical polystyrene nanoparticle covalently bonded with a Tumor-Activated Prodrug (TAP) composed by polyethylene glycol (PEG), a peptide sequence sensitive to MMP-2 and doxorubicin. The presence of the MMP-2 enzyme *in situ*, leads to the disruption of the bond between the peptide and the doxorubicin, with the consequent diffusion of the drug. The same technology was used by this group to fabricate biodegradable systems based on a FDA-approved material, polyethylene glycol (PEG) [165]. This new system is composed by biodegradable poly(d,l-lactic-co-glycolic acid) (PLGA) - block - polyethylene glycol (PEG) copolymer (namely PELGA), blended with TAP composed of a MMP2-sensitive peptide bound to doxorubicin (DOX) at the C- terminus and to PLGA molecule at the N-terminus [165]. In the present work we tested this MMP-2-stimuli-responsive nanoparticles in terms of DOX release normal

and tumoral 3D heterotypic microtissues (μTP). Indeed, normal μTP were fabricated seeding normal fibroblasts (NF) and epithelial breast cell lines (MCF10) as well as tumoral μTP containing epithelial breast cancer cells (MCF7) and cancer-associated fibroblasts (CAF). It is well recognized that tumor stroma physically limits the penetration of molecular drugs as well as nanotherapeutics into the tumors [166]. Nanoparticle cytotoxicity was tested in heterotypic normal and tumoral μTP to demonstrate their significant selectively. We believe that the use of 3D microtissue model as a nanoparticle delivery platform is able to forecast a more realistic therapy response near to *in vivo* conditions.

5.2 Materials and Methods

5.2.1 Cell type

Normal mammary fibroblasts (NF) and cancer associated fibroblasts (CAF), kindly donated by Kojima's group, were sub-cultured onto 150 mm Petri dishes in DMEM (Dulbecco's Modified Eagle Medium) with high glucose, containing 10% fetal bovine serum, 100 μg/ml L-glutamine, 100 U/ml penicillin / streptomycin. Human non tumorigenic epithelial cell lines (MCF10) from ATCC and human breast adenocarcinoma cells (MCF7) kindly donated by Daidone's group were sub-cultured onto 150 mm Petri dishes in MEBM (Modified Eosin Methylene Blue Agar for medium) and RPMI-1640 (Roswell Park Memorial Institute) respectively, with high glucose, containing 10% fetal bovine serum, 100 μg/ml L-glutamine, 100 U/ml penicillin / streptomycin. Cells were maintained at 37 °C in humidified atmosphere containing 5% CO_2. Fibroblasts were stable transfected with pLVX-DsRed-express2-N1 (λex 554nm, λem 591nm) viral vector (Clontech, USA).

5.2.2 Microbeads production

Gelatin porous microbeads (GPMs) have been prepared by following a previously established protocol [6]. GPMs have been stabilized by crosslink reaction with GPMs glyceraldehydes (GAL), in order to make them stable in aqueous environment at 37 °C, as previously described [6]. GAL at 5% w/w of the microbeads has been used to perform all the experiments.

5.2.3 Dynamic cell seeding

Before using, dry GPMs were sterilized in absolute ethanol 24 h on a rotating plate. Then, GPMs were washed twice in sterile phosphate-buffered saline (PBS) without calcium and magnesium solution. Finally, before cell seeding, PBS was replaced by fresh culture medium. For heterotypic culture (NF/MCF10- and CAF/MCF7-μTP) 50 mg of GPMs were loaded together with $7.5*10^5$ of fibroblasts (30 cell/GMP ratio). To help cell seeding on GMPs an intermittent stirring regime (30 min at 0 rpm, 5 min at 30 rpm) for 6 h has been performed. Then, dynamic cultures were kept under continuous stirring at 30 rpm for up to 12 days. At day 6th, MCF10 and MCF7 cells were added in a ratio 1:3 to NF and CAF cells into spinner flask, respectively. Medium was changed on the first day and every 3 days until the end of the experiments. For fibroblasts, from the day 2nd, 50 μg/ml of ascorbic acid were added.

5.2.4 Cell growth

At the day 1, 6, 7 and 12 of culture, 1 ml aliquot of NF/MCF10- (healthy tissue) and CAF/MCF7-μTP (tumor tissue) were collected from the spinner flask for cell growth monitoring on the GPMs. It's necessary to underline that MCF10 and MCF7 cell counting started from day 7, after 24 h of epithelial cells addition into spinner flasks. Briefly, 200 μl of the same aliquot was transferred to a cell culture dish (w/2 mm grid Nunc) for microcarrier counting, after which the microcarrier suspension was placed in a new 2 ml

tube and washed twice with PBS. To detach cells from microcarriers, μTP were digested by collagenase A (Roche Life sciences, Italy) 60 min at 37 °C, centrifuged 5 min at 2000 rpm, and incubated 5 min in Trypsin (Lonza, Italy). The detached cells were then counted using a hemocytometer.

5.2.5 Masson's Trichrome and confocal imaging

About 1 ml of NF/MCF10- and CAF/MCF7-μTP suspension was fixed in a solution of 10% neutral buffered formalin for 1 h at RT, dehydrated in an incremental series of ethanol (75%, 85%, 95% and 100% twice, each step 30 min at RT) treated with xylene and embedded in paraffin. Successively, the samples were sectioned at a thickness of 7 μm. Masson's trichrome (Sigma Aldrich) staining was performed according to standard protocols. At last, the sections were mounted with Histomount Mounting Solution (Bioptica) on coverslips and the morphological features of μTP were observed with a light microscope (Olympus, BX53).

For confocal imaging, NF/MCF10- and CAF/MCF7-μTP were fixed with 4% paraformaldehyde for 20 min and washed three times with PBS. After nuclei staining with 1 μg/ml of 4',6-diamidino-2-phenylindole (DAPI, Sigma-Aldrich), fluorescence images were acquired (for DAPI λex = 700 nm and λem = 425 $\pm$ 25 nm; for NF and CAF cells λex = 543 nm and λem = 590 $\pm$ 60 nm, water objective 40X with NA = 1.10). Two-photon excited fluorescence has been used to induce Second Harmonic Generation (SHG) and obtain high-resolution images of unstained collagen structures in μTP' ECM (λex = 840 nm, λem = 420 $\pm$ 5 nm).

5.2.6 Immunofluorescence staining, imaging and quantification

For immunofluorescence staining, formalin-fixed and paraffin embedded NF/MCF10- and CAF/MCF7-μTP were unmasked by heat antigen retrieval protocol by citrate buffer; washed with PBS containing 0.2% Triton X-100,

blocked with FBS and 5% BSA solution and incubated with primary antibody MMP-2 (1:200, Abcam UK). Secondary antibody incubation and DAPI staining were performed, before closing the slices with glycerol solution. The fluorescent images, previously acquired by using a multichanneled Leica TCS SP5 II, were analyzed for semi-quantitative evaluation with ImageJ. After threshold, the amount of signal was divided by the total number of cells (previously obtained by counting their nuclei) in each image [114].

5.2.7 Gelatin zymography

Gelatin zymography was performed for both NF/MCF10- and CAF/MCF7-μTP culture surnatans as follows: gel (SDS-PAGE, 10%) was copolymerised with gelatin (0.1%) (Sigma-Aldrich). Electrophoresis was carried out using minigel lab apparatus Mini Protean 3 (Biorad) at a constant voltage of 150 V until the dye reached the bottom of the gel. Following electrophoresis, gel was washed in renaturation buffer (2.5% Triton X-100 in 50 mM Tris- HCl pH 7.5) for 1 h in an orbital shaker. Then the gel was incubated for 18 h at 37 °C in incubation buffer (0.15 M NaCl, 10 mM $CaCl_2$, 0.02% NaN_3 in 50 mM Tris-HCl pH 7.5). Gel was then stained with Coomassie blue and destained with 30% methanol and 10% acetic acid. Areas of enzymatic activity appeared as clear bands over the dark background. Following zymogrphy, the degree of gelatin digestion was quantified using Image J software and the image was digitally inverted, so that the integration of bands was reported as positive values. We reported the pixel intensity of the area of each gelatin-digested band.

5.2.8 Nanoparticle preparation

In this work we tested two types of nanoparticles (NPs) named NP-PELGA-TAP and PELGA-DOX. NP-PELGA-TAP is composed by poly(D,L-lactic-co-glycolic acid) (PLGA) and polyethylene glycol (PEG) copolymer (namely PELGA) blended with a Tumor-Activated Prodrug (TAP) composed of MMP-

2 sensitive peptide bound to Doxorubicin (DOX) and to PLGA chain. The second type of NPs is used as negative control because they lack of MMP-sensitive linker. Both NPs were prepared by nanoprecipitation method according to a previous published work [165]. Briefly, after synthesis of copolymers and conjugates, 1 mg of PELGA and 1 mg of PLGA-TAP were dissolved in 500 μl of acetone. After mixing, the solution was added dropwise with a syringe pump into 12.5 ml of distillated water under magnetic stirring (600 rpm). The organic solvent was evaporated for 3 h and the obtained NP dispersion was sterilized using a 0.22 μm membrane filter. Finally, the reduction in volume (1 ml) of the solution was obtained by serial centrifugations. Furthermore, NP-PELGA-DOX were prepared with the same technique using 1 mg of PELGA-DOX and 1 mg of PELGA.

5.2.9 Drug treatment and confocal imaging

In order to have the same cell density, one NF/MCF10- and CAF/MCF7-μTP were transferred into well of a round bottom 96 well plates. Both μTP were treated with NP-PELGA-TAP and PELGA-DOX at 4 and 8 μg/ml after dilution from a stock solution (40 μg/ml) for 48 and 72 h at 37 °C in humidified atmosphere containing 5% CO_2. One row of 96-wells plate was used as control with 200 μL culture medium only. NF/MCF10- and CAF/MCF7-μTP treated with NPs were washed three times with PBS and fixed in 4% paraformaldehyde in PBS for 20 min. Cell nuclei were stained with 1 μg/ml of DAPI (Sigma-Aldrich). DOX fluorescence was observed under a confocal microscope (Leica) with excitation at 488 nm and emission 515 $\pm$ 15 nm, using a 40X water objective (NA = 1.10).

5.2.10 Cytotoxicity assay

After incubation time, 20 μL of 3-(4,5-dimethylthiazol-2-yl) - 2,5 - diphenyltetrazolium bromide (MTT) solution (5 mg/ml) was added to each well, and the plate was incubated for another 4 h, allowing the viable cells to reduce

the yellow MTT into dark-blue formazan crystals, which were dissolved into 100 μL of dimethyl sulfoxide (DMSO). The absorbance of individual well was measured at 470 nm by a microplate reader (Enspire Multimode Plate Reader PerkinElmer). All experiments were done in triplicates.

5.2.11 Statistical analysis

Differences between two or more groups were evaluated ($p_{value} < 0.05$) using one-way analysis of variance (ANOVA). A Gaussian distribution for each population was assumed. For pair-wise comparisons within each experimental group, Tukey's post test was used.

5.3 Results

In this work we used a novel endogenous stimuli-responsive nanoparticle therapy in normal and tumoral μTP. After characterization of heterotypic μTP in terms of cell proliferation and ECM composition (collagen and MMP-2 expression), nanoparticle cytotoxicity response was investigated.

5.3.1 Cell proliferation in Healthy and Tumor Tissues

The healthy (NF/MCF10-μTP) and tumor (CAF/MCF7-μTP) μTP evolution was evaluated during 12 days of culture. In Fig. 5.1 A-B were reported the cell number *per* μTP unit. In particular, NF and CAF cells started both with 36 $\pm$ 5.57 cells at day 1 and after 12 days of culture they presented a final cell number of 870 $\pm$ 129 and 1635 $\pm$ 136 respectively. At the same time, for normal and tumor epithelial cell lines, the cell number increased from 113 $\pm$ 45 and 248 $\pm$ 20 at day 7 (after 1 day of cell loading into spinner flask) to 561 $\pm$ 113 and 2200 $\pm$ 306, respectively. These results highlighted the greater proliferative capability of both tumor epithelial and stromal cells compared to normal counterparts.

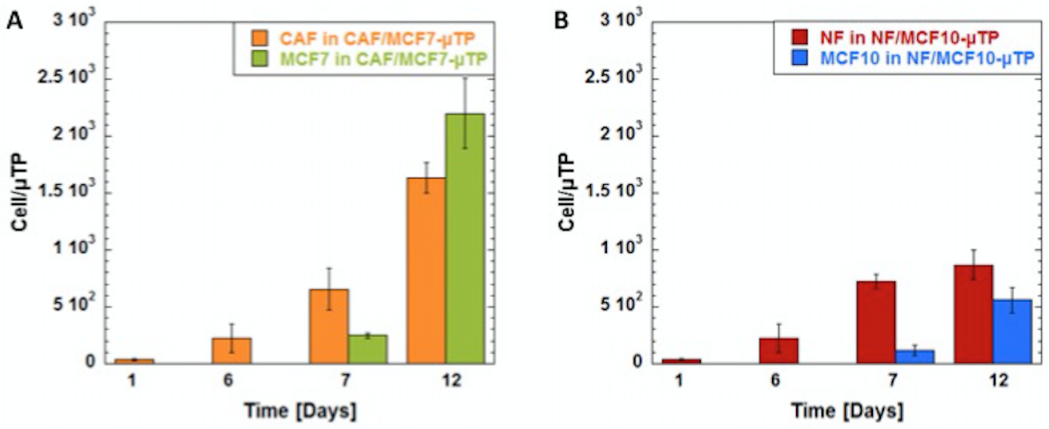

Figure 5.1: Cell proliferation of CAF and MCF7 cells in tumor tissue (A) and NF and MCF10 cells in healthy tissue (B).

5.3.2 ECM morphology and composition

From literature, it has been recognized the tumor microenvironment contribute to resistance to molecular and nanoscale medicine [102]. Among abnormal physiological characteristics, high stromal fraction in tumors lead to diminished delivery as well as effectiveness of drugs [102]. For these reasons, we verify if in our heterotypic μTP model, stromal cells are in the right conditions to be able to produce a dense matrix structure, by performing immunostaining and SHG analysis. Fig. 5.2 A-B reported the histological sections stained by Masson Trichrome of normal and tumoral μTP. From images it was possible to distinguish the red signal related to the microbeads, the purple signal due to the cells staining and blue signal of the endogenous ECM. We also identify fibrillar collagen level from both tissues by SHG signal (gray scale) as indicated in Fig. 5.2 C and D for healthy and tumor tissue, respectively. In both cases the SHG signal was strong indicating a massive collagen fibers deposition but with different organization. Taken together, this data indicated the presence of endogenous ECM synthesized by stromal cells NF and CAF in μTP configuration.

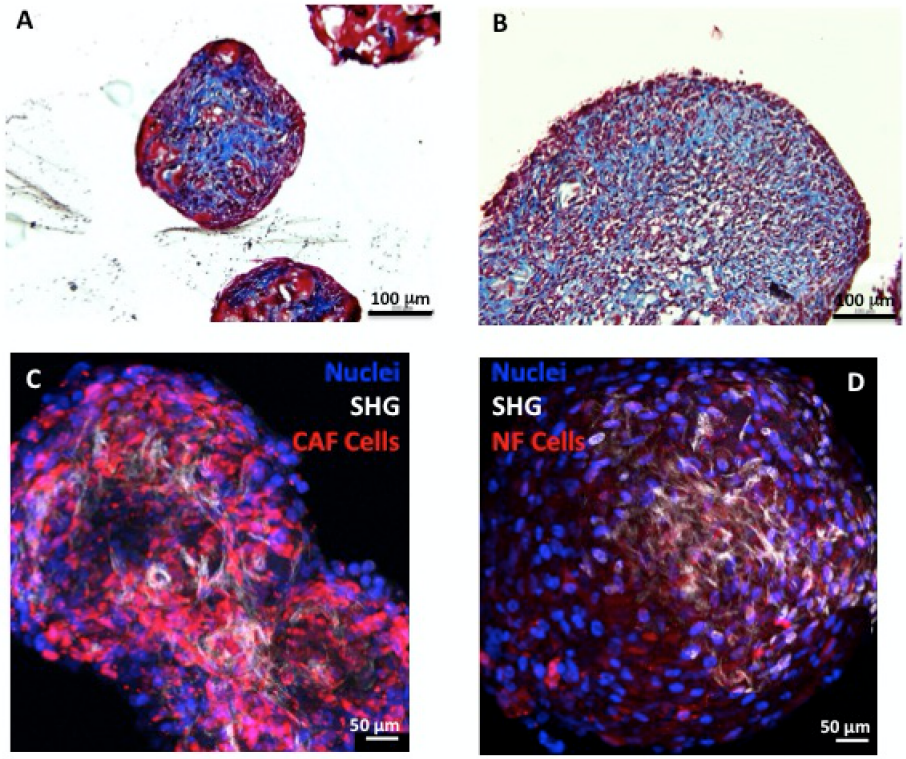

Figure 5.2: Masson's Trichrome staining in CAF/MCF7- (A) and NF/MCF10-μTP (B); Scale bar = 100 μm. SHG images of CAF/MCF7- (C) and NF/MCF10-μTP (D); Scale bar = 50 μm (cell nuclei in blue, CAF and NF in red and SHG signal in gray).

5.3.3 MMP2 over-expression in Tumor Tissue

In this work, the expression and enzymatic activity of endogenous MMP-2 secreted by cells in NF/MCF10- and CAF/MCF7-μTP were verified by immunostaining and zymography analysis. From both techniques, high MMP-2 expression was detected in tumor tissue compared to normal one. Indeed, as shown in Fig. 5.3 A-B, tumor tissue (Fig. 5.3 A) express greater level of MMP-2 protein than normal tissue (Fig. 5.3 B). These findings are confirmed by quantification analysis ($p < 0.05$, Fig. 5.3 C). Furthermore, zymography results demonstrated that, although the inactive form of MMP-2 was greater in normal tissue ($p < 0.05$), a higher amount of MMP-2 activity was found

in CAF/MCF7-μTP compared to NF/MCF10-μTP ($p < 0.05$) (Fig. 5.3 D).

5.3.4 *In vitro* NP Imaging and Cytotoxicity

Having established that our tumor μTP model is a powerful tool for MMP-2-mediated drug delivery *via* nanoparticles, we next evaluated the therapeutic effectiveness of endogenous stimuli-responsive NP-PELGA-TAP. Therefore NF/MCF10- and CAF/MCF7-μTP were exposed to NP-PELGA-TAP and PELGA-DOX for 48 and 72 h. Figure 5.4 shows fluorescence images of tumor and healthy tissue after both NPs treatment at 4 μg/ml for 72 h. As shown in Fig. 5.4 A a diffused fluorescence was noticed around cells in CAF/MCF7-

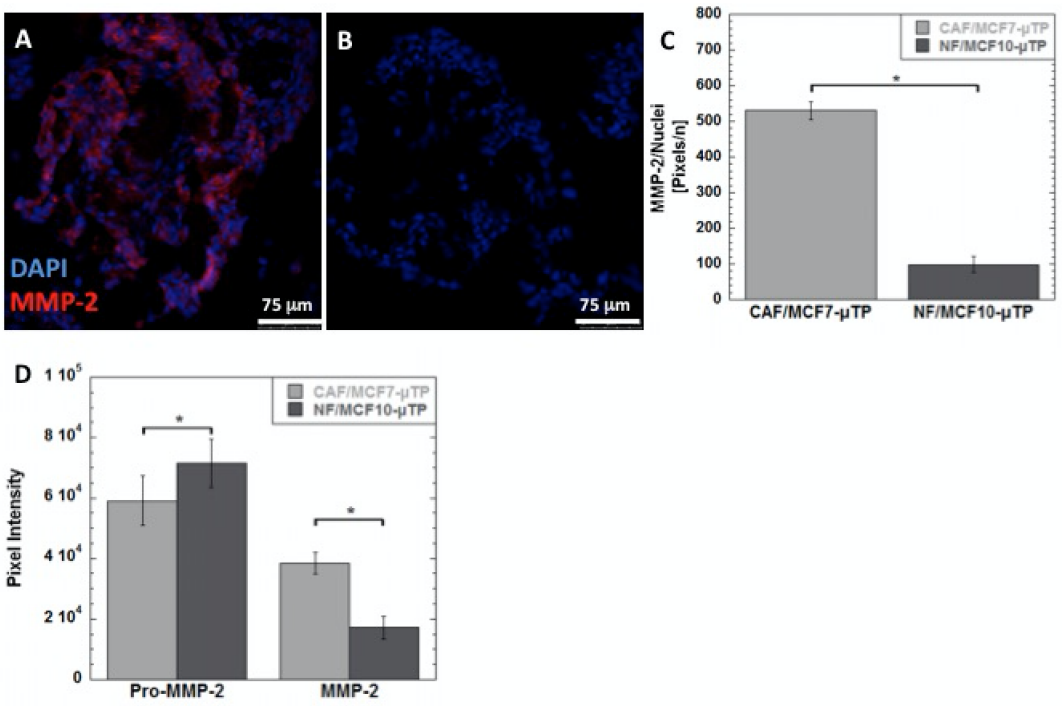

Figure 5.3: MMP-2 levels in CAF/MCF7- and NF/MCF10-μTP. Immunofluorescence staining of MMP-2 protein (red) in CAF/MCF7- (A) and NF/MCF10-μTP (B); quantification analysis of MMP-2 obtained from immunofluorescence (C); gelatin zymography showing the MMP-2 activity of CAF/MCF7- and NF/MCF10-μTP (D).

μTP incubated with NP-PELGA-TAP, indicating the release of free DOX. On the other hand, a very low spotted fluorescence was observed when tumor tissue is put in contact with NP-PELGA-DOX for 72 h (Fig. 5.4 B). More interestingly, normal tissue have shown a low or not detectable fluorescence of free DOX after both NPs type incubation (Fig. 5.4 C-D).

From brightfield images (Fig. 5.4 E-L) a reduction of μTP diameter was identified in tumor tissue after both NPs treatment (Fig. 4F-G) compared to control (Fig. 5.4 E). Indeed, outer cells detached from the μTP were observed (indicated by white arrow, Fig. 5.4 F-G). Finally, the NF/MCF10-μTP diameter remained roughly the same (Fig. 5.4 I-L) respect to control (Fig. 5.4 H), indicating lower DOX release from NPs in healthy tissue.

We next investigated the cytotoxicity of NP-PELGA-TAP and PELGA-DOX in NF/MCF10- and CAF/MCF7-μTP as a function of cell viability. Fig. 5.5 shows cell viability percentage of treated μTP normalized to non-

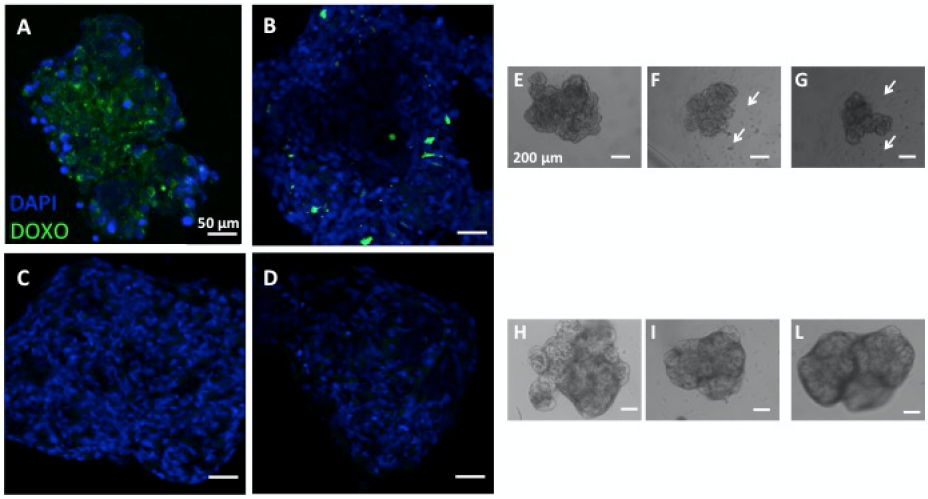

Figure 5.4: Fluorescence distribution of DOX within CAF/MCF7-μTP upon 72 h incubation with PELGA-TAP (A) and PELGA-DOX (B) and within NF/MCF10-μTP (C, D) at 4 μg/ml; scale bar = 50 μm. Brightfield images of CAF/MCF7- (E-G) and NF/MCF10-μTP (H-L) after 72h of PELGA-TAP and PELGA-DOX treatment at 4 μg/ml (E-H controls); scale bar = 200 μm

treated μTP as a function of drug concentration after 48 and 72 h of treatment. For tumor tissue, it was observed an increase in cytotoxic response with incubation time raise (dark gray bar in Fig. 5.5 A-B) for both NPs treatments. However, only after NP-PELGA-TAP treatment, CAF/MCF7-μTP achieved the IC_{50} value at 4 μg/ml for 72h. This value indicates the concentration at which 50% of cellular activity is inhibited. On the contrary, no inhibition effect in cell proliferation was found in NF/MCF10-μTP after both NPs treatment (Fig. 5.5 C-D). These results demonstrate the selective cytotoxic effect of MMP-2-stimuli responsive NP-PELGA-TAP.

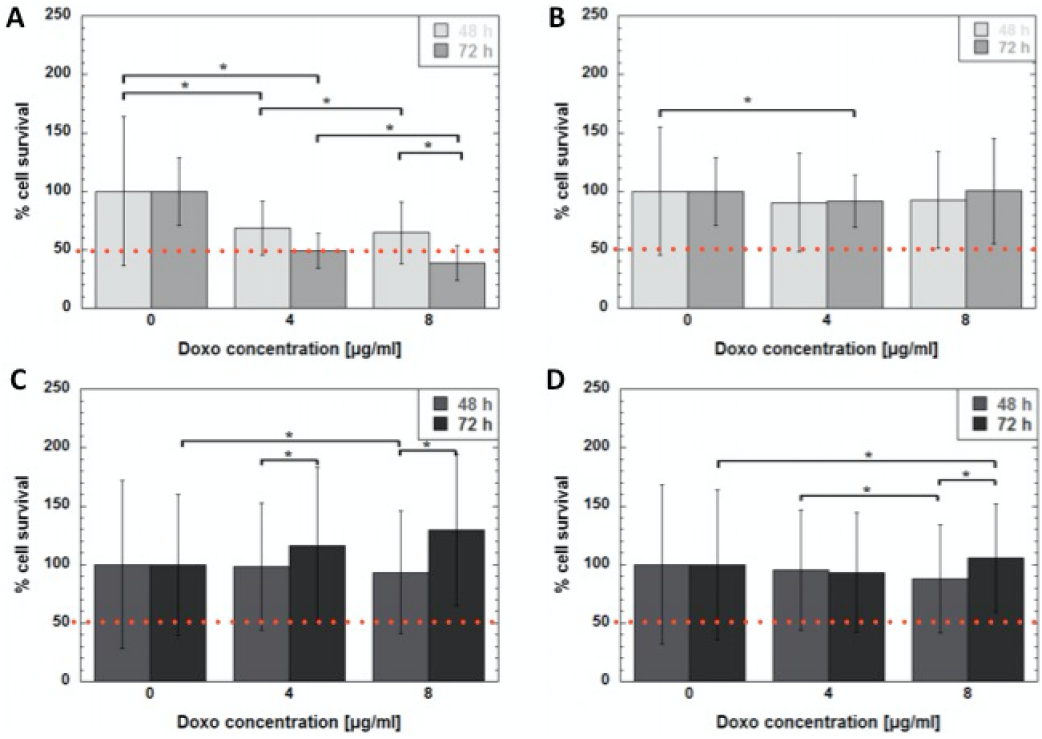

Figure 5.5: Cytotoxicity assay in tumor CAF/MCF7-μTP after treatment with NP-PELGA-TAP (A) and PELGA-DOX (B) and in healthy tissue NF/MCF7-μTP after NP-PELGA-TAP (C) and PELGA-DOX (D) treatment at 4 and 8 μg/ml for 48 and 72 h.

5.3.5 Discussions

In the present study we apply endogenous stimuli responsive nanoparticles to normal and tumroal heterotypic μTP composed of both epithelial and stromal cells. This heterotypic model better recapitulates cell microenvironment compared to other more used 3D cell culture like spheroids or cells embedded in natural or synthetic gels. In particular the tumor microenvironment is composed not only by tumor cell aggregates but also contains other cells of stroma milieu like CAF that contribute to hinder drug distribution [14]. Therefore it is important to incorporate stromal elements in *in vitro* tumor tissue models, as we did, introducing CAF cells that are able to produce and synthesize ECM. The interaction between cells and extracellular matrix plays a pivotal role in cellular behaviors such as proliferation and migration. In fact as demonstrated by growth curves, tumor epithelial (MCF7) and stromal (CAF) cells have greater proliferative capability due to tumor nature compared to normal counterparts (MCF10 and NF, respectively). Therefore it should be emphasized the presence of endogenous ECM as shown by Masson's Trichrome staining and SHG signal, demonstrating a more complex *in vitro* 3D tissue model able to mimic tumor microenvironment seen *in vivo*. On the other side, nanoparticles as drug delivery carriers have received a lot of attention in the last decades. Their success is mainly due to the improved accumulation of active drugs at disease sites, reducing systemic toxicity in healthy neighbors zones. Recently, stimuli-responsive nanoparticles has been emerging as the most promising strategy [177]. This approach is able to further increase tumor specificity and effectiveness of nanoparticles, releasing high concentrations of cytotoxic drugs in presence of cellular/extracellular stimuli of chemical, biochemical or physical origin. Some of these stimuli are naturally occurring *in vivo* like MMP-2 overexpression in tumor tissues [178]. Many works are presented focusing on the development of NPs responsive to MMP-2 presence. Especially in a recent work, Cantisani et al. (2015), exploited a strategy of drug targeting of tumors using nanoparticles that release cytotoxic drugs in response to specific physiological variations

typical of tumor tissue [165]. It is well-known that MMP-2 are overexpressed in most tumors, like breast cancer [179]. Because MMP-2 expression has a role in tumor progression and invasion, this feature was chosen as a trigger for the release of drug payload. Compared to other previous works [180], in this case drug release is mediated by MMP-2 cleavage in the extracellular space not by cellular uptake. In this work we combine the use of MMP-2 responsive nanoparticles to μTP for a more valuable drug testing. We previously verify if in our tissue model a MMP-2 overexpression occurred at extracellular level. As demonstrated by immunofluorescence signal quantification and by zymography analysis, MMP-2 expression in CAF/MCF7-μTP was greater than NF/MCF10-μTP. Consequently, the higher MMP-2 level in CAF/MCF7-μTP efficiently cleaved the peptide drug-polymer bond, allowing the DOX liberation in the extracellular space. In this way it was possible to obtain a significantly reduction of cell viability compared to NP control (PELGA-DOX) without the MMP-sensitive linker. In the last case, the reduced cytotoxic effect was due to the covalent bound of DOX to NPs that not promoting the leakage of drug. These results are in accordance with a previous work [165] where the disaggregation of tumor spheroids is reached after 48 h of incubation. In our case, the cytotoxic effect was reached later, after 72 h of NP treatments. The reason is mainly due to the difference in tumor configuration. In our work the tumor tissue is heterotypic, composed not only by tumor tissue but also by stroma. Therefore the presence of stromal component contributes to drug resistance [181] delaying the therapeutic effects. Furthermore, NP-PELGA-TAP specificity was demonstrated in healthy tissue in which the low presence of extracellular MMP-2 was detected. Consequently not significantly cytotoxic effect was found in NF/MCF10-μTP. On the contrary, in the presence of MMP-2 overexpression, stimuli-responsive NPs are able to favor DOX penetration within tumor matrix after enzymatic cleavage. In this way a reduction of drug dose as well as an improved therapeutic efficacy can be reached.

In summary, this study shows the feasibility of MMP-2-mediated drug

release in tumor breast tissue that closely reflects the human pathophysiology. In this way, DOX despite its high cytotoxicity when was in the free state, can be safely carried through healthy tissues. The release of the drug and therefore its desired cytotoxic action towards tumor cells could be induced only in the presence of MMP-2. As this model closely reflects the human pathophysiology, we believe that therapeutic strategies that are confirmed in this model are more likely to translate to humans, avoiding the use of time-consuming xenograft models.

5.4 Conclusions

In this work a recently validated formulation of endogenous stimuli-responsive nanoparticles and the 3D μTP approach was combined. In order to have a better pre-clinical evaluation of anticancer drugs, the proposed heterotypic 3D μTP model closely resembles *in vivo* tumor microenvironment due to the presence of high proliferative tumor cell capability and dense matrix structure. In this way, the cytotoxic results obtained after NP-PELGA-TAP treatment, accurately forecast tumor's *in vivo* response. Furthermore, the integration of prodrug concept and endogenous stimuli in nanoparticles, lead the accumulation of cytotoxic drug in the extracellular space of tumor, resulting in enhanced anticancer activity and reducing undesirable side effects on healthy tissues.

Bibliography

[1] Jing Zhang and Jinsong Liu. Tumor stroma as targets for cancer therapy. *Pharmacology & therapeutics*, 137(2):200–215, 2013.

[2] Genichiro Ishii, Atsushi Ochiai, and Shinya Neri. Phenotypic and functional heterogeneity of cancer-associated fibroblast within the tumor microenvironment. *Advanced drug delivery reviews*, 2015.

[3] Isaac M Adjei and Sharma Blanka. Modulation of the tumor microenvironment for cancer treatment: A biomaterials approach. *Journal of functional biomaterials*, 6(1):81–103, 2015.

[4] Cynthia E Weber and Paul C Kuo. The tumor microenvironment. *Surgical oncology*, 21(3):172–177, 2012.

[5] Xian Xu, Mary C Farach-Carson, and Xinqiao Jia. Three-dimensional in vitro tumor models for cancer research and drug evaluation. *Biotechnology advances*, 32(7):1256–1268, 2014.

[6] Giorgia Imparato, Francesco Urciuolo, Costantino Casale, and Paolo A Netti. The role of microscaffold properties in controlling the collagen assembly in 3d dermis equivalent using modular tissue engineering. *Biomaterials*, 34(32):7851–7861, 2013.

[7] Claudio R Thoma, Miriam Zimmermann, Irina Agarkova, Jens M Kelm, and Wilhelm Krek. 3d cell culture systems modeling tumor growth determinants in cancer target discovery. *Advanced drug delivery reviews*, 69:29–41, 2014.

[8] Maria Håkanson, Edna Cukierman, and Mirren Charnley. Miniaturized pre-clinical cancer models as research and diagnostic tools. *Advanced drug delivery reviews*, 69:52–66, 2014.

[9] Bumsoo Han, Chunjing Qu, Kinam Park, Stephen F Konieczny, and Murray Korc. Recapitulation of complex transport and action of drugs at the tumor microenvironment using tumor-microenvironment-on-chip. *Cancer letters*, 2015.

[10] Vasiliki Gkretsi, Andreas Stylianou, Panagiotis Papageorgis, Christiana Polydorou, and Triantafyllos Stylianopoulos. Remodeling components of the tumor microenvironment to enhance cancer therapy. *Frontiers in oncology*, 5, 2015.

[11] Peter DelNero, Young Hye Song, and Claudia Fischbach. Micro-engineered tumor models: insights & opportunities from a physical sciences-oncology perspective. *Biomedical microdevices*, pages 1–11, 2013.

[12] Zahraa I Khamis, Ziad J Sahab, and Qing-Xiang Amy Sang. Active roles of tumor stroma in breast cancer metastasis. *International journal of breast cancer*, 2012, 2012.

[13] Kathleen Burke, Ping Tang, and Edward Brown. Second harmonic generation reveals matrix alterations during breast tumor progression. *Journal of biomedical optics*, 18(3):031106–031106, 2013.

[14] Matthew W Conklin and Patricia J Keely. Why the stroma matters in breast cancer: insights into breast cancer patient outcomes through the examination of stromal biomarkers. *Cell adhesion & migration*, 6(3):249–260, 2012.

[15] Marcela Otranto, Vincent Sarrazy, Frédéric Bonté, Boris Hinz, Giulio Gabbiani, and Alexis Desmouliere. The role of the myofibroblast in

tumor stroma remodeling. *Cell adhesion & migration*, 6(3):203–219, 2012.

[16] Junko Iijima, Kenjiro Konno, and Naoki Itano. Inflammatory alterations of the extracellular matrix in the tumor microenvironment. *Cancers*, 3(3):3189–3205, 2011.

[17] Thea D Tlsty and Lisa M Coussens. Tumor stroma and regulation of cancer development. *Annu. Rev. Pathol. Mech. Dis.*, 1:119–150, 2006.

[18] Hanchen Li, Xueli Fan, and JeanMarie Houghton. Tumor microenvironment: the role of the tumor stroma in cancer. *Journal of cellular biochemistry*, 101(4):805–815, 2007.

[19] Tingjiao Liu, Bingcheng Lin, and Jianhua Qin. Carcinoma-associated fibroblasts promoted tumor spheroid invasion on a microfluidic 3d co-culture device. *Lab on a Chip*, 10(13):1671–1677, 2010.

[20] Laura Kass, Janine T Erler, Micah Dembo, and Valerie M Weaver. Mammary epithelial cell: influence of extracellular matrix composition and organization during development and tumorigenesis. *The international journal of biochemistry & cell biology*, 39(11):1987–1994, 2007.

[21] Roy M Bremnes, Tom Dønnem, Samer Al-Saad, Khalid Al-Shibli, Sigve Andersen, Rafael Sirera, Carlos Camps, Inigo Marinez, and Lill-Tove Busund. The role of tumor stroma in cancer progression and prognosis: emphasis on carcinoma-associated fibroblasts and non-small cell lung cancer. *Journal of Thoracic Oncology*, 6(1):209–217, 2011.

[22] Janna Paulsson, Tobias Sjöblom, Patrick Micke, Fredrik Pontén, Göran Landberg, Carl-Henrik Heldin, Jonas Bergh, Donal J Brennan, Karin Jirström, and Arne Östman. Prognostic significance of stromal platelet-derived growth factor β-receptor expression in human breast cancer. *The American journal of pathology*, 175(1):334–341, 2009.

[23] Girdhari Rijal and Weimin Li. 3d scaffolds in breast cancer research. *Biomaterials*, 81:135–156, 2016.

[24] Hendrik Ungefroren, Susanne Sebens, Daniel Seidl, Hendrik Lehnert, and Ralf Hass. Interaction of tumor cells with the microenvironment. *Cell Commun Signal*, 9(18):992–1009, 2011.

[25] Andrew W Holle, Jennifer L Young, and Joachim P Spatz. In vitro cancer cell–ecm interactions inform in vivo cancer treatment. *Advanced drug delivery reviews*, 2015.

[26] HH Nienhuis, SBM Gaykema, H Timmer-Bosscha, M Jalving, AH Brouwers, MN Lub-de Hooge, B van der Vegt, B Overmoyer, EGE de Vries, and CP Schröder. Targeting breast cancer through its microenvironment: Current status of preclinical and clinical research in finding relevant targets. *Pharmacology & therapeutics*, 147:63–79, 2015.

[27] Thomas R Cox and Janine T Erler. Remodeling and homeostasis of the extracellular matrix: implications for fibrotic diseases and cancer. *Disease models & mechanisms*, 4(2):165–178, 2011.

[28] Kerry J Davies. The complex interaction of matrix metalloproteinases in the migration of cancer cells through breast tissue stroma. *International journal of breast cancer*, 2014, 2014.

[29] Ruchi Malik, Peter I Lelkes, and Edna Cukierman. Biomechanical and biochemical remodeling of stromal extracellular matrix in cancer. *Trends in biotechnology*, 33(4):230–236, 2015.

[30] Brigitte Bauvois. New facets of matrix metalloproteinases mmp-2 and mmp-9 as cell surface transducers: outside-in signaling and relationship to tumor progression. *Biochimica et Biophysica Acta (BBA)-Reviews on Cancer*, 1825(1):29–36, 2012.

[31] Mikala Egeblad, Morten G Rasch, and Valerie M Weaver. Dynamic interplay between the collagen scaffold and tumor evolution. *Current opinion in cell biology*, 22(5):697–706, 2010.

[32] Claudia Fischbach, Ruth Chen, Takuya Matsumoto, Tobias Schmelzle, Joan S Brugge, Peter J Polverini, and David J Mooney. Engineering tumors with 3d scaffolds. *Nature methods*, 4(10):855–860, 2007.

[33] Anne Kultti, Chunmei Zhao, Netai C Singha, Susan Zimmerman, Ryan J Osgood, Rebecca Symons, Ping Jiang, Xiaoming Li, Curtis B Thompson, Jeffrey R Infante, et al. Accumulation of extracellular hyaluronan by hyaluronan synthase 3 promotes tumor growth and modulates the pancreatic cancer microenvironment. *BioMed research international*, 2014, 2014.

[34] Jan Brábek, Claudia T Mierke, Daniel Rösel, Pavel Veselỳ, and Ben Fabry. The role of the tissue microenvironment in the regulation of cancer cell motility and invasion. *Cell Commun Signal*, 8:22, 2010.

[35] Paolo P Provenzano, David R Inman, Kevin W Eliceiri, Justin G Knittel, Long Yan, Curtis T Rueden, John G White, and Patricia J Keely. Collagen density promotes mammary tumor initiation and progression. *BMC medicine*, 6(1):11, 2008.

[36] Michael D Amatangelo, Daniel E Bassi, Andrés JP Klein-Szanto, and Edna Cukierman. Stroma-derived three-dimensional matrices are necessary and sufficient to promote desmoplastic differentiation of normal fibroblasts. *The American journal of pathology*, 167(2):475–488, 2005.

[37] Dorothy A Beacham and Edna Cukierman. Stromagenesis: the changing face of fibroblastic microenvironments during tumor progression. In *Seminars in cancer biology*, volume 15, pages 329–341. Elsevier, 2005.

[38] Stephanie Alexander, Bettina Weigelin, Frank Winkler, and Peter Friedl. Preclinical intravital microscopy of the tumour-stroma inter-

face: invasion, metastasis, and therapy response. *Current opinion in cell biology*, 25(5):659–671, 2013.

[39] Andrew G Clark and Danijela Matic Vignjevic. Modes of cancer cell invasion and the role of the microenvironment. *Current opinion in cell biology*, 36:13–22, 2015.

[40] Paolo P Provenzano, Kevin W Eliceiri, Jay M Campbell, David R Inman, John G White, and Patricia J Keely. Collagen reorganization at the tumor-stromal interface facilitates local invasion. *BMC medicine*, 4(1):38, 2006.

[41] Bo Ri Seo, Peter DelNero, and Claudia Fischbach. In vitro models of tumor vessels and matrix: Engineering approaches to investigate transport limitations and drug delivery in cancer. *Advanced drug delivery reviews*, 69:205–216, 2014.

[42] Yvonne Peck and Dong-An Wang. Three-dimensionally engineered biomimetic tissue models for in vitro drug evaluation: delivery, efficacy and toxicity. *Expert opinion on drug delivery*, 10(3):369–383, 2013.

[43] Emily Burdett, F Kurtis Kasper, Antonios G Mikos, and Joseph A Ludwig. Engineering tumors: a tissue engineering perspective in cancer biology. *Tissue Engineering Part B: Reviews*, 16(3):351–359, 2010.

[44] G Imparato, F Urciuolo, and PA Netti. In vitro three-dimensional models in cancer research: a review. *International Materials Reviews*, 60(6):297–311, 2015.

[45] Mireia Alemany-Ribes and Carlos E Semino. Bioengineering 3d environments for cancer models. *Advanced drug delivery reviews*, 79:40–49, 2014.

[46] Marta F Estrada, Sofia P Rebelo, Emma J Davies, Marta T Pinto, Hugo Pereira, Vítor E Santo, Matthew J Smalley, Simon T Barry,

Emilio J Gualda, Paula M Alves, et al. Modelling the tumour microenvironment in long-term microencapsulated 3d co-cultures recapitulates phenotypic features of disease progression. *Biomaterials*, 78:50–61, 2016.

[47] David Herrmann, James RW Conway, Claire Vennin, Astrid Magenau, William G Hughes, Paul Timpson, et al. Three-dimensional cancer models mimic cell-matrix interactions in the tumour microenvironment. *Carcinogenesis*, page bgu108, 2014.

[48] Tamal Das and Suman Chakraborty. Perspective: Flicking with flow: Can microfluidics revolutionize the cancer research? *Biomicrofluidics*, 7(1):011811, 2013.

[49] Yanan Du, Edward Lo, Shamsher Ali, and Ali Khademhosseini. Directed assembly of cell-laden microgels for fabrication of 3d tissue constructs. *Proceedings of the National Academy of Sciences*, 105(28):9522–9527, 2008.

[50] Alison P McGuigan and Michael V Sefton. Vascularized organoid engineered by modular assembly enables blood perfusion. *Proceedings of the National Academy of Sciences*, 103(31):11461–11466, 2006.

[51] Carmela Palmiero, Giorgia Imparato, Francesco Urciuolo, and Paolo Netti. Engineered dermal equivalent tissue in vitro by assembly of microtissue precursors. *Acta biomaterialia*, 6(7):2548–2553, 2010.

[52] Dongeun Huh, Geraldine A Hamilton, and Donald E Ingber. From 3d cell culture to organs-on-chips. *Trends in cell biology*, 21(12):745–754, 2011.

[53] Dan Gao, Hongxia Liu, Yuyang Jiang, and Jin-Ming Lin. Recent developments in microfluidic devices for in vitro cell culture for cell-biology research. *TrAC Trends in Analytical Chemistry*, 35:150–164, 2012.

[54] Niraj K Inamdar and Jeffrey T Borenstein. Microfluidic cell culture models for tissue engineering. *Current opinion in biotechnology*, 22(5):681–689, 2011.

[55] Camilla Luni, Elena Serena, and Nicola Elvassore. Human-on-chip for therapy development and fundamental science. *Current opinion in biotechnology*, 25:45–50, 2014.

[56] William J Polacheck, Ioannis K Zervantonakis, and Roger D Kamm. Tumor cell migration in complex microenvironments. *Cellular and Molecular Life Sciences*, 70(8):1335–1356, 2013.

[57] Colin L Walsh, Brett M Babin, Rachel W Kasinskas, Jean A Foster, Marissa J McGarry, and Neil S Forbes. A multipurpose microfluidic device designed to mimic microenvironment gradients and develop targeted cancer therapeutics. *Lab on a Chip*, 9(4):545–554, 2009.

[58] William J Polacheck, Joseph L Charest, and Roger D Kamm. Interstitial flow influences direction of tumor cell migration through competing mechanisms. *Proceedings of the National Academy of Sciences*, 108(27):11115–11120, 2011.

[59] Cole R Drifka, Kevin W Eliceiri, Sharon M Weber, and W John Kao. A bioengineered heterotypic stroma–cancer microenvironment model to study pancreatic ductal adenocarcinoma. *Lab on a Chip*, 13(19):3965–3975, 2013.

[60] Yoonseok Choi, Eunjeh Hyun, Jeongyun Seo, Cassidy Blundell, Hee Chan Kim, Eunhee Lee, Su Hyun Lee, Aree Moon, Woo Kyung Moon, and Dongeun Huh. A microengineered pathophysiological model of early-stage breast cancer. *Lab on a Chip*, 15(16):3350–3357, 2015.

[61] Rakesh K Jain, Lance L Munn, and Dai Fukumura. Dissecting tumour pathophysiology using intravital microscopy. *Nature Reviews Cancer*, 2(4):266–276, 2002.

[62] Tord Hompland, Arne Erikson, Mikael Lindgren, Tore Lindmo, and Catharina de Lange Davies. Second-harmonic generation in collagen as a potential cancer diagnostic parameter. *Journal of biomedical optics*, 13(5):054050–054050, 2008.

[63] Wenyan Hu, Hui Li, Chunyou Wang, Shanmiao Gou, and Ling Fu. Characterization of collagen fibers by means of texture analysis of second harmonic generation images using orientation-dependent gray level co-occurrence matrix method. *Journal of biomedical optics*, 17(2):0260071–0260079, 2012.

[64] Shuangmu Zhuo, Jianxin Chen, Guizhu Wu, Shusen Xie, Liqin Zheng, Xingshan Jiang, and Xiaoqin Zhu. Quantitatively linking collagen alteration and epithelial tumor progression by second harmonic generation microscopy. *Applied Physics Letters*, 96(21):213704, 2010.

[65] Javier Adur, Vitor B Pelegati, Andre A de Thomaz, Lilia D'Souza-Li, Maria do Carmo Assunção, Fátima Bottcher-Luiz, Liliana ALA Andrade, and Carlos L Cesar. Quantitative changes in human epithelial cancers and osteogenesis imperfecta disease detected using nonlinear multicontrast microscopy. *Journal of biomedical optics*, 17(8):0814071–08140710, 2012.

[66] Javier Adur, Hernandes F Carvalho, Carlos L Cesar, and Víctor H Casco. Nonlinear optical microscopy signal processing strategies in cancer. *Cancer informatics*, 13:67, 2014.

[67] Fabienne Danhier, Olivier Feron, and Véronique Préat. To exploit the tumor microenvironment: passive and active tumor targeting of nanocarriers for anti-cancer drug delivery. *Journal of Controlled Release*, 148(2):135–146, 2010.

[68] Lei Miao, C Michael Lin, and Leaf Huang. Stromal barriers and strategies for the delivery of nanomedicine to desmoplastic tumors. *Journal of Controlled Release*, 219:192–204, 2015.

[69] EL Da Rocha, LM Porto, and CR Rambo. Nanotechnology meets 3d in vitro models: Tissue engineered tumors and cancer therapies. *Materials Science and Engineering: C*, 34:270–279, 2014.

[70] Triantafyllos Stylianopoulos, Ming-Zher Poh, Numpon Insin, Moungi G Bawendi, Dai Fukumura, Lance L Munn, and Rakesh K Jain. Diffusion of particles in the extracellular matrix: the effect of repulsive electrostatic interactions. *Biophysical journal*, 99(5):1342–1349, 2010.

[71] Triantafyllos Stylianopoulos, Benjamin Diop-Frimpong, Lance L Munn, and Rakesh K Jain. Diffusion anisotropy in collagen gels and tumors: the effect of fiber network orientation. *Biophysical journal*, 99(10):3119–3128, 2010.

[72] Qian Tan, Jasdeep K Saggar, Man Yu, Marina Wang, and Ian F Tannock. Mechanisms of drug resistance related to the microenvironment of solid tumors and possible strategies to inhibit them. *The Cancer Journal*, 21(4):254–262, 2015.

[73] Andrew I Minchinton and Ian F Tannock. Drug penetration in solid tumours. *Nature Reviews Cancer*, 6(8):583–592, 2006.

[74] TS Girton, TR Oegema, and RT Tranquillo. Exploiting glycation to stiffen and strengthen tissue equivalents for tissue engineering. *Journal of biomedical materials research*, 46(1):87–92, 1999.

[75] JL-S Au, SH Jang, J Zheng, C-T Chen, S Song, L Hu, and MG Wientjes. Determinants of drug delivery and transport to solid tumors. *Journal of controlled release*, 74(1):31–46, 2001.

[76] Fei Xing, Jamila Saidou, and Kounosuke Watabe. Cancer associated fibroblasts (cafs) in tumor microenvironment. *Frontiers in bioscience: a journal and virtual library*, 15:166, 2010.

[77] Neil A Bhowmick, Eric G Neilson, and Harold L Moses. Stromal fibroblasts in cancer initiation and progression. *Nature*, 432(7015):332–337, 2004.

[78] Raghu Kalluri and Michael Zeisberg. Fibroblasts in cancer. *Nature Reviews Cancer*, 6(5):392–401, 2006.

[79] Silva Krause, Maricel V Maffini, Ana M Soto, and Carlos Sonnenschein. The microenvironment determines the breast cancer cells' phenotype: organization of mcf7 cells in 3d cultures. *BMC cancer*, 10(1):1, 2010.

[80] Leoni A Kunz-Schughart, Paula Heyder, Josef Schroeder, and Ruth Knuechel. A heterologous 3-d coculture model of breast tumor cells and fibroblasts to study tumor-associated fibroblast differentiation. *Experimental cell research*, 266(1):74–86, 2001.

[81] Jason C Tung, J Matthew Barnes, Shraddha R Desai, Christopher Sistrunk, Matthew W Conklin, Pepper Schedin, Kevin W Eliceiri, Patricia J Keely, Victoria L Seewaldt, and Valerie M Weaver. Tumor mechanics and metabolic dysfunction. *Free Radical Biology and Medicine*, 79:269–280, 2015.

[82] Michael I Koukourakis, Alexandra Giatromanolaki, Adrian L Harris, and Efthimios Sivridis. Comparison of metabolic pathways between cancer cells and stromal cells in colorectal carcinomas: a metabolic survival role for tumor-associated stroma. *Cancer research*, 66(2):632–637, 2006.

[83] Min Fang, Jingping Yuan, Chunwei Peng, and Yan Li. Collagen as a double-edged sword in tumor progression. *Tumor Biology*, 35(4):2871–2882, 2014.

[84] Oliver Ingo Hoffmann, Christian Ilmberger, Stefanie Magosch, Mareile Joka, Karl-Walter Jauch, and Barbara Mayer. Impact of the spheroid

model complexity on drug response. *Journal of biotechnology*, 205:14–23, 2015.

[85] Helmut Dolznig, Christian Rupp, Christina Puri, Christian Haslinger, Norbert Schweifer, Elisabeth Wieser, Dontscho Kerjaschki, and Pilar Garin-Chesa. Modeling colon adenocarcinomas in vitro: a 3d co-culture system induces cancer-relevant pathways upon tumor cell and stromal fibroblast interaction. *The American journal of pathology*, 179(1):487–501, 2011.

[86] Eelco Fennema, Nicolas Rivron, Jeroen Rouwkema, Clemens van Blitterswijk, and Jan de Boer. Spheroid culture as a tool for creating 3d complex tissues. *Trends in biotechnology*, 31(2):108–115, 2013.

[87] Derek Yip and Cheul H Cho. A multicellular 3d heterospheroid model of liver tumor and stromal cells in collagen gel for anti-cancer drug testing. *Biochemical and biophysical research communications*, 433(3):327–332, 2013.

[88] Kjell Nilsson, Ferenc Buzsaky, and Klaus Mosbach. Growth of anchorage–dependent cells on macroporous microcarriers. *Nature Biotechnology*, 4(11):989–990, 1986.

[89] Karoly Jakab, Cyrille Norotte, Francoise Marga, Keith Murphy, Gordana Vunjak-Novakovic, and Gabor Forgacs. Tissue engineering by self-assembly and bio-printing of living cells. *Biofabrication*, 2(2):022001, 2010.

[90] Geeta Mehta, Amy Y Hsiao, Marylou Ingram, Gary D Luker, and Shuichi Takayama. Opportunities and challenges for use of tumor spheroids as models to test drug delivery and efficacy. *Journal of controlled release*, 164(2):192–204, 2012.

[91] Paolo Cirri and Paola Chiarugi. Cancer-associated-fibroblasts and tumour cells: a diabolic liaison driving cancer progression. *Cancer and Metastasis Reviews*, 31(1-2):195–208, 2012.

[92] Jason W Locasale and Lewis C Cantley. Altered metabolism in cancer. *Bmc Biology*, 8(1):1, 2010.

[93] Ubaldo E Martinez-Outschoorn, Stephanos Pavlides, Anthony Howell, Richard G Pestell, Herbert B Tanowitz, Federica Sotgia, and Michael P Lisanti. Stromal–epithelial metabolic coupling in cancer: integrating autophagy and metabolism in the tumor microenvironment. *The international journal of biochemistry & cell biology*, 43(7):1045–1051, 2011.

[94] Annette S Vincent, Than T Phan, Anandaroop Mukhopadhyay, Hwee Y Lim, Barry Halliwell, and Kim P Wong. Human skin keloid fibroblasts display bioenergetics of cancer cells. *Journal of Investigative Dermatology*, 128(3):702–709, 2008.

[95] Stefan Walenta and Wolfgang F Mueller-Klieser. Lactate: mirror and motor of tumor malignancy. In *Seminars in radiation oncology*, volume 14, pages 267–274. Elsevier, 2004.

[96] Sabato Fusco, Valeria Panzetta, Valerio Embrione, and Paolo A Netti. Crosstalk between focal adhesions and material mechanical properties governs cell mechanics and functions. *Acta biomaterialia*, 23:63–71, 2015.

[97] Andrew D Doyle and Kenneth M Yamada. Mechanosensing via cell-matrix adhesions in 3d microenvironments. *Experimental cell research*, 2015.

[98] M Veiseh and EA Turley. Hyaluronan metabolism in remodeling extracellular matrix: probes for imaging and therapy of breast cancer. *Integrative Biology*, 3(4):304–315, 2011.

[99] Peter Friedl and Stephanie Alexander. Cancer invasion and the microenvironment: plasticity and reciprocity. *Cell*, 147(5):992–1009, 2011.

[100] Dewi Harjanto and Muhammad H Zaman. Modeling extracellular matrix reorganization in 3d environments. *PloS one*, 8(1):e52509, 2013.

[101] Paolo P Provenzano, Kevin W Eliceiri, Long Yan, Aude Ada-Nguema, Matthew W Conklin, David R Inman, and Patricia J Keely. Nonlinear optical imaging of cellular processes in breast cancer. *Microscopy and Microanalysis*, 14(06):532–548, 2008.

[102] Vikash P Chauhan, Triantafyllos Stylianopoulos, Yves Boucher, and Rakesh K Jain. Delivery of molecular and nanoscale medicine to tumors: transport barriers and strategies. *Annual review of chemical and biomolecular engineering*, 2:281–298, 2011.

[103] Pei-Chun Wu, Tsung-Yuan Hsieh, Zen-Uong Tsai, and Tzu-Ming Liu. In vivo quantification of the structural changes of collagens in a melanoma microenvironment with second and third harmonic generation microscopy. *Scientific reports*, 5, 2015.

[104] G Imparato, C Casale, S Scamardella, F Urciuolo, M Bimonte, F Apone, G Colucci, and PA Netti. A novel engineered dermis for in vitro photodamage research. *Journal of tissue engineering and regenerative medicine*, 2016.

[105] DAI Fukumura, Dan G Duda, Lance L Munn, and Rakesh K Jain. Tumor microvasculature and microenvironment: Novel insights through intravital imaging in pre-clinical models. *Microcirculation*, 17(3):206–225, 2010.

[106] Rakesh K Jain. Normalizing tumor microenvironment to treat cancer: bench to bedside to biomarkers. *Journal of Clinical Oncology*, 31(17):2205–2218, 2013.

[107] Yamin Yang, Xiaochuan Yang, Jin Zou, Chao Jia, Yue Hu, Henry Du, and Hongjun Wang. Evaluation of photodynamic therapy efficiency using an in vitro three-dimensional microfluidic breast cancer tissue model. *Lab on a Chip*, 15(3):735–744, 2015.

[108] Edmond WK Young. Advances in microfluidic cell culture systems for studying angiogenesis. *Journal of laboratory automation*, 18(6):427–436, 2013.

[109] Lauren L Bischel, David J Beebe, and Kyung E Sung. Microfluidic model of ductal carcinoma in situ with 3d, organotypic structure. *BMC cancer*, 15(1):1, 2015.

[110] CB Raub, AJ Putnam, BJ Tromberg, and SC George. Predicting bulk mechanical properties of cellularized collagen gels using multiphoton microscopy. *Acta biomaterialia*, 6(12):4657–4665, 2010.

[111] Nishanth V Menon, Yon Jin Chuah, Bin Cao, Mayasari Lim, and Yuejun Kang. A microfluidic co-culture system to monitor tumor-stromal interactions on a chip. *Biomicrofluidics*, 8(6):064118, 2014.

[112] Alexandre Albanese, Alan K Lam, Edward A Sykes, Jonathan V Rocheleau, and Warren CW Chan. Tumour-on-a-chip provides an optical window into nanoparticle tissue transport. *Nature communications*, 4, 2013.

[113] F Urciuolo, A Garziano, G Imparato, V Panzetta, S Fusco, C Casale, and PA Netti. Biophysical properties of dermal building-blocks affects extra cellular matrix assembly in 3d endogenous macrotissue. *Biofabrication*, 8(1):015010, 2016.

[114] IRENE Acerbi, Luke Cassereau, I Dean, Quanming Shi, Alfred Au, Catherine Park, Yunn-Yi Chen, Jan Liphardt, ES Hwang, and Valerie Marie Weaver. Human breast cancer invasion and aggression cor-

relates with ecm stiffening and immune cell infiltration. *Integrative Biology*, 2015.

[115] A Garziano, F Urciuolo, G Imparato, F Martorina, B Corrado, and P Netti. A micro-perfusion bioreactor for on line investigation of ecm remodeling under hydrodynamic and biochemical stimulation. *Lab on a Chip*, 2016.

[116] Christopher B Raub, Jay Unruh, Vinod Suresh, Tatiana Krasieva, Tore Lindmo, Enrico Gratton, Bruce J Tromberg, and Steven C George. Image correlation spectroscopy of multiphoton images correlates with collagen mechanical properties. *Biophysical journal*, 94(6):2361–2373, 2008.

[117] Luis F Alonzo, Monica L Moya, Venktesh S Shirure, and Steven C George. Microfluidic device to control interstitial flow-mediated homotypic and heterotypic cellular communication. *Lab on a Chip*, 15(17):3521–3529, 2015.

[118] Lina W Dunne, Zhao Huang, Weixu Meng, Xuejun Fan, Ningyan Zhang, Qixu Zhang, and Zhiqiang An. Human decellularized adipose tissue scaffold as a model for breast cancer cell growth and drug treatments. *Biomaterials*, 35(18):4940–4949, 2014.

[119] Kyung Eun Sung, Xiaojing Su, Erwin Berthier, Carolyn Pehlke, Andreas Friedl, and David J Beebe. Understanding the impact of 2d and 3d fibroblast cultures on in vitro breast cancer models. *PloS one*, 8(10):e76373, 2013.

[120] Claudio Luparello. Aspects of collagen changes in breast cancer. *Journal of Carcinogenesis & Mutagenesis*, 2013, 2013.

[121] Boris Hinz, Sem H Phan, Victor J Thannickal, Andrea Galli, Marie-Luce Bochaton-Piallat, and Giulio Gabbiani. The myofibroblast:

one function, multiple origins. *The American journal of pathology*, 170(6):1807–1816, 2007.

[122] Daniel Öhlund, Ela Elyada, and David Tuveson. Fibroblast heterogeneity in the cancer wound. *The Journal of experimental medicine*, 211(8):1503–1523, 2014.

[123] Kristian Pietras, Tobias Sjöblom, Kristofer Rubin, Carl-Henrik Heldin, and Arne Östman. Pdgf receptors as cancer drug targets. *Cancer cell*, 3(5):439–443, 2003.

[124] Tsi-Hsuan Hsu, Jian-Long Xiao, Yu-Wei Tsao, Yi-Lun Kao, Shih-Hao Huang, Wei-Yu Liao, and Chau-Hwang Lee. Analysis of the paracrine loop between cancer cells and fibroblasts using a microfluidic chip. *Lab on a chip*, 11(10):1808–1814, 2011.

[125] Kathleen Burke and Edward Brown. The use of second harmonic generation to image the extracellular matrix during tumor progression. *IntraVital*, 3(3):e984509, 2014.

[126] Carlos P Huang, Jente Lu, Hyeryung Seon, Abraham P Lee, Lisa A Flanagan, Ho-Young Kim, Andrew J Putnam, and Noo Li Jeon. Engineering microscale cellular niches for three-dimensional multicellular co-cultures. *Lab on a Chip*, 9(12):1740–1748, 2009.

[127] Chrisostomi Gialeli, Achilleas D Theocharis, and Nikos K Karamanos. Roles of matrix metalloproteinases in cancer progression and their pharmacological targeting. *FeBS Journal*, 278(1):16–27, 2011.

[128] Christina H Stuelten, Stacey DaCosta Byfield, Praveen R Arany, Tatiana S Karpova, William G Stetler-Stevenson, and Anita B Roberts. Breast cancer cells induce stromal fibroblasts to express mmp-9 via secretion of tnf-α and tgf-β. *Journal of cell science*, 118(10):2143–2153, 2005.

[129] Sonia Saad, David J Gottlieb, Kenneth F Bradstock, Christopher M Overall, and Linda J Bendall. Cancer cell-associated fibronectin induces release of matrix metalloproteinase-2 from normal fibroblasts. *Cancer research*, 62(1):283–289, 2002.

[130] S Saad, LJ Bendall, A James, DJ Gottlieb, and KF Bradstock. Coculture of breast cancer cells and bone marrow fibroblasts induces expression of the metalloproteinase mmp-2. *Breast Cancer Res Treat*, 63:105–115, 2000.

[131] A Ito, S Nakajima, Y Sasaguri, H Nagase, and Y Mori. Co-culture of human breast adenocarcinoma mcf-7 cells and human dermal fibroblasts enhances the production of matrix metalloproteinases 1, 2 and 3 in fibroblasts. *British journal of cancer*, 71(5):1039, 1995.

[132] Christian F Singer, Nicole Kronsteiner, Erika Marton, Marion Kubista, Kevin J Cullen, Kora Hirtenlehner, Michael Seifert, and Ernst Kubista. Mmp-2 and mmp-9 expression in breast cancer-derived human fibroblasts is differentially regulated by stromal-epithelial interactions. *Breast cancer research and treatment*, 72(1):69–77, 2002.

[133] Thomas N Wang, Daniel Albo, and George P Tuszynski. Fibroblasts promote breast cancer cell invasion by upregulating tumor matrix metalloproteinase–9 production. *Surgery*, 132(2):220–225, 2002.

[134] PG Dedes, Ch Gialeli, AI Tsonis, I Kanakis, AD Theocharis, D Kletsas, GN Tzanakakis, and NK Karamanos. Expression of matrix macromolecules and functional properties of breast cancer cells are modulated by the bisphosphonate zoledronic acid. *Biochimica et Biophysica Acta (BBA)-General Subjects*, 1820(12):1926–1939, 2012.

[135] Kathryn L Schwertfeger, Mary K Cowman, Patrick G Telmer, Eva A Turley, and James B McCarthy. Hyaluronan, inflammation, and breast cancer progression. *Frontiers in immunology*, 6, 2015.

[136] Javier Adur, Vitor B Pelegati, Andre A de Thomaz, Mariana O Baratti, Liliana ALA Andrade, Hernandes F Carvalho, Fátima Bottcher-Luiz, and Carlos Lenz Cesar. Second harmonic generation microscopy as a powerful diagnostic imaging modality for human ovarian cancer. *Journal of biophotonics*, 7(1-2):37–48, 2014.

[137] Nathaniel D Kirkpatrick, Molly A Brewer, and Urs Utzinger. Endogenous optical biomarkers of ovarian cancer evaluated with multiphoton microscopy. *Cancer Epidemiology Biomarkers & Prevention*, 16(10):2048–2057, 2007.

[138] Shuangmu Zhuo, Jianxin Chen, Shusen Xie, Zhibin Hong, and Xingshan Jiang. Extracting diagnostic stromal organization features based on intrinsic two-photon excited fluorescence and second-harmonic generation signals. *Journal of biomedical optics*, 14(2):020503–020503, 2009.

[139] Erin M Johnson and William M Deen. Hydraulic permeability of agarose gels. *AIChE Journal*, 42(5):1220–1224, 1996.

[140] E De Rosa, F Urciuolo, C Borselli, D Gerbasio, G Imparato, and PA Netti. Time and space evolution of transport properties in agarose-chondrocyte constructs. *Tissue engineering*, 12(8):2193–2201, 2006.

[141] Rakesh K Jain, John D Martin, and Triantafyllos Stylianopoulos. The role of mechanical forces in tumor growth and therapy. *Annual review of biomedical engineering*, 16:321, 2014.

[142] Paolo A Netti, David A Berk, Melody A Swartz, Alan J Grodzinsky, and Rakesh K Jain. Role of extracellular matrix assembly in interstitial transport in solid tumors. *Cancer research*, 60(9):2497–2503, 2000.

[143] C de L Davies, DA Berk, A Pluen, and RK Jain. Comparison of igg diffusion and extracellular matrix composition in rhabdomyosarcomas

grown in mice versus in vitro as spheroids reveals the role of host stromal cells. *British journal of cancer*, 86(10):1639–1644, 2002.

[144] Live Eikenes, Ingunn Tufto, Edrun A Schnell, Astrid Bjørkøy, and Catharina De Lange Davies. Effect of collagenase and hyaluronidase on free and anomalous diffusion in multicellular spheroids and xenografts. *Anticancer research*, 30(2):359–368, 2010.

[145] George Alexandrakis, Edward B Brown, Ricky T Tong, Trevor D McKee, Robert B Campbell, Yves Boucher, and Rakesh K Jain. Two-photon fluorescence correlation microscopy reveals the two-phase nature of transport in tumors. *Nature medicine*, 10(2):203–207, 2004.

[146] Alain Pluen, Yves Boucher, Saroja Ramanujan, Trevor D McKee, Takeshi Gohongi, Emmanuelle di Tomaso, Edward B Brown, Yotaro Izumi, Robert B Campbell, David A Berk, et al. Role of tumor–host interactions in interstitial diffusion of macromolecules: cranial vs. subcutaneous tumors. *Proceedings of the National Academy of Sciences*, 98(8):4628–4633, 2001.

[147] Edward Brown, Trevor McKee, Alain Pluen, Brian Seed, Yves Boucher, Rakesh K Jain, et al. Dynamic imaging of collagen and its modulation in tumors in vivo using second-harmonic generation. *Nature medicine*, 9(6):796–800, 2003.

[148] V Shenoy and J Rosenblatt. Diffusion of macromolecules in collagen and hyaluronic acid, rigid-rod-flexible polymer, composite matrixes. *Macromolecules*, 28(26):8751–8758, 1995.

[149] Jayme L Horning, Sanjeeb K Sahoo, Sivakumar Vijayaraghavalu, Sanja Dimitrijevic, Jaspreet K Vasir, Tapan K Jain, Amulya K Panda, and Vinod Labhasetwar. 3-d tumor model for in vitro evaluation of anticancer drugs. *Molecular pharmaceutics*, 5(5):849–862, 2008.

[150] Aranzazu Villasante and Gordana Vunjak-Novakovic. Tissue-engineered models of human tumors for cancer research. *Expert opinion on drug discovery*, 10(3):257–268, 2015.

[151] Xulang Zhang, Wei Wang, Weiting Yu, Yubing Xie, Xiaohui Zhang, Ying Zhang, and Xiaojun Ma. Development of an in vitro multicellular tumor spheroid model using microencapsulation and its application in anticancer drug screening and testing. *Biotechnology progress*, 21(4):1289–1296, 2005.

[152] Siew-Min Ong, Ziqing Zhao, Talha Arooz, Deqiang Zhao, Shufang Zhang, Tiehua Du, Martin Wasser, Danny van Noort, and Hanry Yu. Engineering a scaffold-free 3d tumor model for in vitro drug penetration studies. *Biomaterials*, 31(6):1180–1190, 2010.

[153] Won Jin Ho, Edward A Pham, Jun W Kim, Christopher W Ng, Jae H Kim, Daniel T Kamei, and Benjamin M Wu. Incorporation of multicellular spheroids into 3-d polymeric scaffolds provides an improved tumor model for screening anticancer drugs. *Cancer science*, 101(12):2637–2643, 2010.

[154] Daniela Loessner, Kathryn S Stok, Matthias P Lutolf, Dietmar W Hutmacher, Judith A Clements, and Simone C Rizzi. Bioengineered 3d platform to explore cell–ecm interactions and drug resistance of epithelial ovarian cancer cells. *Biomaterials*, 31(32):8494–8506, 2010.

[155] Agnieszka Marczak, Marta Denel-Bobrowska, Aneta Rogalska, Małgorzata Łukawska, and Irena Oszczapowicz. Cytotoxicity and induction of apoptosis by formamidinodoxorubicins in comparison to doxorubicin in human ovarian adenocarcinoma cells. *Environmental toxicology and pharmacology*, 39(1):369–383, 2015.

[156] Il-Kyu Choi, Robert Strauss, Maximilian Richter, Chae-Ok Yun, and André Lieber. Strategies to increase drug penetration in solid tumors.

Ways to improve tumor uptake and penetration of drugs into solid tumors, page 22, 2014.

[157] Ashlee K Clark, Anna V Taubenberger, Renea A Taylor, Birunthi Niranjan, Zhen Y Chea, Elena Zotenko, Shirly Sieh, John S Pedersen, Sam Norden, Mark Frydenberg, et al. A bioengineered microenvironment to quantitatively measure the tumorigenic properties of cancer-associated fibroblasts in human prostate cancer. *Biomaterials*, 34(20):4777–4785, 2013.

[158] Rama Grantab, Shankar Sivananthan, and Ian F Tannock. The penetration of anticancer drugs through tumor tissue as a function of cellular adhesion and packing density of tumor cells. *Cancer research*, 66(2):1033–1039, 2006.

[159] Maria Teresa Santini, Gabriella Rainaldi, and Pietro Luigi Indovina. Apoptosis, cell adhesion and the extracellular matrix in the three-dimensional growth of multicellular tumor spheroids. *Critical reviews in oncology/hematology*, 36(2):75–87, 2000.

[160] Satoko Morohashi, Tomomi Kusumi, Fuyuki Sato, Hiroki Odagiri, Hiroki Chiba, Shuichi Yoshihara, Kenichi Hakamada, Mutsuo Sasaki, and Hiroshi Kijima. Decreased expression of claudin-1 correlates with recurrence status in breast cancer. *International journal of molecular medicine*, 20(2):139–143, 2007.

[161] Anna-Mária Tőkés, Janina Kulka, Sándor Paku, Ágnes Szik, Csilla Páska, Pál Kaposi Novák, László Szilák, András Kiss, Krisztina Bögi, and Zsuzsa Schaff. Claudin-1,-3 and-4 proteins and mrna expression in benign and malignant breast lesions: a research study. *Breast Cancer Res*, 7(2):296–305, 2005.

[162] Norimasa Sawada, Masaki Murata, Keisuke Kikuchi, Makoto Osanai, Hirotoshi Tobioka, Takashi Kojima, and Hideki Chiba. Tight junctions and human diseases. *Medical Electron Microscopy*, 36(3):147–156, 2003.

[163] Tracey A Martin, Gareth Watkins, Robert E Mansel, and Wen G Jiang. Loss of tight junction plaque molecules in breast cancer tissues is associated with a poor prognosis in patients with breast cancer. *European journal of cancer*, 40(18):2717–2725, 2004.

[164] Patrice J Morin. Claudin proteins in human cancer: promising new targets for diagnosis and therapy. *Cancer research*, 65(21):9603–9606, 2005.

[165] Marco Cantisani, Daniela Guarnieri, Marco Biondi, Valentina Belli, Martina Profeta, Luca Raiola, and Paolo A Netti. Biocompatible nanoparticles sensing the matrix metallo-proteinase 2 for the on-demand release of anticancer drugs in 3d tumor spheroids. *Colloids and Surfaces B: Biointerfaces*, 135:707–716, 2015.

[166] Mathumai Kanapathipillai, Amy Brock, and Donald E Ingber. Nanoparticle targeting of anti-cancer drugs that alter intracellular signaling or influence the tumor microenvironment. *Advanced drug delivery reviews*, 79:107–118, 2014.

[167] Simona Mura, Julien Nicolas, and Patrick Couvreur. Stimuli-responsive nanocarriers for drug delivery. *Nature materials*, 12(11):991–1003, 2013.

[168] Yanhua Liu, Wenping Wang, Jianhong Yang, Chengming Zhou, and Jin Sun. ph-sensitive polymeric micelles triggered drug release for extracellular and intracellular drug targeting delivery. *asian journal of pharmaceutical sciences*, 8(3):159–167, 2013.

[169] Huachao Chen, Danyang Liu, and Zijian Guo. Endogenous stimuli-responsive nanocarriers for drug delivery. *Chemistry Letters*, (0), 2016.

[170] You Han Bae and Kinam Park. Targeted drug delivery to tumors: myths, reality and possibility. *Journal of Controlled Release*, 153(3):198, 2011.

[171] Xinyi Jiang, Hongliang Xin, Jijin Gu, Ximing Xu, Weiyi Xia, Shuo Chen, Yike Xie, Liangcen Chen, Yanzuo Chen, Xianyi Sha, et al. Solid tumor penetration by integrin-mediated pegylated poly (trimethylene carbonate) nanoparticles loaded with paclitaxel. *Biomaterials*, 34(6):1739–1746, 2013.

[172] Sabine H van Rijt, Deniz A Bölükbas, Christian Argyo, Stefan Datz, Michael Lindner, Oliver Eickelberg, Melanie Königshoff, Thomas Bein, and Silke Meiners. Protease-mediated release of chemotherapeutics from mesoporous silica nanoparticles to ex vivo human and mouse lung tumors. *ACS nano*, 9(3):2377–2389, 2015.

[173] Wenxiu Hou, Fangfang Xia, Carla S Alves, Xiaoqing Qian, Yuming Yang, and Daxiang Cui. Mmp2-targeting and redox-responsive pegylated chlorin e6 nanoparticles for cancer near-infrared imaging and photodynamic therapy. *ACS applied materials & interfaces*, 8(2):1447–1457, 2016.

[174] Peter C Black and Colin PN Dinney. Bladder cancer angiogenesis and metastasis—translation from murine model to clinical trial. *Cancer and Metastasis Reviews*, 26(3-4):623–634, 2007.

[175] Susan A Brooks, Hannah J Lomax-Browne, Tracey M Carter, Chloe E Kinch, and Debbie MS Hall. Molecular interactions in cancer cell metastasis. *Acta histochemica*, 112(1):3–25, 2010.

[176] Daniela Guarnieri, Marco Biondi, Hui Yu, Valentina Belli, Andrea P Falanga, Marco Cantisani, Stefania Galdiero, and Paolo A Netti. Tumor-activated prodrug (tap)-conjugated nanoparticles with cleavable domains for safe doxorubicin delivery. *Biotechnology and bioengineering*, 112(3):601–611, 2015.

[177] Rutian Li, Wei Wu, Qin Liu, Puyuan Wu, Li Xie, Zhenshu Zhu, Mi Yang, Xiaoping Qian, Yin Ding, Lixia Yu, et al. Intelligently

targeted drug delivery and enhanced antitumor effect by gelatinase-responsive nanoparticles. *PloS one*, 8(7):e69643, 2013.

[178] Emanuel Fleige, Mohiuddin A Quadir, and Rainer Haag. Stimuli-responsive polymeric nanocarriers for the controlled transport of active compounds: concepts and applications. *Advanced drug delivery reviews*, 64(9):866–884, 2012.

[179] Ahmed M Mansour, Joachim Drevs, Norbert Esser, Farid M Hamada, Osama A Badary, Clemens Unger, Iduna Fichtner, and Felix Kratz. A new approach for the treatment of malignant melanoma: enhanced antitumor efficacy of an albumin-binding doxorubicin prodrug that is cleaved by matrix metalloproteinase 2. *Cancer research*, 63(14):4062–4066, 2003.

[180] Neetu Singh, Amrita Karambelkar, Luo Gu, Kevin Lin, Jordan S Miller, Christopher S Chen, Michael J Sailor, and Sangeeta N Bhatia. Bioresponsive mesoporous silica nanoparticles for triggered drug release. *Journal of the American Chemical Society*, 133(49):19582–19585, 2011.

[181] Andrew S Mikhail, Sina Eetezadi, Sandra N Ekdawi, James Stewart, and Christine Allen. Image-based analysis of the size-and time-dependent penetration of polymeric micelles in multicellular tumor spheroids and tumor xenografts. *International journal of pharmaceutics*, 464(1):168–177, 2014.

Acknowledgments

Firstly, I would like to express my sincere gratitude to my tutor Prof. Paolo Antonio Netti and my advisors Francesco Urciuolo, Giorgia Imparato and Virginia Brancato for the continuous support of my Ph.D study and related research, for his patience, motivation and immense knowledge. Their guidance helped me in all the time of research and writing of this thesis.

I would also like to thank all my friends and colleagues (Brunella, Claudia, Francesca, Bernadette, Ezia, Sara, Angela, Martina, Andrea, Flavia). Their support and care helped me overcome setbacks and stay focused on my Ph.D study. I greatly value their friendship and I deeply appreciate their belief in me.

Most importantly, none of this would have been possible without the love and patience of my family and my boyfriend. My family has been a constant source of love, concern, support and strength all these years. Without their precious support it would not be possible to conduct this research.